Aus der Medizinischen Universitätsklinik Tübingen
Abteilung VIII - Medizinische Onkologie und Pneumologie

Virotherapy of the Hepatocellular Carcinoma Characterization of Resistance to the Recombinant Vaccinia Virus GLV-0b347 in Murine HCC Cell Lines with Distinct Oncogenic Mutations

Inaugural-Dissertation
zur Erlangung des Doktorgrades
der Medizin

der Medizinischen Fakultät
der Eberhard Karls Universität
zu Tübingen

vorgelegt von

Fischer, Daniel Joseph

2022

Dekan: Professor Dr. B. Pichler

1. Berichterstatter: Professor Dr. U. Lauer
2. Berichterstatter: Professor Dr. E. Wieland

Tag der Disputation: 10.06.2021

to my family
and
my teachers

Contents

List of Figures

List of Tables

1 Introduction

1.1 The Hepatocellular Carcinoma

1.1.1 Epidemiology and Etiology

With an estimated 781,631 deaths in the year 2018 liver cancer is the fourth leading cause of cancer death worldwide (8.2% of total cancer deaths). It is the fifth most common malignancy in men (incidence: 596,574 cases, 6.3% of the total) and the ninth most common in women (244,506 cases, 2.8%) [1]. Primary liver cancer (PLC), of which the hepatocellular carcinoma (HCC) is the most common, is mostly a problem of developing countries. High risk regions include South-east Asia and sub-Saharan Africa, with nearly 50% of all cases occurring in China. Alarming is the rising incidence of HCC in the last years. With its dismal prognosis (mortality-to-incidence ratio: 0.95) most patients of primary liver cancer do not survive longer than one year [2]. The most important risk factors for HCC include chronic liver infection with hepatitis B or C as well as toxic injury through aflatoxin B or alcohol. Metabolic syndrome and non-alcoholic fatty liver disease (NAFLD) gain increasing attention as important risk factors [3]. Other co-factors include infection with human immunodeficiency virus (HIV), which increases the risk of HCC [4], and hereditary diseases which potentiate the impact of chronic infections, such as hemochromatosis and Wilson's disease etc. [2]. The demography of HCC is very closely linked to the distribution of its risk factors. A high prevalence of hepatitis B and ingestion of with aflatoxin B contaminated food occasion a high incidence of HCC in developing countries, whereas hepatitis C and alcohol play the main role in developed countries [5]. Vertical transmission of hepatitis B from mother to child in high-risk regions causes an early onset of PLC (starting at 20 years of age), whereas in developed countries infection with hepatis B or

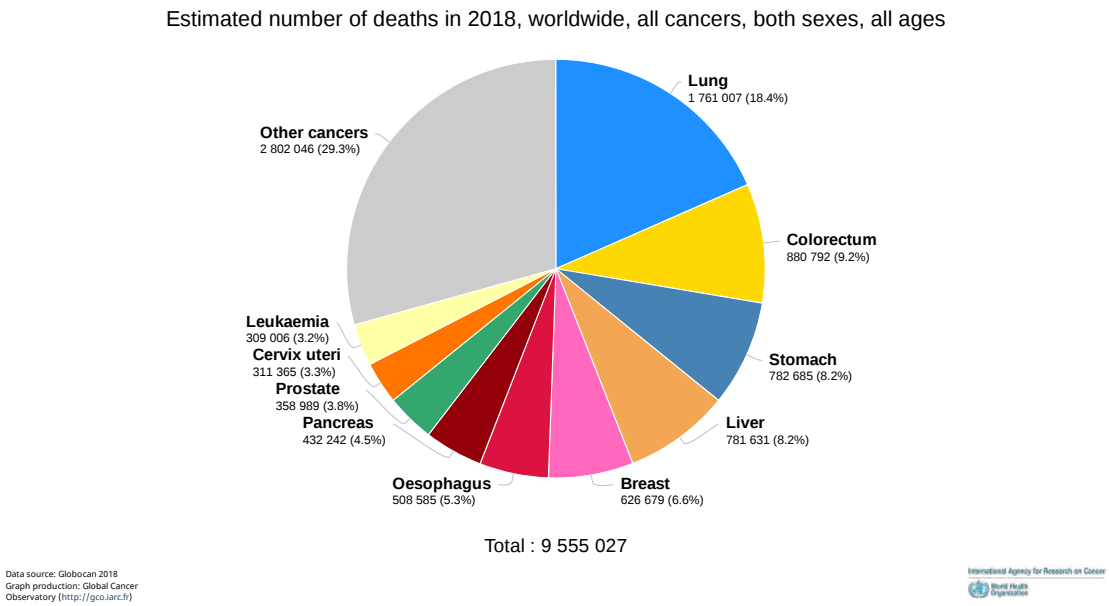

Figure 1: Estimated cancer deaths in 2018 worldwide. The figure shows the estimated worldwide mortality due to specific cancer entities in the year 2018. Figure was generated on 25.04.2019 with CANCER TODAY, a subsection of the Global Cancer Observatory (http://gco.iarc.fr) of the International Agency for Research on Cancer (IARC).

C occurs mostly in adolescence, either through intravenous drug abuse, sexual transmission or unscreened blood transfusions. Together with the effect of alcohol they cause a late onset starting around the age of 50 [2]. The most important preventive measure against HCC will be universal hepatitis B virus vaccinations and antiviral prophylaxis for infective mothers, especially in endemic regions [6]. Epidemiologic studies in China and Taiwan demonstrate the effectiveness of vaccination programs in preventing PLC [7, 8].

1.1.2 Mutational Patterns of HCC

Hepatocarcinogenesis is a heterogeneous multistep process involving various genes and signaling pathways. The molecular profile of HCC varies dependent on exposure to carcinogenic risk factors and geographic location. Mutations may be relevant for subclass treatment options and determine the individual prognosis [9]. It is established that repeated hepatocyte injuries leading to continuous cycles of necrosis and regeneration on a background of chronic inflammation facilitate carcinogenic mutations [10]. Most common mutations include inactivation of tumor suppressor p53 (TP53, 25-40%), activation of Catenin beta-1 (β-catenin,

CTNNB1, 25%), overexpression or activation of ErbB receptor family members and epigenetic deregulation of various cancer related genes [10, 11]. The p53 protein is the key player in surveying and sustaining the genomic integrity of cells by detecting DNA damage and gaining cell cycle control, inducing DNA repair or eventually apoptosis. The β-catenin protein functions as a cell-cell adhesion molecule and as an intracellular signal transducer in the canonical wingless (Wnt) signaling pathway (Wnt/β-catenin pathway), which is involved in cell differentiation, proliferation and homeostasis. It also is known for its role in carcinogenesis. Extracellular Wnt binding its receptor disrupts the degradation of β-catenin in the cytoplasm and allows translocation of β-catenin into the nucleus where it activates Wnt response genes [12]. A similar pathway is the Hedgehog (Hh) signaling pathway which mediates cell differentiation, regeneration, and stem cell renewal. Hh activity leads to accumulation of the transcription factor Gli in the nucleus, activating genes controlling cell cycle and growth. Furthermore, Hh induces the overexpression of c-Myc (MYC), which is itself an important oncogene [13]. C-Myc amplification is associated with a poor prognosis [14, 15]. Many HCCs have mutated tyrosine kinase receptor (TKR)-dependent pathways, e.g. epidermal growth factor receptor (EGFR). Overexpression of EGFR (68%) and RAS/MAPK (50%), as well as abnormal activation of PI3K/AKT signaling, suppressing apoptosis, are common [16]. These provide targets for modern treatment options (see chapter 1.1.3). Other widespread mutations are amplifications of vascular endothelial growth factor A (VEGFA), contributing to the high vascularization of HCC [17], as well as epigenetic silencing (CpG hypermethylation of promoter regions) of tumor suppressors e.g. phosphatase and tensin homolog (PTEN) [18] and various others [11].

1.1.3 State of the Art Therapy

Effective treatment of patients with hepatocellular carcinoma is highly dependent on the preceding assessment of prognosis. The earlier the tumor is detected, the better the prognosis and the chance of cure through resection. Unluckily, most HCCs are detected in a late and symptomatic stage, where options are mostly limited to palliative treatments. The validated Barcelona Clinic Liver Cancer (BCLC) staging and treatment strategy selects patients according to prognosis and gives treatment recommendations [19]. The BCLC considers tumor size and spread,

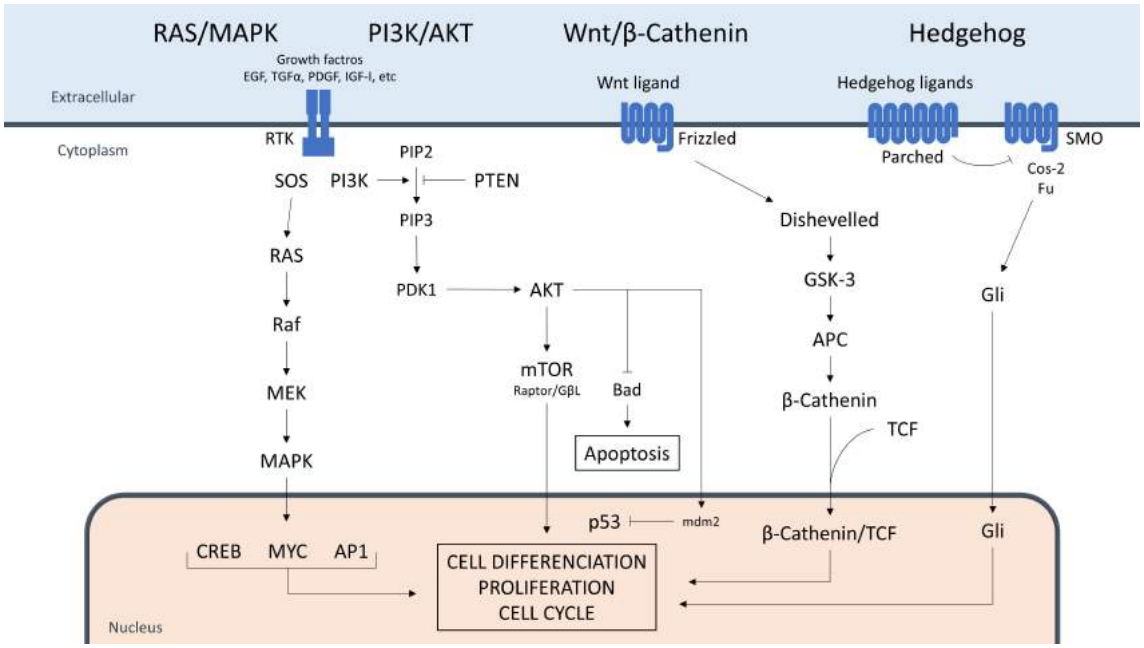

Figure 2: Molecular pathways affected in HCC. Major signaling pathways and genes affected in HCC, including the RAS/MAPKinase, PI3K/Akt, Wnt/β-Catenin and Hedgehog pathways, as well as MYC and p53. These occasion for dysregulated cell differentiation, excessive proliferation and loss of cell cycle control with aggravated apoptosis. Adapted from Villanueva et al, 2007 [11].

liver function (Child-Pugh classification) and the patients' general health and performance status (ECOG classification). The treatment recommendations of the European Society for Medical Oncology (ESMO) are based on the BCLC staging. Early stage (0 and A) patients with asymptomatic single or small localized nodules are thereby referred to radical curative treatments including ablation, resection or liver transplantation. Intermediate (B) patients with large multinodular lesions are treated palliatively with trans-arterial chemoembolization (TACE). Advanced staged (C) with portal invasion or extrahepatic spread receive systemic treatments, with multikinase inhibitors or immunotherapy. End stage (D) patients receive best supportive care, as their prognosis is dismal and further interventions bare no benefit.

Sorafenib (Nexavar®) is an oral multikinase inhibitor and the first of several others that are approved for the treatment of solid tumors such as HCC. It inhibits various tyrosine kinases, such as VEGFR and platelet-derived growth factor receptors (PDGFR), and furthermore Raf (MAPK-signaling). It slows tumor cell proliferation, reduces tumor vascularization and induces apoptosis [20]. In 2019 lenvatinib joined sorafenib as first line treatment for BCLC stage C patients after a phase III clinical trial showed non-inferiority to sorafenib as first line treatment [21]. Lenvatinib acts by inhibiting VEGFR1-3, FGFR1-4, PDGFR, KIT and RET proto-

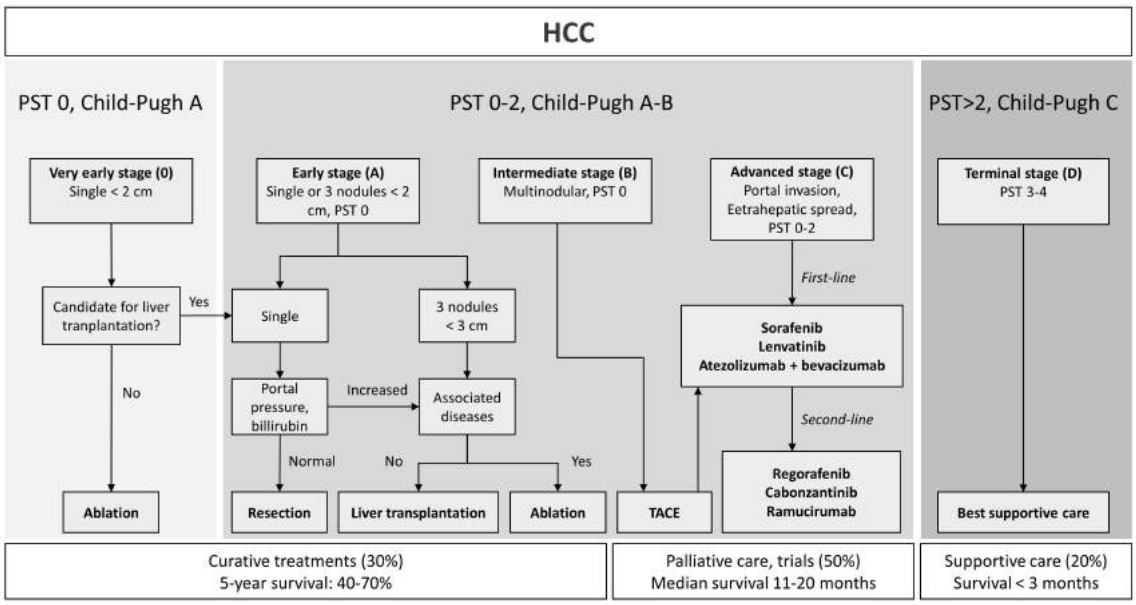

Figure 3: HCC-treatment algorithm. The underlying Barcelona Clinic Liver Cancer (BCLC) staging and treatment strategy is complemented by current ESMO HCC-treatment recommendations. Modified from Harrison's Principles of Internal Medicine 19th edition and ESMO Clinical Practice Guidelines for diagnosis, treatment and follow-up (including the eUpdate from 19th June 2020) [23]. HCC: hepatocellular carcinoma. PST: ECOG performance status. TACE: trans-arterial chemo embolization.

oncogene. In 2020 the US Food and Drug Administration (FDA) gave approval for the combination of atezolizumab (Tecentriq®) plus bevacizumab (Avastin®) as an initial treatment for patients with advanced disease (BCLC stage C). A global, open-label, phase III trial showed that a combination treatment of the PD-L1 antagonizing monoclonal antibody atezolizumab and the anti-VEGF antibody bevacizumab results in a longer overall and progression-free survival compared to treatment with sorafenib [22]. This resembles the first major improvement in HCC treatment since over a decade.

1.2 Oncolytic Virotherapy

Oncolytic virotherapy (herein abbreviated OVT) is an innovative emerging new field of selective cancer therapy. Its core principle relies on replication-competent oncolytic viruses (OVs) which selectively infect tumor cells, multiply and destroy tumor tissues. The concomitant release of tumor-neoantigens in an immunostimulatory environment activates a long-lasting host adaptive immune response

against the tumor, resulting in clearance of metastatic sites. Treatment options can be increased by arming oncolytic viruses with transgenes (e.g. "suicide genes"), enhancing their lytic efficiency or enabling complementary gene therapy [24, 25]. Oncolytic viruses that have been approved for treatment include Oncorine (H101) in China and Talimogene laherparepvec (Imlygic®, T-Vec), developed by Amgen, in the US and in Europe [26, 27]. Wide panels of promising OVs, therapy schemes and combination therapies are under investigation in clinical trials while preclinical research focuses on improving key aspects like specificity and potency of oncolytic viruses [28]. In few cases OVT showed its full potential inducing long lasting tumor remission in patients with end-stage disseminated cancers [29].

1.2.1 Brief History of Oncolytic Virotherapy

The beginning of oncolytic virotherapy roots in the mid-1800s were several case reports describe tumor regression after coincidental virus infection. Especially conspicuous were reports of hematological malignancies going in remission after natural infection with measles virus [30], including one famous case report describing regression of a Burkitt's lymphoma in a young boy [31]. First mentionable clinical trials started in the 1950s utilizing wild-type human pathogenic viruses in the form of infective body fluids, showing proof of concept. Unsurprisingly those trials showed insufficient efficacy and poor safety, often causing more harm than benefit for the patients. A lack of understanding viruses and cancer biology slowed down the development of better OVs. It was not until the late 1990s, that the wide availability of recombinant DNA technology enabled modifications of the viral genome on large scales [32]. The new possibilities in biotechnology caused a renaissance in oncolytic virotherapy. The last two decades brought significant progress in the development of OVs, achieving major milestones concerning safety, specificity, potency and delivery [25], as further discussed below. These developments culminated in 2015 as talimogene laherparepvec, a recombinant herpes simplex virus type-1 named T-Vec, was approved by the FDA as the first oncolytic virus in the west.

1.2.2 Principles of Oncolytic Virotherapy

The full range and mechanisms of the anti-tumor activity of OVs remain incompletely understood, but two distinct mechanisms of action (MOA) are thought to cause the main therapeutic effects. First, a direct tumor mass reducing action through OVs that replicate selectively in cancer cells causing oncolysis, thereby releasing viral progeny. This makes OVs self-enhancing drugs at precisely the site where they are needed. The reduction of tumor cells by second generation OVs is dubbed *bystander effect*. The second and most important MOA is the induction of an adaptive immune response against the tumor. The triggered immune response can further attack residual cancer cell nests at distant tumor sites inside the patient's body. The transformation of the initial localized (lytic) antitumor effect into a systemic immune response, clearing metastasis, is described by the so-called *paradigm of oncolytic virotherapy* [33]. This effect was shown i.a. through a phase III clinical trial, that ultimately led to the approval of the recombinant herpes simplex virus type-1 (T-Vec) in the USA [34]. Due to these immune modulating properties OVs may also be called oncolytic immunotherapeutics.

Selectivity

Concerning biosafety, the most crucial property of OVs is their ability to enter and replicate predominantly in neoplastic cells. There are various mechanisms that ensure that OVs do not enter or propagate in healthy cells. Those mechanisms can be grouped into pre-entry and post-entry selectivity. As described by the so-called "hallmarks of cancer" (Hanahan and Weinberg, 2011), neoplastic cells often lose antiviral defense mechanisms during oncogenic transformation [35], e.g. to shut down protein biosynthesis, up-regulate major histocompatibility complex (MHC) presentation or activate apoptosis. Oncolytic viruses benefit from these cancer cell immune evasion pathways, described by Pikor et al. in 2015 as "Exploiting Cancer's Deal with the Devil" [36]. The most important and frequently affected pathway involves the interferon (IFN) response signaling. This can affect both IFN production and/or adequate response to IFNs [33]. Further ways of ensuring post entry-selectivity is to genetically modify OVs by deleting genes (e.g. virulence factors) that are crucial for survival in normal cells but are not obligatory for efficient replication in cancer cells [37]; restricting entry by engineering tumor

specific ligands into the viral particles surface [38]; by inserting promoters specific to the tumor-environment thereby gaining transcriptional control of essential viral genes and other [39, 40].

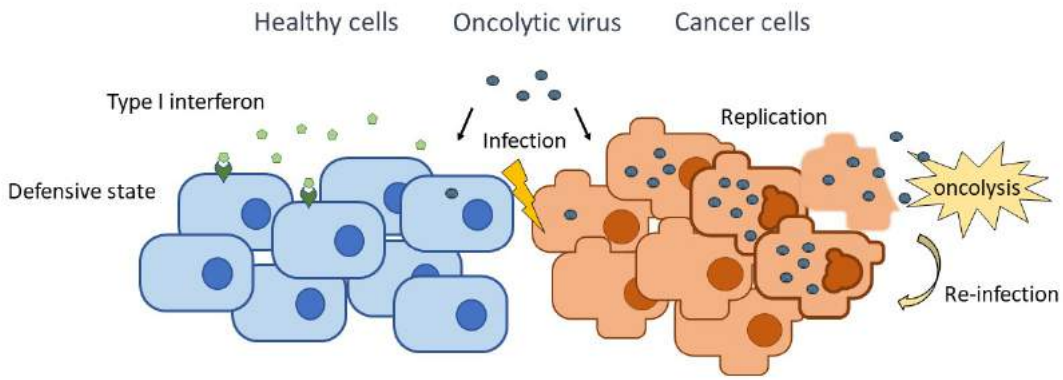

Figure 4: Selectivity of oncolytic viruses. OVs may infect both malignant and healthy cells but are only capable to sustain effective replication in interferon deficient malignant cells. Healthy cells secrete type 1 interferons (e.g. interferon beta) and turn into a defensive state controlling the infection. In contrast malignant cells are highjacked by the OV and produce viral progeny until the cells burst and are disintegrated (oncolysis).

Anti-Tumor Immunity

The most important effect of oncolytic virotherapy is triggered by OV-induced immunogenic cancer cell death (ICD; includes apoptosis, autophagic cell death, pyroptosis, necrosis and necroptosis) leading to concomitant release of tumor neo-antigens and danger associated molecules that are recognized by antigen presenting cells (APCs), eventually culminating in a host adaptive immune response [41]. This complex process involves viral and tumor (neo-) antigens being exposed simultaneously to various immune cells in an inflammatory environment. Infection of the tumor cell causes genotoxic stress, the upregulation of reactive oxygen species (ROS) and production of antiviral cytokines, e.g. type-1 Interferons (IFNs). When released, they stimulate APCs, CD8+ cytotoxic T cells and natural killer (NK) cells. Following oncolysis, endogenous danger associated molecular patterns (DAMPs) and pathogen associated molecular patterns (PAMPs) are

released, further activating immune cells through binding to their pattern recognition receptors (PRRs; chapter 1.4.1), most importantly Toll-like receptors. Tumor associated antigens (TAAs) including neo-antigens are processed by APCs which then activate CD4+ helper T cells and CD8+ cytotoxic T cells, resulting in an host immune response against OV-infected and non-infected tumor cells. The therapeutic effect of immune mediated anti-tumor activity seems to depend especially on CD8+ T cells and NK cells [42]. Certain genetically modified viruses including T-Vec carry cytokine coding transgenes, e.g. granulocyte-macrophage colony-stimulating factor (GM-CSF), or other adjuvants to boost their immune stimulating properties.

1.2.3 Modifying Oncolytic Viruses

Modern biotechnology allows modification of viral agents in multiple ways. The PEGylation or polymeric coating of viral particles can shield them from preformed neutralizing antibodies [43, 44] while the engineering of the viral capsid and its receptors can create a cell type-specific tropism [38]. The most common methods involve the genetic modification of the viral genome, e.g. deletion of virulence genes, modification of structural proteins and insertion of therapeutic transgenes, as already mentioned in the chapters above. Modifications are utilized i.a. to enhance lytic effectivity, improve safety [45], modify host immune response [46] or to label tumor cells for imaging [47]. A very elegant example of genetic modification is the insertion of so-called suicide genes [48]. These convert non-toxic prodrugs into their active and lethal form. The activation is confined to the site of the suicide gene expression, enabling a localized effect of the compound even if administered systemically. One example is the measles virus MeV-SCD expressing a super cytosine deaminase (SCD) suicide gene encoding a fusion protein of cytosine deaminase and uracil phosphoribosyltransferase. The enzyme converts the nontoxic prodrug 5-fluorocytosine (5-FC) into the chemotherapeutic compound 5-fluorouracil (5-FU) [49, 50]. These genetic modifications multiply the range of possibilities and implications for oncolytic virotherapy.

1.2.4 Perspectives

The significance of OVs in cancer therapy is rising, especially as part of a combined therapy approach. As stated by Kaufman et al.: *"Oncolytic viruses can easily be combined with a wide range of therapies, including surgical resection, chemotherapy, radiation therapy, hormonal therapy, targeted therapies, and immunotherapy"* [33]. And many possible combinations are under current clinical investigation. For example, due to its immune response eliciting properties, OVT proved to be synergistic with immune checkpoint inhibition (ICI) therapy. In some cases, the combination can overcome systemic ICI resistance by increasing neoantigen directed T-cell responses [42, 51].

Clinical Testing

As indicated by Russell, Peng and Bell in 2012, one of the greatest challenges for OVT at the current moment is clinical testing. When considering the long list of potential wild type viruses applicable for OVT, all possible beneficial modifications and all possible indications, protocols etc., clinical research encounters a problem: Every combination classifies as a new and different product, which will make it nearly impossible to generate sufficient clinical data for many of these OVT-options. Furthermore, advances in OV-technologies develop faster than current state of the art OVT can be clinically tested. Russell et al. summarized the situation as follows: *"The solution to this conundrum of technology developments outstripping our ability to test them in the clinic will most likely have to be a new drug development paradigm for the oncolytic virotherapy field in which iterative phase 1 equivalence clinical trials become standard practice."* [25]. New strategies in clinical testing will be crucial to get innovative OVT from bench to bedside.

1.3 Vaccinia Virus in Oncolytic Virotherapy

Vaccinia virus (VACV) is a member of the *Poxviridae* family, genus *Orthopoxvirus*. It is historically known for its major role as the vaccine that helped eradicate the highly lethal smallpox disease (caused by the variola virus) in 1977. As depicted by Shen and Nemunaitis in 2005, VACV has made a comeback in recent years as a platform for modern cancer immunotherapy. Genetically engineered VACVs are currently explored as vectors for anti-cancer gene therapy, as anti-cancer vaccines and as replication-competent oncolytic viruses [52]. There are many important features that make vaccinia virus a favorable choice. It has a well-known safety profile as demonstrated in its extensive use as an effective vaccine. The strict limitation of its replication cycle to the cytoplasm makes any interference with the human genome extremely unlikely [53]. Also, the large viral DNA genome allows the insertion of large transgenes thereby increasing the therapeutic possibilities. Other favorable properties include a natural tumor tropism [54], high immunogenicity [55], strong lytic efficacy and a short life cycle.

1.3.1 Wildtype Vaccinia Virus

All members of the Poxviridae family are complex, linear, double stranded DNA-viruses. They replicate exclusively in the cytoplasm of their host cells, as displayed in figure 5 [53]. The vaccinia virus appears in different structural forms. The basic infectious form, the mature virion (MV), has a barrel like shape, measures approximately 360 x 270 x 250 nm and has a mass of 9.5 fg. Its genome consists of almost 195 kbp and comprises approximately 250 open reading frames (ORFs). All VACV genes are categorized into early, intermediate and late genes, according to their time of expression. Next to the MV, the enveloped virion (EV) has an additional envelope and is concerned with cell-to-cell spread. MVs can enter the cell either by fusion with the cell membrane or by endocytosis. The exact mechanisms of cell invasion are still unclear.

Human infection with wild type Vaccinia, as by vaccination, causes a typical vesiculopustular response which remains as a smallpox vaccine scar. Compared with modern vaccines, vaccinia virus poses a higher risk of adverse reactions, especially for people with compromised cellular immunity. Rare but severe compli-

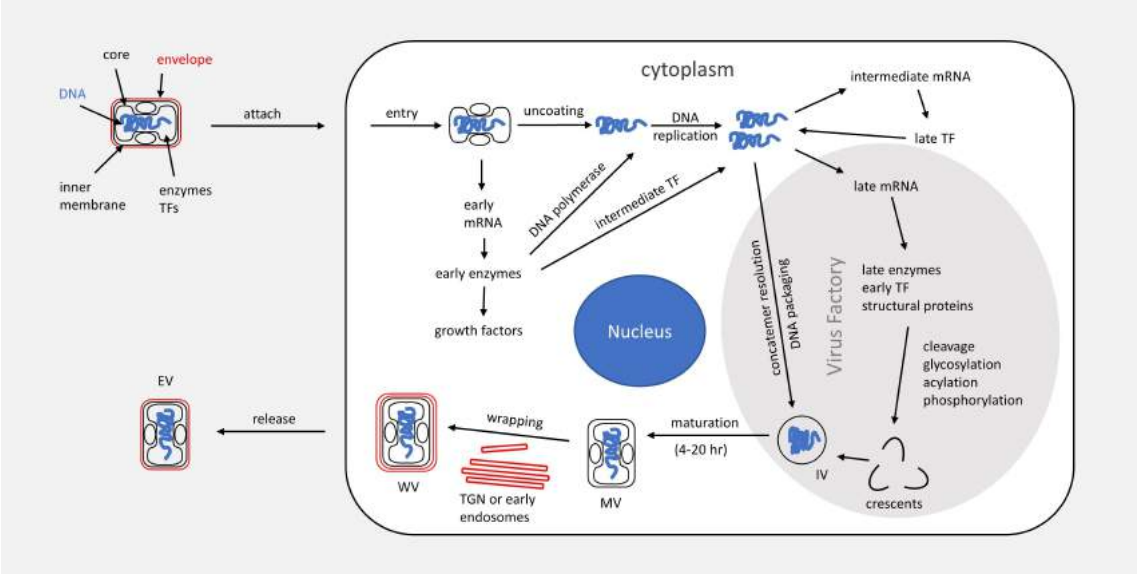

Figure 5: Replication cycle of vaccinia virus. Succeeding cell entry, the viral particle is uncoated, and a cascade of transcription factors, mRNA and enzymes are released leading to the production of new viral particles. Following the attachment and entry, the DNA is uncoated releasing core proteins. Early mRNAs are synthesized, which translate into early enzymes: DNA and RNA-polymerases and intermediate transcription factors (TF). DNA is replicated into large concatemers and intermediate mRNA is translated into late TFs which subsequently initiates the transcription of late genes. These late mRNAs are translated into late enzymes, early TF and structural proteins. They are further modified and assembled with packed DNA into immature virions (IV). After 4-20 hours IVs have matured (MV) and are wrapped into modified membranes of the trans-Golgi network (TGN) or the early endosome. The wrapped virion (WV) fuses with the outer cell membrane to release an extracellular enveloped virion (EV). This figure is adapted from Fields virology 6th edition, 2013 [57].

cations include generalized vaccinia, eczema vaccinatum, progressive vaccinia, and postvaccinial encephalitis [56].

Clinical Trials with Wild Type Vaccinia

As summarized by Shen et al. clinical trials employing wild type VACV include: Roenigk et al. (1974), a study on 20 patients with metastasized malignant melanoma, injecting the Wyeth strain (world's first smallpox vaccine) directly into the tumor [58], Hansen et al. (1978), describing a case of untreated chronic lymphocytic leukemia going into remission after a smallpox vaccination [59] and Mastrangelo et al. (2002), a study comprising five patients with recurrent melanoma, using intratumoral injections of the Wyeth strain [60].

1.3.2 GL-ONC1

The recombinant vaccinia virus GLV-1h68 (GL-ONC1) is an OV developed by Genelux Corporation [61]. The vaccinia Lister strain was modified by inserting three expression cassettes coding for Renilla luciferase-Aequorea GFP (Ruc-GFP) fusion protein, β-galactosidase, and β-glucuronidase into the viral genome (figure 6). Thereby the F14.5L, J2R (encoding thymidine kinase) and A56R (encoding hemagglutinin) ORFs were disrupted, leading to a further attenuation of the virus.

GLV-1h68 has been extensively studied in preclinical settings [47] and is currently under clinical investigation in multiple clinical trials (table 7). One completed phase I/II study administrating GLV-1h68 intraperitoneally to patients with advanced peritoneal carcinomatosis reports that in 8 out of 9 patients GL-ONC1 effectively infected and replicated within the patients tumor and led to oncolysis [62]. Two further ongoing studies involve topical application of GL-ONC1, a phase I/II study with intraperitoneal administration of GLV-1h68 in patients with recurrent or refractory ovarian cancer and a study with intrapleural administration in patients with malignant pleural effusion. Systemic administration of GL-ONC1 is under investigation in two completed and one ongoing phase I trial administrating the virus intravenously prior to surgery.

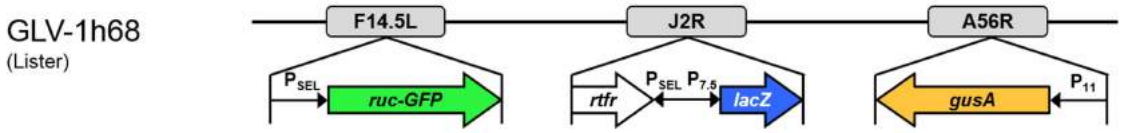

Figure 6: GLV-1h68 genetic modifications. A56R: Haemagglutinin. F14.5L: IMV protein. gusA: β-glucuronidase. J2R: Thymidine kinase. lacZ: β-galactosidase. P 7.5 : Promoter of the vaccinia virus 7.5-kDa polypeptide (early promoter). P 11: Late promoter. P SEL: Synthetic early late promoter. rtfr: Reverse inserted human transferrin receptor. ruc-GFP: Renilla luciferase-Aequorea GFP. Figure from Chen et al. oral abstract at SITC 27th Annual Meeting 2012.

1.3.3 Pexastimogene devacirepvec (Pexa-Vec)

Pexastimogene devacirepvec or Pexa-Vec is a vaccinia-based virotherapeutic drug containing the recombinant replication-capable virus JX-594. It was cre-

ated by modification of the Wyeth vaccine strain (Dryvax), deleting the thymidine kinase gene, inserting the gene encoding human GM-CSF under control of a synthetic early late promoter and inserting the gene coding for β-galactosidase (lac-Z) [63]. The expression of GM-CSF is supposed to enhance tumor-directed immune response. Pexa-Vec has been extensively tested in multiple preclinical [64] and clinical trials (table 8). It has been shown that JX-594's mechanisms of action involve not only oncolysis and activation of anti-tumor immune responses but also disruption of tumor vasculature [65, 66]. Clinical studies including over 300 adults (by 2015) have proven Pexa-Vec to be safe, employing intravenous and intratumoral administration routes. Safety was also demonstrated in a small cohort of pediatric patients [67]. Up to now there are ten completed clinical studies with Pexa-Vec involving patients with advanced tumors, half of which concern HCC, furthermore colorectal tumors, malignant melanoma and other solid tumors. One randomized phase II dose-finding trial in 30 patients with HCC compared high dose (1 x 10^9 PFU) and low dose (1 x 10^8 PFU) intratumoral injection of JX-594. The survival rate was significantly higher in patients receiving high doses with a median survival of 14.1 months compared to 6.7 months with low dose. Breitbach et al. (2015) report that a phase IIb clinical trial comparing Pexa-Vec and best supportive care (BSC) with BSC alone in patients with advanced liver cancer who failed sorafenib (TRAVERSE-study) could not show improvement of overall survival [68]. Other studies investigate applicability of combination therapies. One phase II study applying a sequential treatment of JX-594 followed by sorafenib showed promising results [69]. Currently a phase I/II trial is combining Pexa-Vec with PD1-blocking antibody nivolumab. A phase III trial comparing Pexa-Vec plus sorafenib with sorafenib monotherapy (PHOCUS) was terminated in 2019 after a pre-planed futility-evaluation by the Independent Data Monitoring Committee (IDMC) recommended its discontinuation.

1.4 Antiviral Response Mechanisms

Through their evolutionary struggle eukaryotic cells developed so called innate immune defense systems (most important the interferon pathway) to survive the constant threat from viral pathogens [70]. Later, higher life forms e.g. mammals developed the adaptive immune system. In vertebrates a major part of the immune defense against viruses is fought on the level of lymphocytes and NK

cells. This section will focus rather on the intrinsic mechanisms of single cells and small local cell groups to prevent viral infection, replication and spread. Various detection molecules sense possible intruders and activate signaling cascades inducing the transcription of multiple genes and the secretion of cytokines, alerting nearby cells. This ultimately results in a defensive state or in apoptosis, either way containing the infection [71]. As viruses and their host organisms co-evolved, viruses have adapted to escape or interrupt these response mechanisms in various ways.

1.4.1 Pattern Recognition Receptors and Downstream Signaling

The first part in the anti-microbial immune defense system comprises different pattern recognition receptors (PRRs) that can sense infections in form of PAMPs and DAMPs (chapter 1.2.2). These PRRs comprise RIG-I-like receptors (RLRs), Toll-like receptors (TLRs), NOD-like receptors (NLRs) and C-type lectin receptors (CLRs) [71]. Concerning viral recognition there are specialized endo-somal and cytosolic sensing molecules that detect atypical nucleic acids (e.g. CpG-DNA or dsRNA) and viral proteins. These sensing molecules fall into four groups: (i) RLRs (intracellular RNA sensors), (ii) Toll-like receptors (extracellular/endosomal), (iii) protein kinase R (intracellular RNA and stress sensor) and (iv) intracellular DNA sensors.

Rig-like Receptors

The most important viral RNA sensing molecules belong to the RIG-like receptor (RLR) family which consists of retinoic acid-inducible gene I (RIG-I, DDX58) [72], melanoma differentiation-associated protein 5 (MDA5, IFIH1) [73, 74] and probable ATP-dependent RNA helicase (LGP2, DHX58) [75]. RIG-I and MDA5 are similar in their properties. Both sense RNA and initiate downstream signaling via the mitochondrial antiviral signaling protein (MAVS/IPS1)-pathway. This phosphorylates interferon regulatory factor (IRF) 3 and IRF7, which dimerize and translocate into the nucleus, activating the transcription of type I IFNs, most notably IFN-β (figure 7).

Cytoplasmatic DNA Sensors

Foreign cytoplasmatic DNA is detected by multiple sensing molecules and activates innate immunity via the stimulator of interferon genes (STING)-pathway, summarized in figure 7 [76]. Intracellular DNA sensors include ZBP1 [77], DDX41 [78], IFI16 [79] and cGAS [80]. Another intracellular dsDNA sensor, which is related to IFI16, is the absent in melanoma 2 (AIM2) protein. Together with ligand-DNA AIM2 binds ASC (apoptosis-associated speck-like protein containing a caspase activation and recruitment domain) forming an inflammasome. Through ASCs caspase activation domain (CARD) the inflammasome recruits and activates caspase-1, which further proteolytically activates inflammatory cytokines IL1-β and IL18. Caspase-1 can lead to pyroptosis through cleavage of gasdermin D [81].

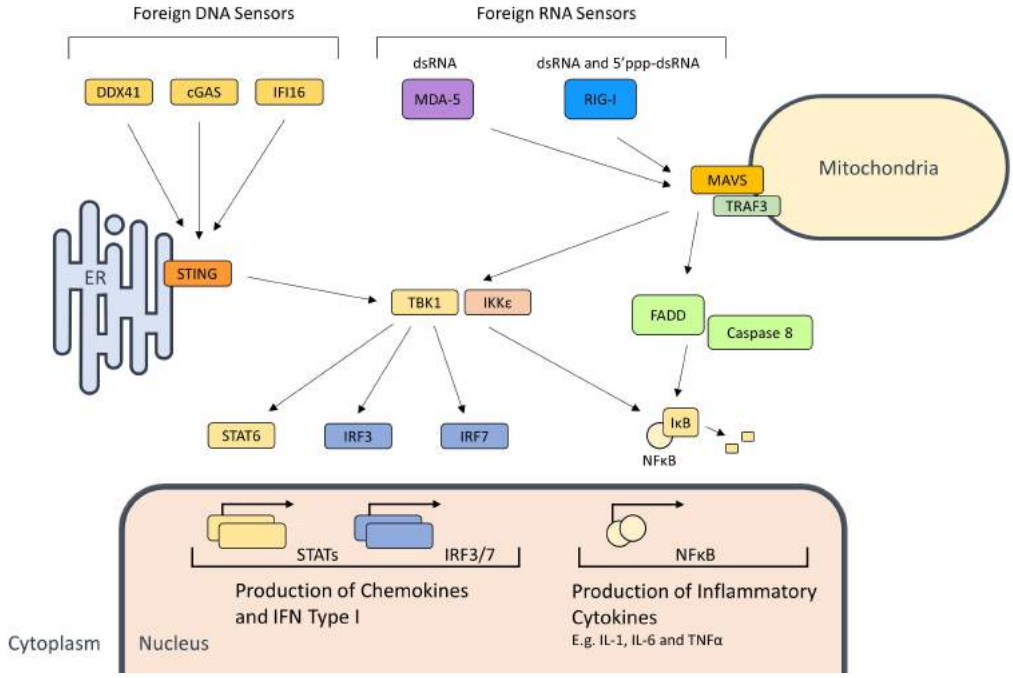

Figure 7: Foreign nucleic acid receptors and signaling pathways. Multiple sensors in the cytoplasm detect foreign nucleotides. Among others, DNA is detected by cyclic GMP-AMP synthase (cGAS), which then activates stimulator of interferon genes (STING) via the production of cyclic GMP-AMP (cGAMP). STING recruits TBK1 and IKKϵ (IKK-i) to activate IRFs, STAT6 and NFκB [76]. Viral RNA is detected by melanoma differentiation antigen 5 (MDA-5) and retinoic acid inducible gene I (RIG-I). Both signal via mitochondrial antiviral-signaling protein (MAVS/IPS-1) and activate TBK1 and IKKϵ via TRAF3. This results in the phosphorylation of IRF3 and 7, which translocate into the nucleus as dimers, inducing the transcription of IFN-β. NFκB is also activated downstream of MAVS via the FADD and Caspase-8 dependent pathway [82].

Toll-like Receptors

Toll-like receptors belong to the most crucial components of the innate immune system. Defects in the TLR-system can lead to serious and very specific immunodeficiency syndromes [83]. So far 10 TLRs have been identified in humans and 12 in mice. Each subtype can be stimulated by a small group of distinct molecules. TLRs are single-pass transmembrane proteins with an extracellular ligand binding site and a single intracellular Toll/Interleukin-1 receptor (TIR) homology domain, which interacts with downstream signaling molecules. There are only three receptors relevant to viral detection: TLR3, able to sense double stranded RNA, TLR7, able to sense single-stranded RNA, and TLR9, which can detect atypical DNA such as unmethylated DNA and CpG-oligodeoxynucleotides (CpG-DNA). Once TLRs are stimulated downstream signaling results in expression of type I interferons and proinflammatory cytokines (figure 8) [84].

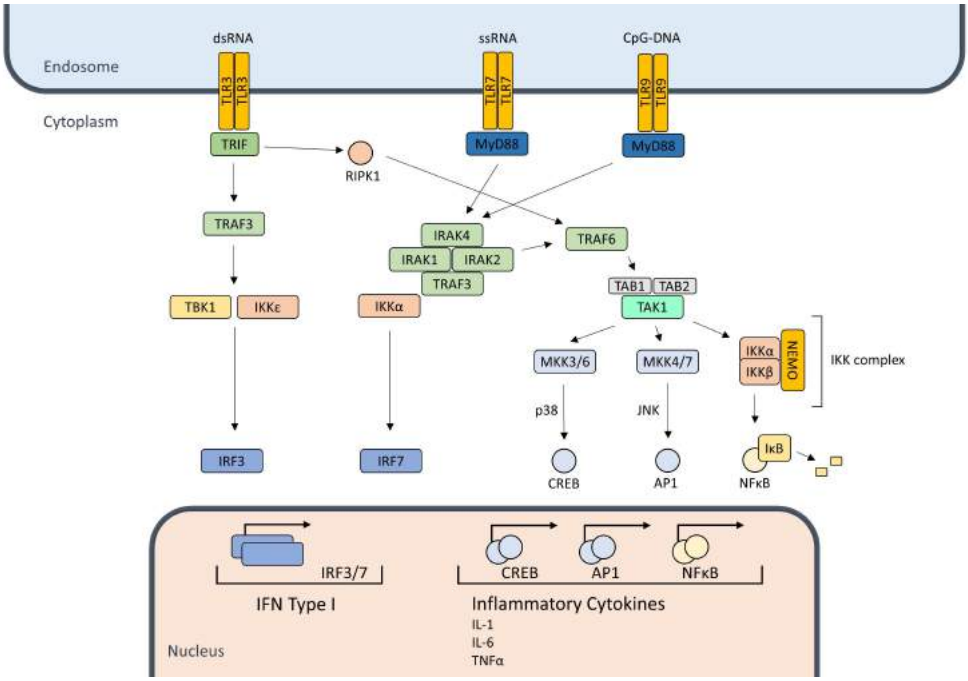

Figure 8: Toll-like receptor signaling pathways. Activated TLRs interact with four different adapter proteins of which the most important is myeloid differentiation primary response protein 88 (MYD88). MyD88 binds activated TLRs and recruit's interleukin-1 receptor associated kinase (IRAK) 4 which phosphorylates IRAK1 and 2, further activating TRAF6. TRAF6 activates NFκB, via TAK1 and activation of the IKK complex. TAK1 further activates MAPK-pathways through activation of MKK3/6 and MKK4/7, resulting in activation of CREB transcription factor and AP1. NFκB, CREB and AP1 ultimately drive the transcription of proinflammatory cytokines, mostly TNFα, IL1 and IL6. The MyD88 dependent pathway can also activate IRF7 and thereby induce type I IFNs. TLR3 is associated with TRIF and can induce type I IFNs through TBK1 and IRF3. TRIF can also cross signal to TRAF6 via RIPK1 [84].

1.4.2 Interferons and Antiviral State

Interferons (IFNs) are cytokines released by host cells in response to viral infections. They play the key role in the immune system's antiviral defense. IFNs alert nearby cells and activate immune cells (NK cells and macrophages). Host cells respond to IFNs by transcribing hundreds of genes, collectively referred to as interferon stimulated genes (ISGs), driving the cells into a defensive state. Broadly described, the pathway starts with PRRs sensing a hazard. These activate IRFs which induce the secretion of (mostly type I) IFNs. Consecutively, IFNs activate the JAK-STAT-pathway inducing an antiviral transcriptome, comprising antiviral effector proteins and feedback loops [85].

Interferons and Signaling

There are three types of IFNs distinguished by their receptors. Type I IFNs (IFN-$\alpha/\beta/\epsilon/\kappa/\omega$) bind to the IFN-$\alpha/\beta$ receptor (IFNAR) consisting of subunits IFNAR1 and 2 [86]. Type II IFN (IFN-γ) binds to the IFN-γ receptor (IFNGR), also consisting of two subunits [87], and type III IFNs (IFN-δ) bind to yet another receptor [88].

The effects of interferon are mediated via the JAK-STAT signaling pathway. Binding of the ligand causes dimerization of receptor subunits. The proximity of associated Janus kinases (JAK1-3 and TYK2) allows cross phosphorylation of JAKs and of the receptor, creating a docking site for the signal transducer and activator of transcription (STAT) proteins. STATs bind and are activated through phosphorylation, after which they dissociate from the receptor and form homodimers and heterodimers. STAT-dimers translocate into the nucleus where they bind specific DNA sequences and initiate transcription. The type I IFN stimulated IFNAR requires JAK1 and TYK2 to phosphorylate STAT1 and STAT2. These form heterodimers and associate with interferon regulatory factor 9 (IRF9 or ISGF3 p48 subunit) forming the ISGF3 transcription factor complex. ISGF3 translocates into the nucleus where it binds IFN stimulated response elements (ISRE) activating transcription of ISGs. The IFNGR passes IFN-γ signal via JAK1 and JAK2 and the activation of STAT1 homodimers which translocate into the nucleus and bind to the gamma activated sequences (GAS) of IFN-γ-stimulated genes [89, 90].

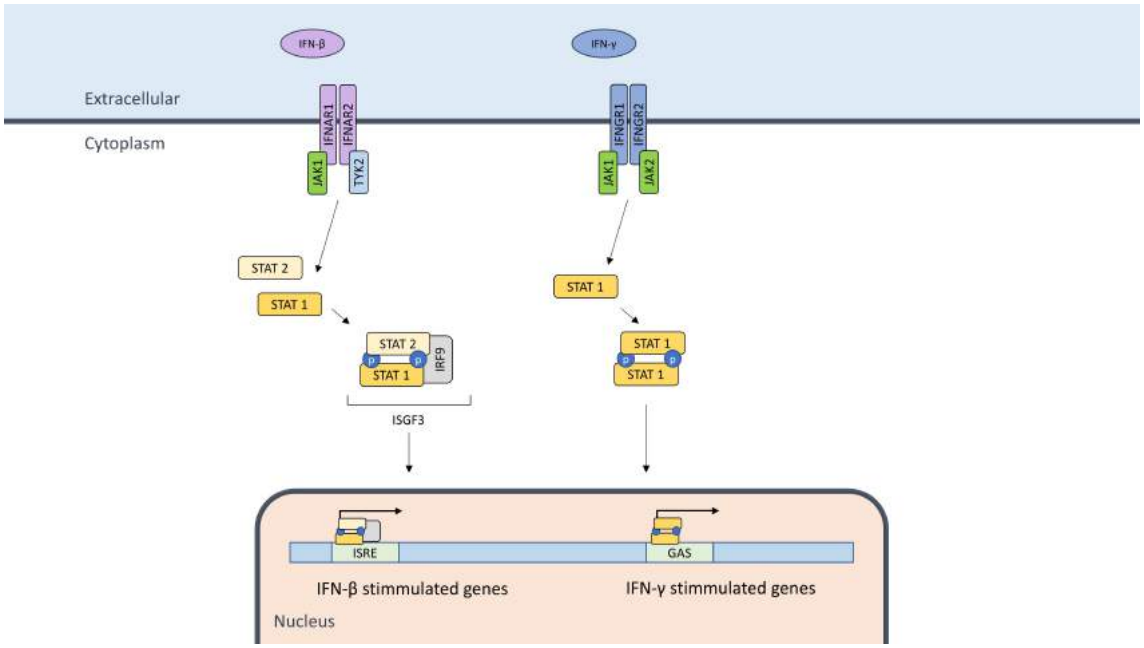

Figure 9: The JAK-STAT-pathway. Cellular effects of IFN-β and IFN-γ are mediated through the JAK-STAT pathway, resulting in the expression of ISGs. IFN-β binds to the IFN-α/β receptor (IFNAR) causing cross phosphorylation of JAK1 and TYK2, which further phosphorylate STAT1 and 2. These form heterodimers and associate with IRF9 (p48) to form IFN-stimulated gene factor 3 (ISGF3) transcription complex. IFN-γ binds to the IFN-γ-receptor (IFNGR) causing cross phosphorylation of JAK1 and JAK2, which further causes dimerization of phosphorylated STAT1. ISGF3 and STAT1-homodimers translocate into the nucleus to bind to IRSE and GAS, respectively, activating transcription of multiple ISGs. Adapted from Samuel, 2001 [90].

Interferon Stimulated Genes and Antiviral State

IFNs induce the transcription of hundreds of different ISGs, which consolidate the cell in an antiviral state. These genes comprise (i) antiviral effectors which can interfere with the viral life cycle, (ii) proteins involved in the IFN-pathway and signaling molecules, and (iii) negative regulators reducing upstream signaling. ISGs can also be directly induced by IRFs bypassing the IFN-pathway. Some of the most efficient antiviral effectors are PKR, the 2-5A system and the Mx system, but many others exist [85, 91]. A further IFN-induced immune response is the upregulation of major histocompatibility complexes for increased viral antigen presentation. This allows better cytotoxic T-cell mediated recognition and killing of infected cells [90].

The interferon-induced, double-stranded RNA-activated protein kinase (PKR) can block translation of AUG codon-dependent mRNA [92] and activate NFκB [93]. As a last option, PKR can induce cell apoptosis [94]. The 2-5A system relies on

2'-5'-oligoadenylate synthetases (OAS) 1 to 3, which are activated by dsRNA and produce 2',5'-oligoadenylates (2-5A). These reversibly activate the 2-5A-dependent RNAse L, which leads to large scale cleavage of ssRNA [95]. The interferon-induced GTP-binding protein Mx1 has a broad and powerful antiviral activity through different mechanisms interfering with transcription, the nucleocapsid transport and other steps in viral replication [96, 97]. Together these systems and many other genes involved establish a highly effective defense mechanism against viral threats.

1.5 Objective

Since the treatment options of hepatocellular carcinoma (HCC), especially in progressed stages of the disease, remain limited in number and effectiveness new and better therapies are needed to reduce HCC related mortality. Oncolytic virotherapy offers a new and promising treatment platform that is especially suitable for patients with disseminated disease. Unfortunately, the efficacy of OV-therapy in individual patients can vary highly. Therefore, it is necessary to explore possible tumor-related properties that account for the varying success of OV-therapy. In a malignancy with such heterogenic mutational patterns as in HCC it might prove useful to correlate certain mutations with increased susceptibility or resistance to a specific OV. The same holds true with the detectable expression of antiviral genes in individual tumors. This information could help to develop OV-panels to match the perfect OV to each individual tumor type.

The goal of this thesis was to investigate the oncolytic effects of a recombinant vaccinia virus (GLV-0b347) on murine hepatocellular carcinoma (mHCC) cell lines. Special attention was paid to the role of the specific tumor mutations and expressed antiviral response genes, which may play a role in tumor resistance to oncolytic virotherapy. The impact of oncogenic mutations and of the innate immune defense in mHCC cells on their susceptibility to oncolytic virotherapy was explored.

2 Materials and Methods

2.1 Laboratory and Working Safety

All experiments were conducted inside the facilities of the Hertie-Institute located at Otfried-Müller-Str. 27 and the Department of Nuclear Medicine located at Otfried-Müller-Str. 14, 72076 Tübingen, Germany. The laboratories comply with the requirements and standards for laboratories with containment level 2 specified in the directive 2000/54/EC of the European Parliament and of the Council of September 18th, 2000, and in the German IfSG of July 20th, 2000. All work involving potentially infectious or hazardous biological or chemical substances was performed under a HERAsafe® laminar flow safety workbench. Every member of the staff wore personal protective equipment. While working with virus containing materials protective glasses and sleeves were worn. Surfaces and materials were disinfected before and after usage with 70% isopropanol, or with Descosept AF and additionally UV-irradiated if procedures involved viruses. Liquid and solid waste was autoclaved at 2 bar pressure and 121 °C for 20 minutes. Waste including TCA, crystal violet, formaldehyde, phenol, β-mercaptoethanol etc. was disposed as special waste.

2.2 Cell Biology Methods

2.2.1 Cell Lines

The murine HCC-cell lines (mHCC) used in this thesis were provided by the research group of Professor Lars Zender, MD. These cell lines are not freely avail-

able as standard cell lines but were created individually within the framework of the groups paper "A MYC-aurora kinase A protein complex represents an actionable drug target in p53-altered liver cancer" in 2016 [98]. They were generated through a well-established transposon-based mouse model. Trans-poson vectors (pCaN, pCaM) carrying oncogenic driver mutations (NrasG12V, MycT58A) were delivered via hydrodynamic tail-vein injection (HDI) into C57BL/6-mice with specific gene double-knockouts (dko; indicated by -/-) for tumor suppressors Cdkn2a ARF or Trp53. Cell lines were derived from the HCCs the mice developed subsequently. The mHCC cell lines carry distinct patterns of oncogenic mutations which represent common alterations in human HCC (chapter 1.1.2). Mutations include Nras, Akt, Myc, TP53 -/- and p19 ARF (alternative reading frame) -/-. CV-1-cells were obtained from Genelux corporation and used as indicator cells for viral titration (chapter 2.6) due to their susceptibility to infection with vaccinia virus (VACV).

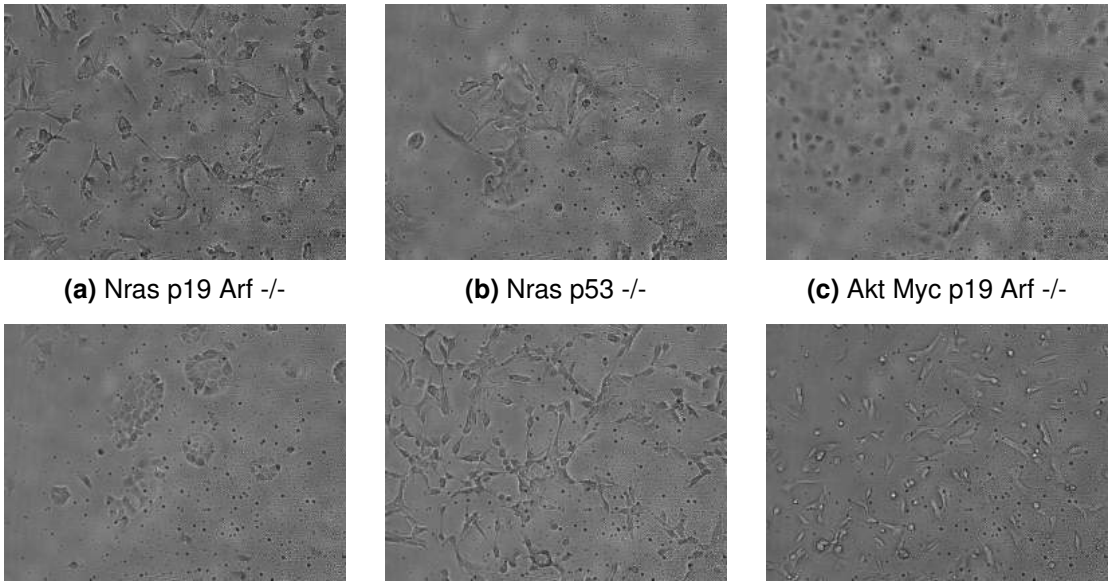

(a) Nras p19 Arf -/- **(b)** Nras p53 -/- **(c)** Akt Myc p19 Arf -/-

(d) Akt Myc p53 -/- **(e)** Nras Myc p19 Arf -/- **(f)** Nras Myc p53 -/-

Figure 10: Morphology of mHCC cell lines. Photos of mHCC cell lines in cell culture (x100). Photos were taken with an IX50 inverted phase contrast microscope.

2.2.2 Cultivation, Splitting and Harvest of Cells

All procedures requiring a sterile environment were carried out under a laminar flow safety work bench. Cell lines were cultivated in tissue culture flasks with filter caps (75 cm^2 and 175 cm^2). Standard culture medium (further simply re-

ferred to as "medium") used for all cell lines was composed of Dulbecco's modified Eagle's medium (DMEM) enriched with 5% fetal bovine serum (FBS) and 1% non-essential amino acids (NEAA). Cells were incubated at 37 °C in a humidified atmosphere with 5% CO_2 in a Hera-Cell incubator. The density of cells was controlled on a regular basis under a CK40 inverted phase contrast microscope and cells were split if the cell layer was near confluence. If not described other, all media, phosphate buffered saline (PBS) and trypsin-EDTA were prewarmed at 37 °C in a water bath before working with cell cultures.

For splitting of cells, medium was removed from the culture flask, and cells were rinsed with sterile Dulbecco's phosphate-buffered saline (DPBS). After removal of DPBS, trypsin-EDTA (0.05%) was added and cells were incubated at 37 °C for up to 5 min until they detached from the culture flask. Cells were resuspended in medium, transferred into a 15 mL centrifuge tube and centrifuged in a Megafuge 2.0 R at 1,000 rounds per minute (rpm) for 4 min at room temperature (RT). The supernatant was removed with a sterile pasteur pipette and cells were again resuspended in medium. A fraction of the cell suspension was transferred back into a culture flask while the remaining part was either discarded or used to seed cells into multiwell plates for further experiments.

2.2.3 Cryoconservation and Thawing of Cells

For cryoconservation, cells were harvested as described in the previous chapter. After centrifugation cell pellets were resuspended in cryoconservation medium comprising 50% FBS with 40% DMEM and 10% dimethyl sulfoxide (DMSO). The suspension was apportioned into cryoconservation tubes which were placed in a Mr. Frosty™ freezing container. The freezing container was stored overnight at -80 °C and cells were transferred the next day, either to a -150 °C freezer or into liquid nitrogen at -196 °C, where they were stored for long term conservation. After fewer than 30 passages cell lines were replaced with fresh cells to avoid genetic drift and maintain stable conditions for the experiments. Therefor prior cryoconserved cells were thawed and re-cultured. Cryotubes were placed in a water bath at 37 °C until all content was fluid. Under the workbench the cell suspension was transferred into a centrifuge tube containing prewarmed medium. The tube was centrifuged at 1,000 rpm for 4 min at RT. The cell pellet was suspended in

fresh medium and cells were cultivated in tissue culture flasks. Newly thawed cells were passaged at least once before being used for new experiments.

2.2.4 Determination of Cell Count with a Haemocytometer

Cell concentrations were determined using an improved Neubauer haemocytometer [99, 100]. A haemocytometer is a thick microscope slide that shapes counting chambers with a laser engraved grid pattern. A cell suspension was diluted (1:10 or 1:100) in trypan blue and vortexed thoroughly. The improved Neubauer haemocytometer was prepared by sliding a glass cover over the central area until Newton's rings were visible. Next, the chambers of the haemocytometer were loaded with 5-10 μL of the trypan blue cell dilution. The tip of the adjustable pipette was placed at the edge of the glass cover. Dilution was slowly pipetted on to the slide, allowing capillary forces to soak the dilution beneath the cover. Beneath a CK40 phase contrast microscope all non-blue colored, and therefor viable cells, in the four big corner squares (one square contains 100 nL) were counted. The cell concentration (in cells/mL) was calculated by multiplying the average number of cells in one big corner square with 10^4 and correcting for the dilution.

2.3 Oncolytic Vaccinia Virus GLV-0b347

The genetically modified vaccinia virus GLV-0b347 used in this thesis was developed by the Genelux Corporation (San Diego, USA). GLV-0b347 was created through modification of the western reserve strain of vaccinia virus. The nonessential JR2-gene, coding for viral thymidine kinase (TK), was knocked out by insertion of the turboFP635-gene (figure 11). This adds to its cancer specific properties by highly attenuating viral replication in healthy cells and restricting its replication to TK-expressing (replicating) cells. The turboFP635-gene (alias Katushka), controlled by a synthetic early/late promoter, codes for a far-red mutant of the red fluorescent protein from the sea anemone *Entacmaea quadricolor*. Excitation/emission maxima are at 588/635 nm [101].

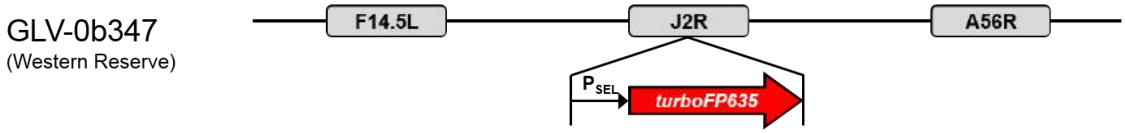

Figure 11: GLV-0b347 genetic modifications. Oral abstract from Chen et al. at the Society for Immunotherapy of Cancer (SITC) 27th Annual Meeting 2012. A56R: gene encoding Hemagglutinin (HA). F14.5L: open reading frame (ORF) encoding highly conserved polypeptide. J2R: Thymidine kinase (TK). PSEL: VACV synthetic early/late promoter. turboFP635: far red mutant of red fluorescent protein.

2.3.1 Infection of Cells with Vaccinia Virus GLV-0b347

All six mHCC cell lines were infected with GLV-0b347 to assess oncolytic effectiveness (chapter 2.5 and 2.7), viral replication (chapter 2.6), protein and RNA expression (chapter 2.8 and 2.9). The virus was tested using different concentrations, quantified in so called multiplicities of infection (MOI). A MOI of 1 represents one plaque forming unit (PFU) per cell. Various MOIs were employed for experiments, ranging from 0.0001 to 1. Therefor dilution series were prepared. Cells were infected either in 24- or 6-well plates and were usually seeded 24 hours before infection (hbi). Cell counts were adapted to the respective experiment, i.e. 2 x 10^4 cells for mHCC Nras p19 Arf -/-, Nras p53 -/-, Nras Myc p19 Arf -/- and Nras Myc p53 -/-; 2.5 x 10^4 cells for Akt Myc p19 Arf -/- and Akt Myc p53 -/- for viability assays. The virus was thawed on ice and sonicated for 30 seconds in a 4 °C cool water bath using a sonifier attached to a thermostatic circulator. This was necessary to separate aggregated viral particles. The virus was further diluted as needed in DMEM with 2% FBS. Before cells were infected, medium was removed, and cells were washed with sterile DPBS. Subsequently, 250 µL of inoculum were added per well. Cells were incubated in a separate incubator for infectious samples at 37 °C and 5% CO_2 for one hour. Every 15 min the plates were gently tilted to assure an even distribution. After incubation, the inoculum was removed and replaced with fresh medium. Lastly, the cells were placed back in the incubator.

2.4 Fluorescence Microscopy of GLV-0b347 Infected Cells

All mHCC cell lines were seeded in a 24-well plate and infected with GLV-0b347. At 72 and 96 hours post infection (hpi) cell lines were investigated under an IX50 inverted phase contrast and fluorescence microscope attached to a U-RFL-T power supply unit. Phase contrast photos were taken to document damage to the cell layer. Fluorescence photos were able to show the progress of infection, through depicting the expression of the far-red mutant fluorescent protein Katushka encoded by GLV-0b347. The exposure time of phase contrast photos was automatically adapted by the program AnalySIS for equal brightness. The fluorescence photos were taken with a constant exposure time of 300 ms. Digital phase contrast and fluorescence photos were overlaid using the GNU Image Manipulation Program (GIMP).

2.5 Sulforhodamine B (SRB) Cytotoxicity Assay

The Sulforhodamine B (SRB)-Assay was first described by Skehan et al. in 1990 and remains one of the most widely used in vitro cell cytotoxicity assays [102]. Its rapid implementation, high sensitivity and cost effectiveness make it favorable for large scale cytotoxicity screenings. Under mild acidic conditions the SRB dye binds to amino acid residues, prior fixated to the culture plate with trichloroacetic acid (TCA). Reversely, the dye dissolves under mild alkaline conditions. The amount of dye extracted from stained cells is proportional to their mass and can be quantified photometrically [103]. For this endpoint evaluating assay, cells were seeded in 24 well plates and infected as described in chapter 2.3.1. At 72 and 96 hpi medium was removed, cells were washed with ice-cold PBS and then fixated in 250 µL of 10% (w/v) TCA. The plate was incubated for at least 30 min at 4 °C. After incubation the TCA was discarded in special waste. Plates were washed with tap water and dried overnight at 40 °C in a drying chamber. The next day cells were stained with 250 µL of SRB staining solution (0.4% [w/v] SRB in 1% acetic acid). Plates were incubated for at least 10 min at RT. Afterwards plates were washed four times with 1% acetic acid to remove unbound dye. Plates were again

dried for at least 4 h or overnight. Protein bound dye was extracted with 1-2 mL of 10 mM (pH 10.5) unbuffered tris base (tris[hydroxymethyl]aminomethane). Plates were incubated for at least 10 min on a shaker, before 80 µL of the solutions were pipetted in duplicates into a 96-well micro plate. The optical density (OD) was determined at 550 nm (reference wavelength: 620 nm) with the Tecan Genios Plus microtiter plate reader. Data was processed with the XFluor 4 software. The resulting averaged values of each test group were plotted relative to the mock sample values, using the software GraphPad Prism 5.

2.6 Viral Growth Curves

To compare viral replication in different cell lines viral growth curves were established employing a plaque assay to determinate viral titers over time.

2.6.1 CMC Overlay Medium and Crystal Violet Stain

To prepare the virus plaquing overlay medium 7.5 g of carboxymethylcellulose (CMC) was added to a 500 mL glass bottle with a stir bar and autoclaved. Afterwards 500 mL of DMEM was added under sterile working conditions. The bottle was placed on a RTC basic magnetic stirrer overnight until the CMC was entirely dissolved. Then, 25 mL FBS and 5 mL of Penicillin/Streptomycin/Amphotericin-B-solution was added. After stirring for another 15 min the overlay medium was stored at 4 °C. Due to its high viscosity, the overlay medium was heated to 37 °C before usage.

The crystal violet stain was mixed by filling 0.65 g of crystal violet into a 500 mL glass bottle containing a stir bar and adding 25 mL ethanol. The solution was stirred for an hour before 150 mL of 37% formaldehyde were added. Lastly, the bottle was filled with ddH_2O to the top mark. The crystal violet stain was stored at RT.

2.6.2 Generation of Samples for Plaque Assay

For each cell line a 6-well plate with 1.5 or 2 x 10^5 cells/well was seeded, depending on the cell line. The next day, cells were infected with GLV-0b347 at a MOI of 0.075. Cells were rinsed with DPBS before incubation with 1 mL of inoculum for 1 hour in an incubator. Then the inoculum was removed, cells were rinsed with DPBS and 2 mL of fresh medium were added. Each well was scheduled for one time point: 1, 24, 48, 72 and 96 hpi. Cells were harvested at respective time points using a sterile cell scraper to detach cells from the ground of the well. Cells and supernatant were collected and transferred into a 2 mL microfuge cup and immediately frozen at -80 °C.

2.6.3 Titration of Samples on CV-1 Indicator Cells

The plaque assay was performed on simian CV-1 cells which are highly permissive to viral infection. CV-1 cells were seeded in a 24-well plate (one plate for two time points) with 1 x 10^5 cells per well. If cells were confluent the next day, they were infected with a dilution series derived from each infected sample. These were thawed in a water bath, thoroughly vortexed and placed on ice. The prior freezing achieves rupture of cell membranes and release of assembled virions. Shortly before preparation of the dilution series each sample was sonicated for 30 sec at 4 °C. A dilution series was prepared ranging from 1 to 10^{-6} parts of the original sample. The medium of two wells was removed and CV-1 cells were infected with 250 µL of the sample dilution. The infection schema depended on the timepoint of sample collection (time point 1 hpi: dilution ranged from 1-10^{-5}; 24 hpi: 10^{-1}-10^{-6}; 48, 72, 96 hpi: 10^{-2}-10^{-7}). Plates were gently swayed every 20 min while incubating at 37 °C and 5% CO_2. After one hour cells were overlaid with CMC-medium and placed back in the incubator for 48 hours. To visualize the plaques, 250 µL of crystal violet stain was added into each well on top of the CMC-medium and plates were incubated for at least 4 hours or overnight at RT. After incubation, all medium was removed and discarded in special waste. The wells were washed with tap water three times. After drying and UV-irradiation, plaques were manually counted under a magnifying glass.

2.6.4 Analysis of Plaque Assay Results

As every plaque originates from infection with one viral particle, the number of plaques corresponds to the titer of infectious particles. The unstained plaques are visible to the unaided eye in the layer of stained CV-1 cells (figure 12). Under a magnifying glass the number of plaques was counted. Only wells containing more than 6 and less than 90 plaques were considered and results were transcribed into a matrix. After enumeration, the virus titer was calculated by following equation: Viral titer [PFU/mL] = mean plaque count [PFU] / (dilution x volume of inoculum [mL]). The results of the plaque assay were plotted with GraphPad Prism 5 using a base-10 logarithmic scale for the Y-axis.

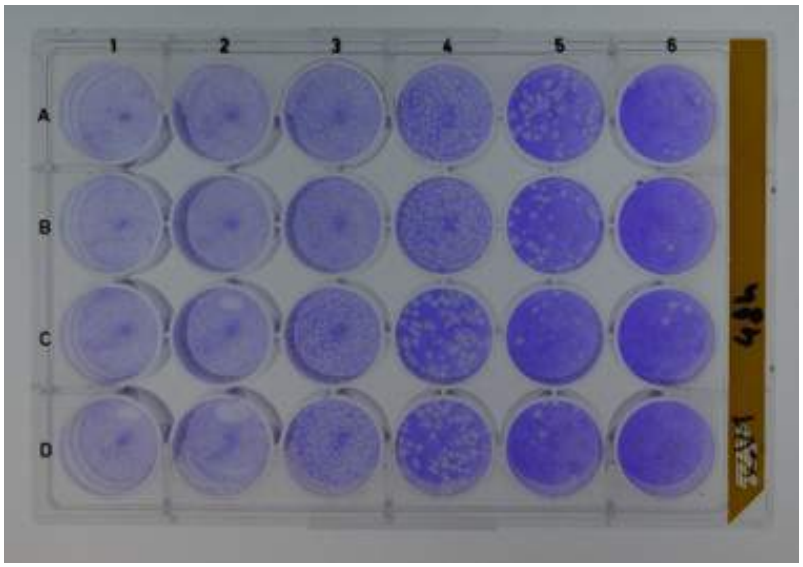

Figure 12: Crystal violet stain of infected CV-1 cells. The picture shows a 24-well plate seeded with CV-1 cells 48 hours after infection with virus samples and after staining with crystal violet. Rows A and B were infected with samples from Nras p19 Arf -/- while rows C and D were infected with samples from Nras p53 -/-. Columns 1-6 represent dilutions from 10^{-2} to 10^{-7}. Only the last two wells in rows A and B and the last three wells in rows C and D were counted.

2.7 Real Time Cell Analysis with xCELLigence

The xCELLigence system (ACEA Biosciences) is a novel non-invasive technique which allows a continuous monitoring of cell proliferation, morphology and viability. The assay relies on a measurable change in impedance caused by cells attached to the bottom surface of an electrode equipped 96-well E-plate. Real time data is continuously collected throughout the experiment while the instrument is placed inside an incubator and connected via cable to a control unit outside. The system uses special electronic microtiter plates (E-Plates), which have a specific gold electrode array at the bottom of each well covering 80% of the surface area. The data collected is reported by a unitless parameter named Cell Index (CI) which is calculated from a nominal impedance and the measured change of impedance to baseline [104].

2.7.1 Assessment of Cell Proliferation and Viability with xCELLigence RTCA

Murine HCC cell lines Nras p19 Arf -/-, Nras p53 -/-, Nras Myc p19 Arf -/- and Nras Myc p53 -/- were further investigated with the xCELLigence Real Time Cell Analyzer (RTCA). A 96-well E-Plate was prepared by pipetting 200 µL of PBS into the interspaces and 50 µL of medium into the wells using a mechanical multichannel pipette. Then a background measurement was performed. To assess proliferation, cell counts of 1000, 1500, 2000, 2500 and 3000 cells per well were chosen. Cells were sifted through a 40 µm cell strainer to dissolve aggregates before a cell count was performed. Next, cells were seeded into the wells in 150 µL of medium and the E-Plate was stationed inside an incubator (37 °C in a humidified atmosphere with 5% CO_2). For the assessment of cell viability, a cell count of 1000 cells per well was chosen. Cells were infected with 10 µL of GLV-0b347 24 hours after the initial seeding using MOIs of 1, 0.1, 0.01 and a mock. Also, a death control was performed by adding 10 µL of Triton X-100 leading to cell lysis. After infection, the E-Plate was stationed back inside the incubator and data was further collected every 30 min for 96 hpi.

2.8 Western Blot Analysis

2.8.1 Generation of Samples

Murine HCC cells (1.5 - 4 x 10^5) from each cell line were transferred into microcentrifuge tubes and centrifuged for 5 min at 4500 rpm at 4 °C. Supernatant was carefully removed and the pellet was resuspended in 50-100 µL of lysis buffer (table 1). Samples were stored at -20 °C. To further process the cell sample, cell lysis was achieved through three freeze-thaw cycles with liquid nitrogen. Microcentrifuge tubes containing the samples were thawed in a block heater and subsequently frozen in liquid nitrogen again, three times in a row. Afterwards the samples were centrifuged (for 10 min at 13000 rpm and 4 °C) to remove cell debris. Cleared lysate was transferred into a new tube and stored at -20 °C.

Table 1: Buffers and Solutions for Western Blot.

Buffer/Solution	Composition
Tris-buffered saline (TBS) (pH 7.4)	NaCl 150 mM, Tris 50 mM, pH adjustment with HCl (37%)
Dilution and wash buffer: TBS-Tween™ (TBS-T)	TBS (pH 7.4), 0.02% Tween-20
1x Transfer buffer	Tris 48 mM, Glycin 39 mM, MeOH 20%
5x PAGE running buffer (pH 8.3)	Tris 125 mM, Glycine 950 mM, SDS 0.5 % (m/v), pH adjustment with HCl (37%)
10x Ponceau dye	0.1% Ponceau, 5% acetic acide
Cell lysis buffer	Tris 50 mM (pH 7.6), NaCl 150 mM, IGEPAL 10%, H_2O
6x Loading buffer	0.125% bromophenol blue, 40% sucrose, 0.1% SDS
Stripping buffer	β-mercaptoethanol 100 mM, SDS 2%, TBS (pH 6.7) 62.5 mM

2.8.2 Bradford Assay for Protein Quantification

The Bradford protein assay, developed by Marion M. Bradford in 1976, is an easy colorimetrical method to quantify the amount of protein in a solution [105]. The interaction of protein with Coomassie Brilliant Blue G-250 dye under acidic conditions results in a shift of light absorbance. The unbound cationic red/green form of the dye has an absorbance maximum at 465 nm, while the anionic blue form binds the proteins' carboxyl and amino groups and has its absorbance maximum

at 595 nm. The increased absorbance at 595 nm is proportional to the amount of protein. The Bradford assay was performed to determine the protein concentration in the samples further used for western blot analysis. First, a standard curve was generated through a dilution series of bovine serum albumin (BSA). Samples of 0.5, 0.25, 0.1, 0.05 and 0.00 mg/mL BSA in ddH_2O were prepared. The protein samples were diluted 1:20 or 1:40 and 10 µL of each sample were pipetted in duplicates into a 96-well plate. The Bradford dye was diluted 1:5 with ddH_2O and 200 µL were added to each sample in the 96-well plate. After 5 min the absorbance at 595 nm was measured with the Tecan Genios Plus microplate reader using the Magellan software. The software automatically calculates the amount of protein in each sample, as well as the volume of sample containing exactly 50 µg of protein.

2.8.3 Sodium Dodecyl Sulfate-Polyacrylamide Gel Electrophoresis

Sodium Dodecyl Sulfate-Polyacrylamide Gel Electrophoresis (SDS-PAGE) is an analytical method in biotechnology, developed by Ulrich K. Laemmli in 1970 [106], which uses an electric field to separate a mixture of charged proteins according to their molecular weight. The electrical field forces negatively charged unfolded proteins through the molecular mesh of a polyacrylamide gel towards the anode. While an ordinary PAGE separates macromolecules by their electrophoretic mobility (depending on length, conformation and charge), sodium dodecyl sulfate (SDS) unfolds proteins and covers their intrinsic charge, allowing separation depending solely on the mass of the proteins.

Preparation of Gel

For western blot analysis equipment from Bio-Rad was used. Glass plates were cleaned with 70% isopropanol before assembly in plastic frames. After the composed glass plates were checked for leakage with ddH_2O, the separating gel (8% acrylamide) was prepared as described in table 2 and filled into the glass frame up to 0.5 cm beneath the estimated height of the wells. Then isopropanol was filled

on top of the gel to form a level horizontal edge. After 15 min the gel had polymerized, and the isopropanol was discarded. The stacking gel (5% acrylamide) was prepared (table 2) and poured on top of the separating gel, subsequently a comb was placed into the liquid stacking gel. After the stacking gel had polymerized as well, the gel/glass plates were taken out of their plastic frame and either stored in wet paper towels at 4 °C or directly placed inside an electrophoresis chamber. Before loading samples, the chamber was filled with running buffer, so that every well was immersed in buffer.

Table 2: Composition of separating and stacking gel

Components	Seperating gel (8%)	Stacking gel (5%)
Overall amount	20 mL	6 mL
ddH_2O	9.3 mL	4.1 mL
Acrylamide 30%	5.3 mL	1 mL
Tris-HCl 1M (pH 6.8)	-	0.75 mL
Tris-HCl 1.5 M (pH 8.8)	5.0 mL	-
SDS 10%	0.2 mL	0.06 mL
APS 10%	0.2 mL	0.06 mL
TEMED	0.012 mL	0.006 mL

APS: Ammoniumpersulfate. SDS: Sodium dodecyl sulfate. TEMED: Tetramethylethylenediamine.

Preparation of Samples

The samples were thawed and a volume containing exactly 50 µg of protein, was transferred into a microcentrifuge tube. Then 1/5 of that volume of loading buffer (6 x), containing bromophenol blue and β-mercaptoethanol, was added under a fume hood. The tube was briefly centrifuged and placed in a heating block at 95 °C for 5 min to break secondary and tertiary structures of the proteins. Afterwards the tube was again briefly centrifuged. The first well was always loaded with 5 µL of a molecular weight marker (PageRuler™). Every sample was loaded with a pipette into its own well. An electrical voltage of 70 V was applied, forcing the samples out of their well and collecting them at the verge of the separating gel. After all samples were located on an even horizontal the electrical current was set to a constant 40 mA. The power was disconnected after the colored front reached the end of the gel.

2.8.4 Electroblotting

In order to conserve the patterns of separated proteins, the proteins were fixed on a polyvinylidene fluoride (PVDF) membrane through electroblotting. The sandwich frame, sponge and Whatman paper were placed in a tub filled with transfer buffer and soaked, before assembly according to figure 13. After the gel had been carefully detached from the glass frame and placed on the Whatman paper, the PVDF-membrane was briefly immersed in methanol before being rinsed in ddH_2O and placed on the gel. A round glass tube was used to remove all air trapped between the gel and the membrane. After the blot-sandwich was prepared, it was placed inside the blotting chamber with caution, placing the anode on the side of the PVDF-membrane. Then, a cool battery was placed next to the sandwich into the blotting-chamber to avoid overheating during the blotting process and the chamber was filled with transfer buffer. Finally, the whole apparatus was connected to a power supply and run at 300 mA for 1 hour. After blotting the membrane was fixed in methanol and dried. Then the marker bands were marked with a pen on the membrane.

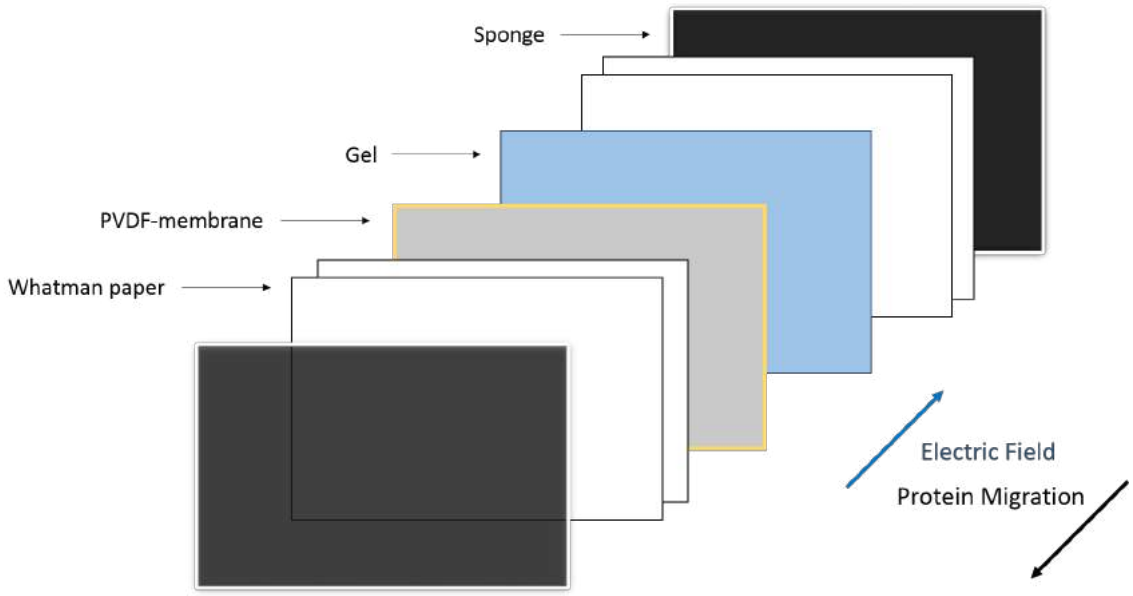

Figure 13: Assembly of sandwich for electroblot.

2.8.5 Immunologic Detection Methods

To detect specific proteins on the membrane, the membranes were incubated with antibodies. First, membranes were incubated in TBS-T with 5% (w/v) non-fat dry milk or in Roti®-block for at least 1 hour at RT on an orbital shaker to block unspecific binding sites. Then the membrane was washed 3 x 10 min in TBS-T and incubated overnight at 4 °C on an orbital shaker with the primary antibody (table 3). The next day membranes were washed 3 x 10 min in TBS-T and incubated with a horseradish peroxidase (HRP) conjugated secondary antibody for 1 hour on a shaker at RT, according to corresponding species of the primary antibody. The membrane was again washed at least 3 x 10 min in TBS-T. Then proteins could be detected through chemiluminescence using the ECL™ Western Blotting Detection Reagent (GE Healthcare). Equal parts of the two reagents (Solution A: Luminol, and Solution B: Peroxide) were mixed and poured onto the membranes. After one minute of incubation supernatant was discarded and the membrane was placed in a plastic seal. At the site of antibody bound protein the HRP catalyzes the oxidation of luminol with hydrogen peroxide into a dianion. The following reaction of the dianion with oxygen produces (unstable) luminol endoperoxide, which ultimately decays into nitrogen and 3-aminophthalic acid, causing the emission of light at 428 nm (blue). The emitted light was detected on a photosensitive film in a darkroom.

If the membrane was intended to be reused, all antibodies were removed from the membrane. This was achieved through incubation of the membrane in stripping buffer (table 1) for 30 min at 50 °C and subsequent washing in large volumes of TBS-T.

Table 3: Antibodies

	Target	Species	Preparation in TBS-T	Manufacturer
Primary antibodies	Vinculin	Mouse	1:8000 with 5% milk	Sigma-Aldrich
	p53	Mouse	1:200	Santa Cruz BT.
Secondary antibodies	Mouse IgG	Goat	1:8000 with 5% milk	Bio Rad

2.9 Reverse Transcription Quantitative Polymerase Chain Reaction

2.9.1 Generation of pure RNA Samples and Reverse Transcription into cDNA

Nras p19 Arf -/- and Nras p53 -/- cells were each seeded in a 6-well plate with 2 x 10^5 and 2.5 x 10^5 cells per well, respectively. After 24 hours, 3 wells were infected with GLV-0b347 at a MOI of 0.075 and 3 wells were mock infected. At 24 hpi, the medium was removed and cells from 2 wells were collected in DPBS, using a sterile cell scraper. Cells were transferred into a 2 mL tube and centrifuged at 4,500 rpm for 5 min at 4 °C. The supernatant was removed, and the pellet was further processed to extract RNA using the NucleoSpin® RNA isolation kit. For detailed description of the RNA isolation process refer to the NucleoSpin RNA user manual. RNA purity and concentration were reviewed with the NanoDrop™ 1000 spectrophotometer and NanoDrop-1000 software. Samples were frozen at -80 °C. The RNA was further transcribed into cDNA using the RT^2 First Strand Kit (Qiagen) according to the instructions in the RT2 Profiler PCR Array Handbook (Dec 2014). 5 µg of total RNA per reaction were used. Genomic DNA contaminations were removed with the "elimination mix" and subsequently cDNA was synthesized with the "reaction mix". For detailed description of cDNA synthesis process refer to the manual. Lastly, probes were analyzed with the NanoDrop™ 1000 spectrophotometer and NanoDrop-1000 software, and stored at -20 °C.

2.9.2 Real-Time PCR with RT2 Profiler Array

According to the RT^2 Profiler PCR Array Handbook, the synthesized cDNA (102 µL) was mixed with 2x RT^2 SYBR Green Mastermix (1350 µL) and RNase-free water (1248 µL) to obtain the "PCR components mix". The mix was pipetted into the RT^2 Profiler PCR Array plate (figure 14) containing the pre-dispensed gene-specific primer sets using a multichannel pipette and RNAse/DNAse free tips. The plate was briefly centrifuged (1300 rpm, 1 min) to remove bubbles. Afterwards the

	1	2	3	4	5	6	7	8	9	10	11	12
A	Aim2	Atg12	Atg5	Azi2	Card9	Casp1	Casp8	Ccl3	Ccl4	Ccl5	Cd40	Cd80
B	Cd86	Chuk	Cnpy3	Ctsb	Ctsl	Ctss	Cxcl10	Cxcl11	Cxcl9	Cyld	Dak	Ddx3x
C	Ddx58	Dhx58	Fadd	Fos	Hsp90aa1	Ifih1	Ifna2	Ifnar1	Ifnb1	Ikbkb	Il12a	Il12b
D	Il15	Il18	Il1b	Il6	Irak1	Irf3	Irf5	Irf7	Isg15	Jun	Map2k1	Map2k3
E	Map3k1	Map3k7	Mapk1	Mapk14	Mapk3	Mapk8	Mavs	Mefv	Mx1	Myd88	Nfkb1	Nfkbia
F	Nlrp3	Nod2	Oas2	Pin1	Pstpip1	Pycard	Rela	Ripk1	Spp1	Stat1	Sugt1	Tank
G	Tbk1	Tbkbp1	Ticam1	Tlr3	Tlr7	Tlr8	Tlr9	Tnf	Tradd	Traf3	Traf6	Trim25
H	Actb	B2m	Gapdh	Gusb	Hsp90ab1	MGDC	RTC	RTC	RTC	PPC	PPC	PPC

Figure 14: RT^2 Profiler PCR array "mouse antiviral response" 96-well layout. A comprehensive list of all genes with further information can be found in the appendix A.3. MGDC: Mouse genomic DNA contamination. RTC: Reverse transcription control. PPC: Positive transcription control.

Table 4: PCR-program

Repeats	Settings (temperature, time)	Description
1	95° C, 10:00	Activation of taq polymerase
40	95° C, 00:15 60° C, 01:00	Fluorescence measurement
1	95° C, 00:15 60° C, 01:00 95° C, 00:15 60° C, 00:15	Melting plot

array was immediately placed on ice. The experiment was then carried out using an Applied Biosystems 7300 real-time PCR system. The cycler was programmed as described in table 4. After the experiment, the array was discarded.

2.9.3 RT-qPCR Data Analysis Using the ΔΔCT Method

The data was further processed using the AB 7300 software. Baseline was set automatically while the threshold was set to 0.3 ΔRn (above background signal and within the lower half to the lower third of the linear phase). The C^T values of all wells were exported into a blanc excel sheet and transferred into a template excel sheet from Qiagen for web-based analysis. The arrays contain proprietary controls: The reverse transcription controls (RTC), the positive PCR controls (PPC) and the genomic DNA controls (GDC). Three different quality controls were performed concerning (i) PCR array reproducibility, (ii) reverse transcription efficiency and (iii) genomic DNA contamination. The first was reviewed by comparing the average C^T (PPC) of the samples. If they were no further apart than 2 cycles, they were considered pass. Reverse transcription efficiency was reviewed by the ΔC^T (average RTC minus average PPC) value. If they were smaller then 5, the test

was considered pass. For the last, the C^T values of the genomic DNA controls (GDC) were examined and considered pass if they were higher than 35, indicating the absence of genomic DNA contamination.

After these quality controls all C^T values higher than 35 or N/A (not detected) were set to 35 and were considered negative. Then the ΔC^T was calculated for each of the 84 pathway focused genes of interest (GOI) by subtracting the mean C^T value of the house keeping genes (HKG) from the C^T value of the GOI: $\Delta C^T_{GOI} = C^T_{GOI} - C^T_{HKG}$. With this value one can calculate the normalized gene expression ($2^{-\Delta CT(GOI)}$), which represents the expression of the GIO normalized to the HKG. To identify the induction or depression of GOIs between control and test sample, the $\Delta\Delta C^T$ value was calculated next, through subtraction of the ΔC^T(control) from the ΔC^T(test) value: $\Delta\Delta C^T_{GOI} = \Delta C^T_{Test} - \Delta C^T_{Control}$. Then the fold-change was determined through the following calculation: Fold-change = $2^{-\Delta\Delta CT}$. This number represents the factor by which the GOI is over- or under-expressed relative to the control sample. Results were processed and graphs generated using GraphPad Prism 5.

3 Results

3.1 Immunoblot Verifies Expected p53-Knockout in mHCC Cell Lines

Western blots and immunologic detection methods were utilized to confirm the knockout of TP53 in the mHCC cell lines. The blot in figure 15 shows the results: Nras p19 Arf -/-, Akt Myc p19 Arf -/- and Nras Myc p19 Arf -/- tested p53 positive, while Nras p53 -/-, Akt Myc p53 -/- and Nras Myc p53 -/- were p53 negative. All mHCC cell lines therefore showed the expected p53-expression pattern.

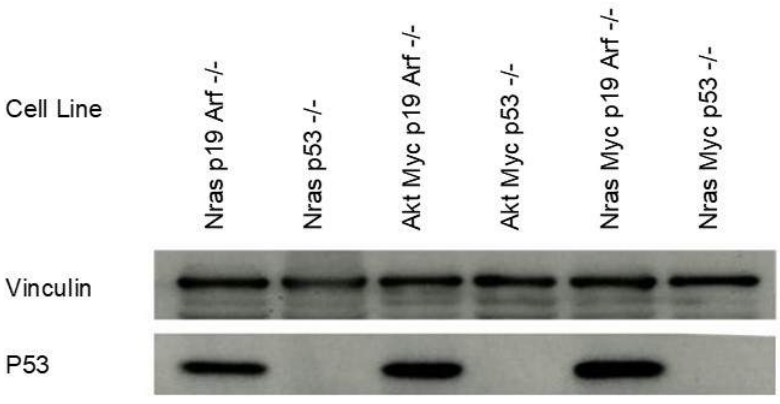

Figure 15: Confirmation of p53 presence and knock-out through immunoblot. Upper bands: Vinculin. lower bands: p53.

3.2 Microscopy Reveals Viral Infection and Damage to mHCC Cell Layer

All six murine HCC cell lines were infected with GLV-0b347 employing multiplicities of infection (MOIs) ranging from 1 to 0.0001. Photos were taken at 72 and 96 hours post infection (hpi) to catalogue damage to the cell layer and expression of the far-red fluorescent protein Katushka encoded by GLV-0b347. Positive fluorescence signals showed successful infection and traced viral spread from cell to cell. Phase contrast photos allowed to assess the lytic effectiveness of the virus by comparing the scope and morphology of cell layer damage. Phase contrast photos and corresponding fluorescence photos were overlaid. Photos of MOI 0.0001 are not shown.

Figure 16 shows first signs of infection in Nras p19 Arf -/- at an MOI of 0.001 at 72 hpi. The cell layer was damaged and showed morphological changes and fluorescence in few cells. At MOI 0.01 widespread infection and cell damage was seen at 72 hpi. The cell layer had lost its continuity and big detached cell rafts emitting bright red signal were seen. Almost all cells changed morphology from fusiform to spherical, showing that they were infected. At MOIs 0.1 and 1 cells had completely detached from the surface. At an MOI of 1, only smaller cell residues were left emitting less signal. At 96 hpi most cells had died, and a weak signal was emitted by a few left-over viable cells.

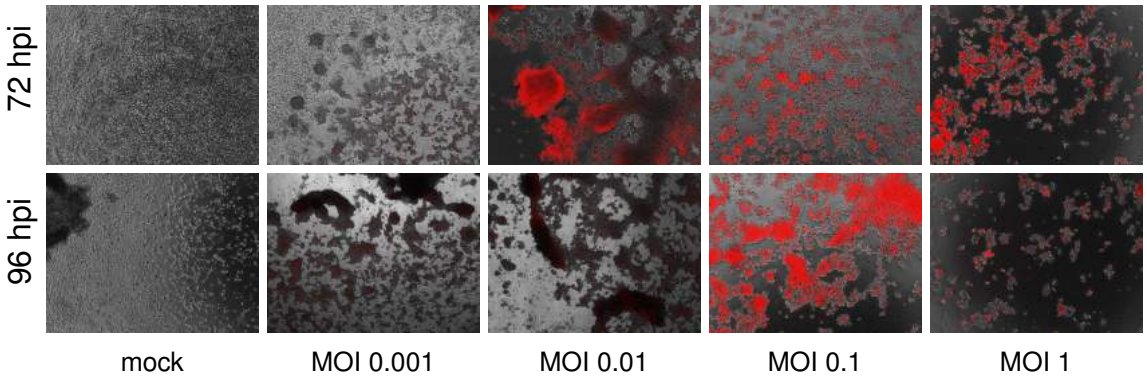

Figure 16: Nras p19 Arf -/-. Cells were infected with GLV-0b347 at MOIs ranging from 0.001 to 1 or mock infected. Red signal shows the expression of TurboFP635. Phase contrast and corresponding fluorescence photos were overlaid.

Nras p53 -/- showed first signs of cell damage and fluorescence signal at 72 hpi and an MOI of 0.01 (figure 17). Viral plaques were visible in the cell layer with

altered cell morphology at the rim and strong red fluorescent signal. At 96 hpi the infection had spread, and plaques had expanded. At an MOI of 0.1 the whole cell layer was affected. Almost all cells showed changes in morphology and emitted red fluorescence. At an MOI of 1 all cells were infected emitting bright red signals and were detached from the culture plate.

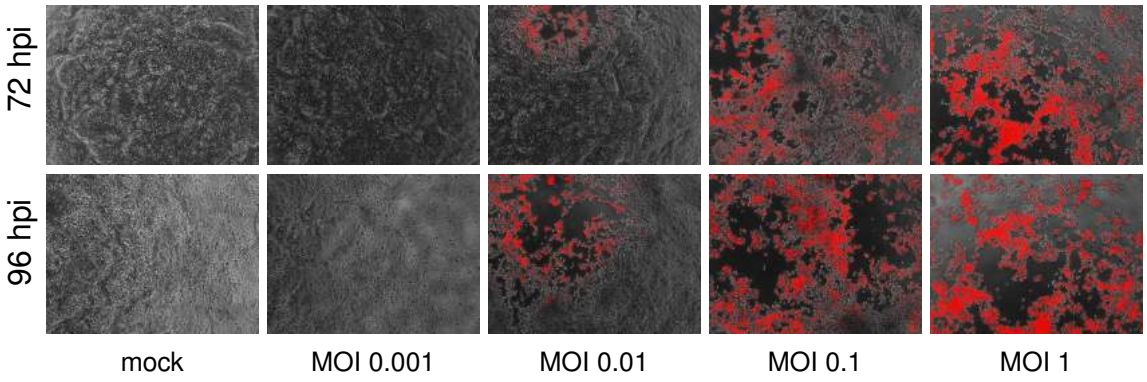

Figure 17: Nras p53 -/-. Cells were infected with GLV-0b347 at MOIs ranging from 0.001 to 1 or mock infected. Red signal shows the expression of TurboFP635. Phase contrast and corresponding fluorescence photos were overlaid.

Akt Myc p19 Arf -/- (figure 18) showed earliest fluorescence signs at 96 hpi at an MOI of 0.001. At an MOI of 0.01 small isolated plaques in the cell layer emitting fluorescent signals were detectable 72 hpi. At an MOI of 0.1 the plaques were bigger and showed a cell free center. At 72 hpi at an MOI of 1 almost all cells were infected and detached. At 96 hpi the entire cell layer was damaged with all infected cells showing a change in morphology and emitting red fluorescent signal. Cells that did not emit any signal were dead.

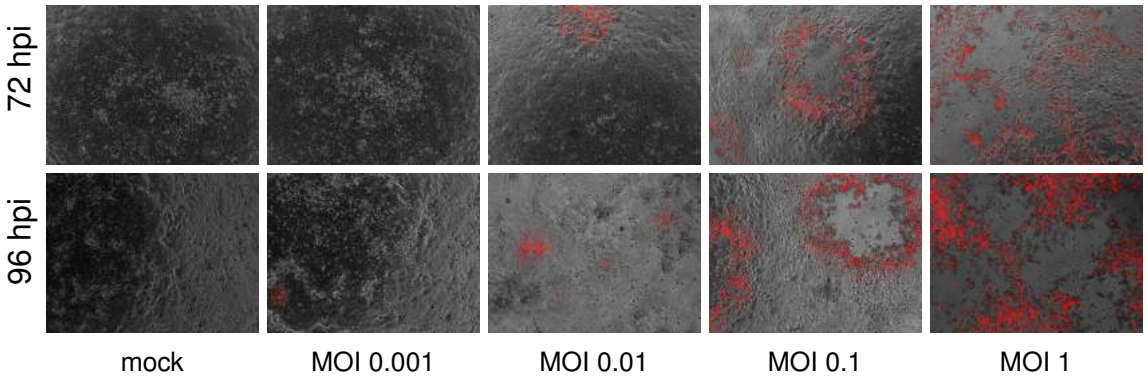

Figure 18: Akt Myc p19 Arf -/-. Cells were infected with GLV-0b347 at MOIs ranging from 0.001 to 1 or mock infected. Red signal shows the expression of TurboFP635. Phase contrast and corresponding fluorescence photos were overlaid.

Akt Myc p53 -/- (figure 19) showed an early lesion 72 hpi at an MOI of 0.001. At an MOI of 0.01 plaques were visible with fluorescent signal infiltrating the intact

cell layer. At 96 hpi many cells showed a more spherical morphology. At MOI 0.1 the infection had spread through the cell layer. An MOI of 1 caused massive infection and destruction of the cell layer, leaving only infected red fluorescent cells and cell debris.

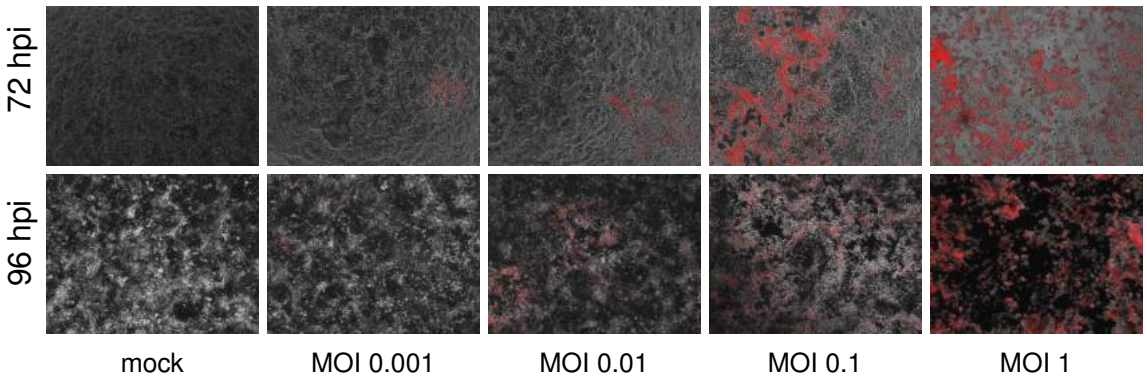

Figure 19: Akt Myc p53 -/-. Cells were infected with GLV-0b347 at MOIs ranging from 0.001 to 1 or mock infected. Red signal shows the expression of TurboFP635. Phase contrast and corresponding fluorescence photos were overlaid.

Nras Myc p19 Arf -/- showed plaques already at MOI 0.001 at 72 hpi (figure 20). The area of damage increased with increasing MOI, becoming confluent at an MOI of 0.1. At an MOI of 1 all cells were infected and detached. At 96 hpi cell damage had slightly increased, but fluorescence signal had faded remarkably. 96 hpi at an MOI of 1 only cell debris was left.

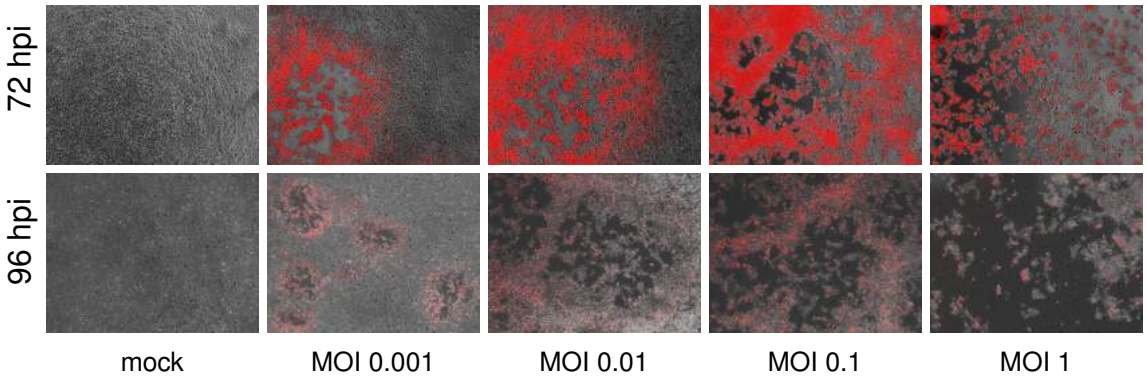

Figure 20: Nras Myc p19 Arf -/-. Cells were infected with GLV-0b347 at MOIs ranging from 0.001 to 1 or mock infected. Red signal shows the expression of TurboFP635. Phase contrast and corresponding fluorescence photos were overlaid.

In Nras Myc p53 -/- infection was detected at an MOI of 0.001 at 96 hpi (figure 21). At an MOI of 0.01 single plaques were visible with infected cells at their rim emitting fluorescence signal as well as infected and dead cells in the center. At an MOI of 0.1 the infection had spread over the entire cell layer. Much of

the area emitted bright red signal. At an MOI of 1 the cell layer had completely disintegrated with many cells emitting a strong fluorescent signal.

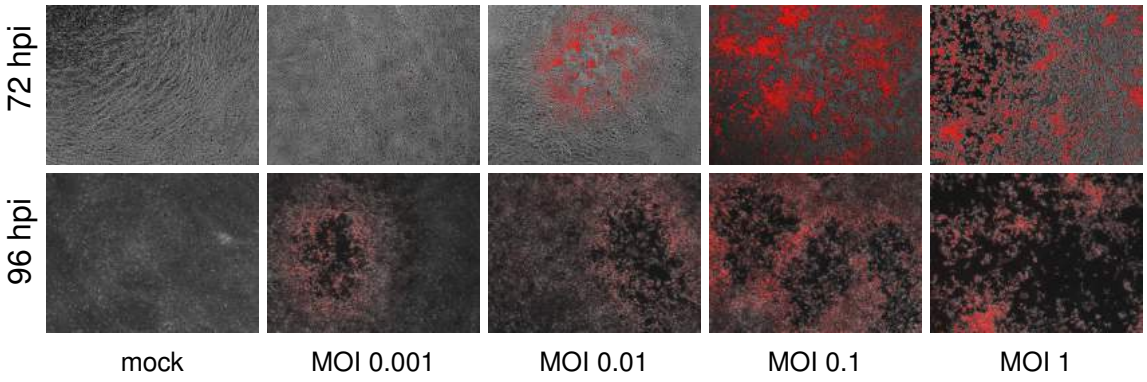

Figure 21: Nras Myc p53 -/-. Cells were infected with GLV-0b347 at MOIs ranging from 0.001 to 1 or mock infected. Red signal shows the expression of TurboFP635. Phase contrast and corresponding fluorescence photos were overlaid.

Figure 22 shows how a higher viral dosage caused an increased number of initial centers of infection, damaging the cell layer. These regions expanded and eventually grew confluent.

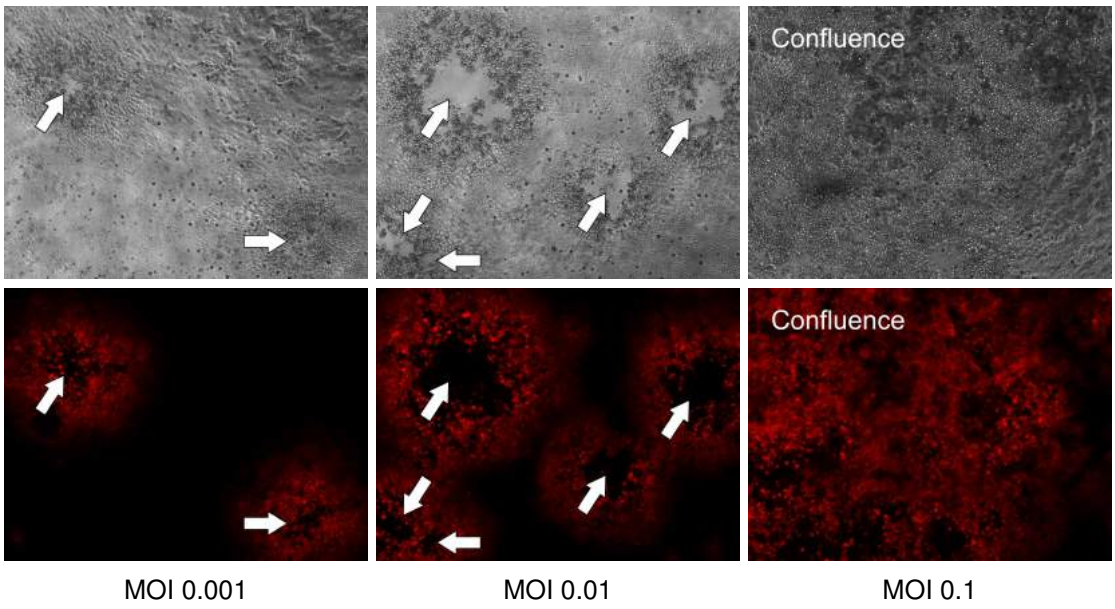

Figure 22: Exemplary phase contrast and fluorescence photos of Akt Myc p19 Arf -/- 72 hpi. Cells were infected with GLV-0b347 at MOIs ranging from 0.001 to 1. Red signal shows the expression of TurboFP635. White arrows indicate centers of initial infections forming plaques.

3.3 Murine HCC Cell Lines Show Different Susceptibility to GLV-0b347-Mediated Oncolysis

To assess the oncolytic effectiveness of GLV-0b347, all six mHCC cell lines were infected with GLV-0b347 at MOIs ranging from 0.0001 to 1. At 72 and 96 hpi phase contrast and fluorescence photos were taken before a Sulforhodamine B assay was performed. The remaining cell mass of each cell line at mentioned time points was assessed. The results are shown in figure 23. The cell line Nras p19 Arf -/- showed the greatest reduction in cell mass both at 72 and 96 hpi. The mean remaining cell mass at an MOI of 1 at 72 hpi was 31.5% and dropped to 9.4% at 96 hpi. Second highest reduction at 96 hpi was detected in Nras Myc p19 Arf -/- (32.6%) followed by Nras Myc p53 -/- (65.3%), Nras p53 -/- (73.6%), Akt Myc p19 Arf -/- (80.5%), and lastly Akt Myc p53 -/- (83.3%). Cell line Akt Myc p53 -/- showed an unexpected increase in remaining cell mass at 72 hpi at all viral concentrations.

3.3.1 Grouping of mHCC Cell Lines Based on Viability Assay Results

Based on the lytic performance of the virus, the cell lines were grouped according to their susceptibility. Figure 24 compares the remaining cell mass of all six mHCC cell lines 96 hpi at an MOI of 1. Those cell lines with residual cell masses of less than 50% were considered susceptible to GLV-0b347-mediated oncolysis. Cell lines with a remaining cell mass between 50 and 75% were considered moderately susceptible and of more than 75% resistant to oncolysis (the thresholds are indicated by dotted lines). According to this definition cell lines Nras p19 Arf -/- and Nras Myc p19 Arf -/- were susceptible, cell lines Nras Myc p53 -/- and Nras p53 -/- were moderately susceptible and cell lines Akt Myc p19 Arf -/- and Akt Myc p53 -/- were considered resistant.

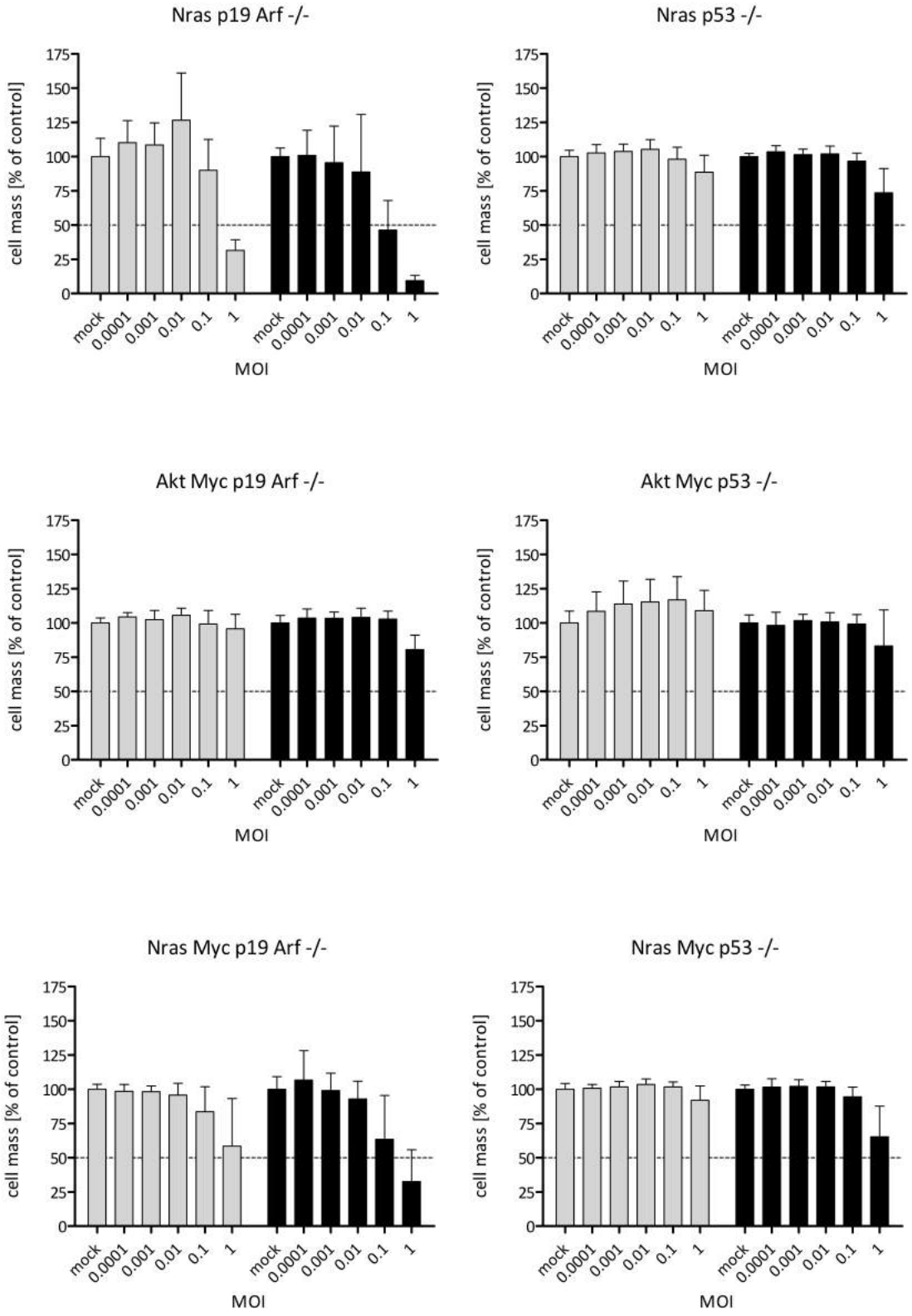

Figure 23: SRB-assay results of mHCC cell lines post infection with GLV-0b347. Cell lines were infected with the indicated MOIs. SRB-assays were performed at 72 and 96 hpi to determine cell viability. Each panel shows the determined cell mass of one mHCC cell line relative to control at 72 (left, gray bars) and at 96 hours (right, black bars) post infection (hpi). The bar graphs show arithmetic mean and standard deviation of four independent experiments. Dotted lines indicate 50%.

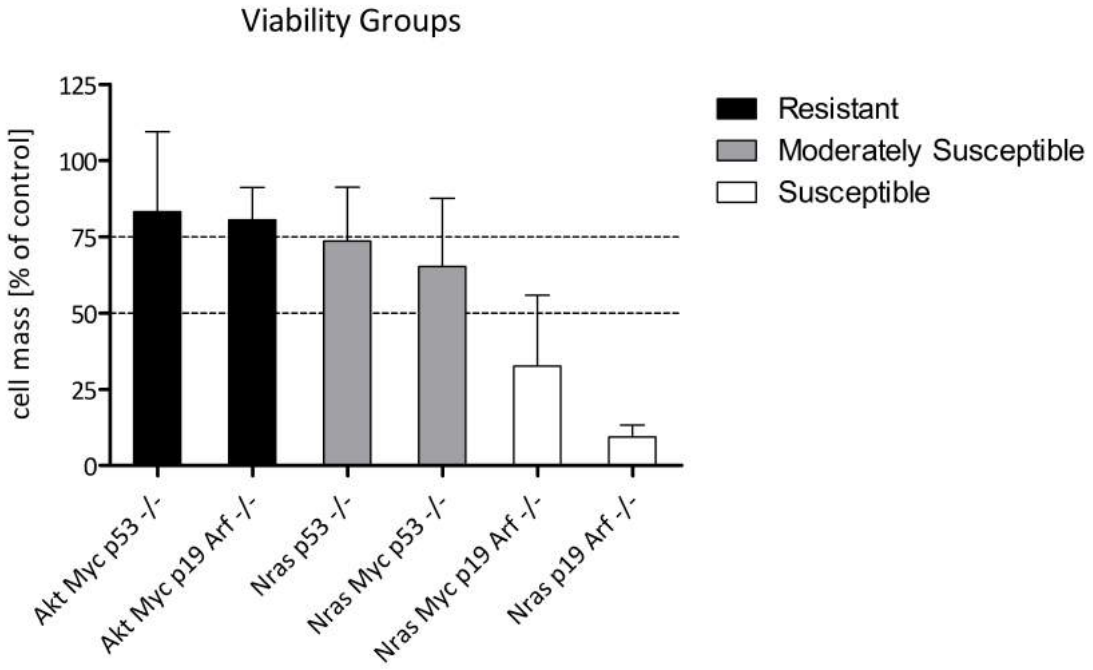

Figure 24: Viability groups. The remaining cell mass of all mHCC cell lines 96 hpi with GLV-0b347 at an MOI of 1 are shown in comparison. The results are displayed as mean and standard deviation of the remaining cell mass in percent of control. The cell lines are ordered by declining mean values. Dotted lines indicate 75% and 50% of the mock value. MHCC with cell masses above 75% were considered resistant (black), between 75% and 50% moderately susceptible (grey) and beneath 50% susceptible (white). SRB: Sulforhodamine B. MOI: multiplicity of infection. hpi: hours post infection.

3.4 Continuous Observation of the Viability of mHCC Cell Lines after GLV-0b347 Infection

Prior to continuous observation of the viability of cell lines Nras p19 Arf -/-, Nras p53 -/-, Nras Myc p19 Arf -/- and Nras Myc p53 -/- post infection, the proliferation rate of the respective mHCC cell lines was explored using the xCELLigence real time cell analyzer (RTCA). This was necessary to determine the optimal cell number to run the subsequent viability experiments. Since the experiment was designed as a long-term measurement ($>$ 48 h), a long exponential growth phase was needed. The following cell concentrations were seeded: 10000, 7500, 5000, 2500 and 1000 cells per well, in at least triplets. The impedance at the well bottom was measured in regular 30 min intervals and normalized to the baseline impedance with medium only. Figure 25 shows selected results for 7500, 2500 and 1000 cells per well with data points displayed every 4 hours. Analysis of the graphs revealed that all four cell lines had different proliferation profiles.

3.4.1 Pretests Show Fast Proliferation Profile of mHCC Cell Lines in xCELLigence RTCA

The first experiments with 7500 cells per well showed a similar position of the vertices of three cell lines at around 52 h. The mean cell index (CI) of the vertices though differed with 5.1 for Nras p53 -/-, 3.2 for Nras Myc p19 Arf -/- and 1.9 for Nras p19 Arf -/-. The vertex of Nras Myc p53 -/- was reached after 72 h and had a mean CI of 4.8. Subfigure 25b shows an experiment with 2500 cells per well, revealing a similar constellation. The cell lines Nras p53 -/-, Nras Myc p19 Arf -/- and Nras p19 Arf -/- had early vertices (between 64 and 68 h) with mean CI similar to the first experiment, 5.1, 3.1 and 1.8 respectively. Nras Myc p53 -/- showed a late vertex at 92 h with a mean value of 5.2. The last graph represents an experiment with only 1000 cells per well. During the first 64 hours the curves of all four cell lines did not diverge far from each other. A clear distinction in CI appeared earliest after 68 hours. Nras Myc p19 Arf -/- and Nras p19 Arf -/- had the earliest vertices at around 80 h with the lowest mean CI-values of 2.2 and 1.5, respectively. Nras Myc p53 -/- had its vertex later at around 96 h at the right outer limit of the graph. The value was again high, at 5.6. The cell line Nras p53 -/- did not show a vertex on the graph. The cell index increased steadily until it reached its highest measured value 3.5 at the end of the graph at 96 hours.

3.4.2 Real Time Monitoring of Virus Mediated Oncolysis in mHCC Cell Lines

To continuously monitor GLV-0b347 mediated oncolysis and to compare its effectiveness in the distinguished mHCC cell lines, an xCELLigence real time cell monitoring assay was performed. The mHCC cell lines were seeded with 1000 cells per well into 96-well E-plates. After 24 hours cells were infected at MOIs 1, 0.1 and 0.01. Triton X-100 was added as a control for complete cell lysis. Data was collected for further 96 hours. The results can be best compared between cell lines at defined time points. Figure 26 shows the continuous measurement of the cell index (CI) as well as the cell index at distinct time points 48, 72 and 96 hpi (bar graphs) for MOIs 0.1 and 1. In the susceptible cell line Nras p19 Arf -/- (subfigure 26a) no oncolysis was measured during the first 48 hpi. At 72 hpi an

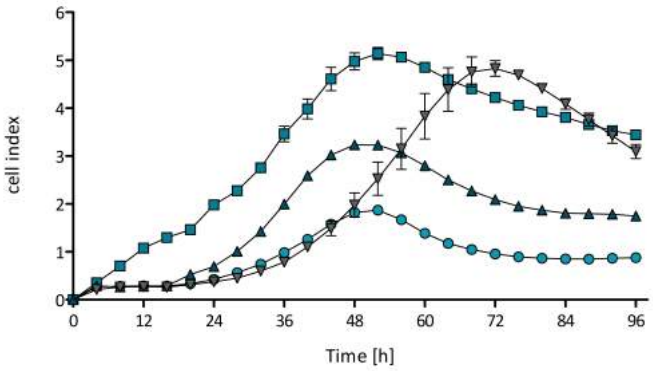

(a) 7500 cells per well

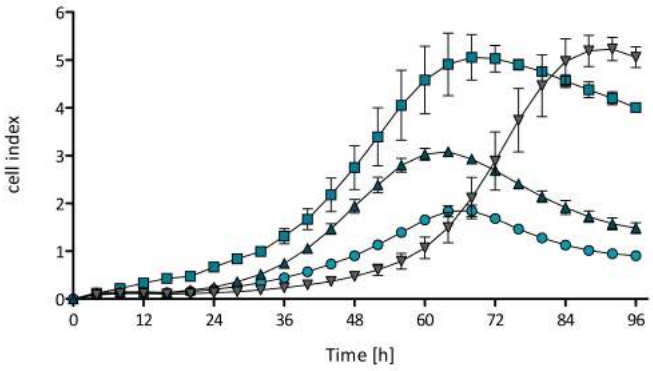

(b) 2500 cells per well

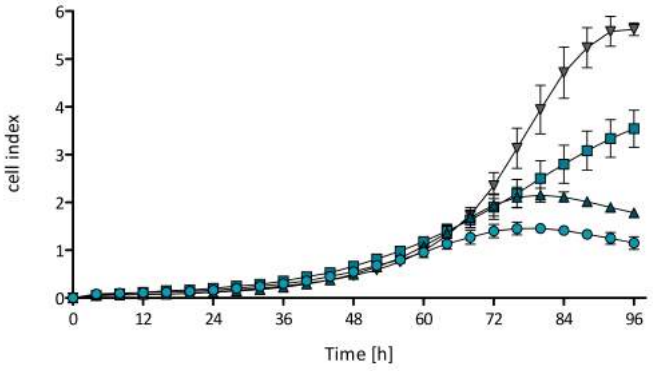

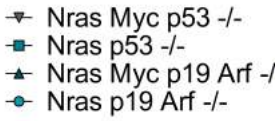

(c) 1000 cells per well

Figure 25: Proliferation of mHCC cell lines traced with xCELLigence RTCA. Different cell counts (7500, 2500, 1000) of mHCC cell lines Nras p19 Arf -/-, Nras p53 -/-, Nras Myc p19 Arf -/-, Nras Myc p53 -/- seeded in at least 3 wells of a 96 well E-plate and incubated for 96 h. Graphs show data points obtained every 4 h. Increase in the cell index (CI) corresponds to cell growth and proliferation.

increase in CI exceeding that of mock infected cells was observed in the group infected with MOI 0.1. The CI remained higher than mock until 96 hpi. Only the higher concentration of MOI 1 caused a clear decrease in CI, as early as 56 hpi. The CI dropped to 0.36 at 72 hpi and persisted low until 96 hpi. With the moderately susceptible cell line Nras p53 -/- (subfigure 26b) no oncolytic activity was seen at 48 hpi. Starting at about 60 hpi at MOI 1 there was a clear decline in cell index indicating oncolysis. By 96 hpi the mean CI of the mock infected cells had grown continuously to 3.5. At this point the groups MOI 0.1 and 1 showed a clear dose dependent oncolytic response with CI of 2.4 and 0.7, respectively. In the susceptible cell line Nras Myc p19 Arf -/- (subfigure 26c) an early dose dependent response was detectable starting at 48 hpi. There was a considerable decrease in CI relative to mock in groups MOI 0.1 and 1 at all three time points. At 96 hpi the following CI were reached: 1.6 (mock), 0.3 (MOI 0.1) and 0.02 (MOI 1). The moderately susceptible cell line Nras Myc p53 -/- (subfigure and 26d) showed first moderate changes in CI around 48 hpi. At 72 hpi CI of group MOI 0.1 remained similar to that of the mock. The only reduction relative to mock (3.2) was registered in group MOI 1, with a strong decrease to 1.2. At 96 hpi a considerable and dose dependent reduction in CI was measured in both infected groups with mean CI of 3.9 (mock), 1.9 (MOI 0.1) and 0.4 (MOI 1).

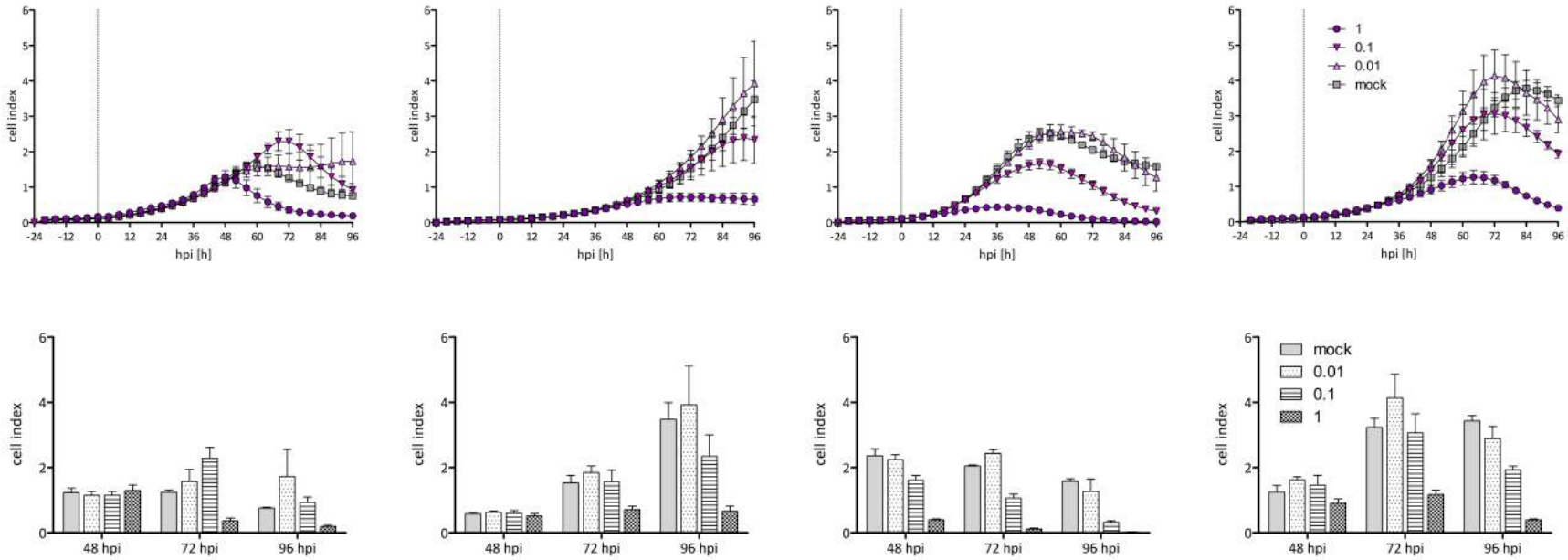

(a) Nras p19 Arf -/- **(b)** Nras p53 -/- **(c)** Nras Myc p19 Arf -/- **(d)** Nras Myc p53 -/-

Figure 26: Dynamic oncolytic effects of GLV-0b347 on mHCC cell lines. The viability of mHCC cell lines Nras p19 Arf -/-, Nras p53 -/-, Nras Myc p19 Arf -/- and Nras Myc p53 -/- was evaluated by continuous measurements with the xCELLigence RTCA system. 1000 cells per well were seeded in at least three wells of a 96 well E-plate and incubated 24 h for cell adhesion. Cells were infected with MOIs of 0.01, 0.1 and 1 (time point represented by vertical dotted line), with an additional mock control and a death control incubated with Triton X-100 (MOI 0,01 and Triton X-100 not shown). The impedance at the well bottoms was measured every 30 min for 120 h. Data points are displayed every 4 hours. A change in cell index (CI) represents either growth, a change in viability or in cell morphology.

3.5 GLV-0b347 Replicates Efficiently in mHCC Cell Lines

To assess whether GLV-0b347 mediated oncolysis is linked to replication efficiencies in mHCC cell lines, plaque assays were performed on CV1-indicator cells. Cell lines Nras p19 Arf -/-, Nras p53 -/-, Nras Myc p19 Arf -/- and Nras Myc p53 -/- were infected with GLV-0b347 at MOI 0.075 and viral titers were determined at time points 1, 24, 48, 72 and 96 hpi.

Viral growth curves are shown in figure 27. All mHCC cell lines supported the propagation of vaccinia virus. Viral replication showed a phase of exponential growth reaching a plateau. In Nras p53 -/- and Nras Myc p53 -/- cells titers slightly declined after 72 hpi. GLV-0b347 showed moderate differences in replication efficiency in mHCC cell lines, as shown by the viral growth curves. For all four cell lines a 10^3 to10^5-fold increase in viral titers was observed between 1 and 24 hpi. After 48 hours a plateau was reached above 10^7 PFU/mL and titers did not increase notably further.

In order to compare replication in mHCC cell lines, the maximum titer reached in each cell line, as well as the initial titer (obtained at 24 hpi) were chosen as key parameters (figure 28). The fastest increase in virus titer during the first 24 hours was observed in cell line Nras Myc p19 Arf -/- reaching a titer of 1.1 x 10^7 PFU/mL at 24 hpi followed by Nras p19 Arf -/- with 2.3 x 10^6 PFU/mL, Nras Myc p53 -/- with 5 x 10^5 PFU/mL and Nras p53 -/- with 3 x 10^5 PFU/mL, as depicted in figure 28a. The highest titer was achieved in Nras Myc p19 Arf -/- with 1.6 x 10^8 PFU/mL at 72 hpi, followed by Nras p19 Arf -/- with 1.2 x 10^8 PFU/mL at 96 hpi, Nras Myc p53 -/- with 3.9 x 10^7 PFU/mL at 72 hpi and lastly Nras p53 -/- with 3.6 x 10^7 at 72 hpi (figure 28b). While the virus reached titers beyond 10^6 PFU/mL in the first 24 hpi as well as maximum titers above 10^8 PFU/mL within 96 hpi in both susceptible cell lines, neither was reached in the moderately susceptible cell lines.

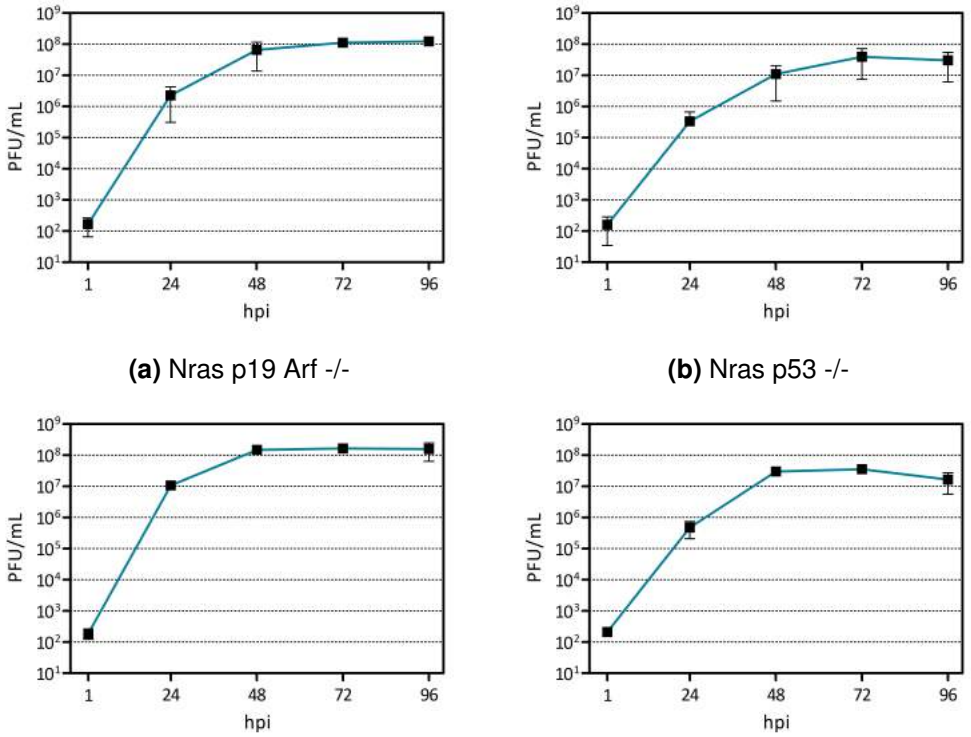

(a) Nras p19 Arf -/-

(b) Nras p53 -/-

(c) Nras Myc p19 Arf -/-

(d) Nras Myc p53 -/-

Figure 27: Replication of GLV-0b347 in mHCC cell lines. Murine HCC cell lines Nras p19 Arf -/-, Nras p53 -/-, Nras Myc p19 Arf -/- and Nras Myc p53 -/- were infected at an MOI of 0.075 and samples were taken at five different time points post infection (hpi). Plaque assays on CV-1 indicator cells were performed. Viral growth curves show mean and standard deviation of the determined plaque count (plaque forming unit [PFU] per mL) of three independent experiments.

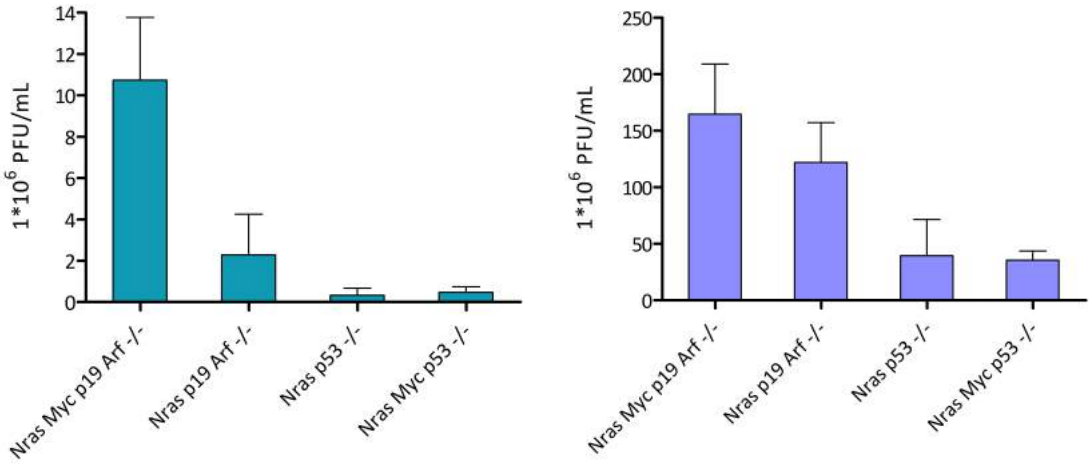

(a) Initial Increase

(b) Maximum Titer

Figure 28: Key parameters of GLV-0b347 replication in mHCC cell lines. Graphs show the initial titer increase in the first 24 hpi (a) and the maximum titers in each cell line (b) Values are presented as mean and standard deviation. Data is derived from the same three independent experiments displayed in figure 27.

3.6 Antiviral Gene Expression Varies in mHCC Cell Lines of Distinct Oncolysis Resistance Groups

In order to understand the different reactions and defense mechanisms of the mHCC cell lines, gene expression levels were compared between cell lines of different oncolysis resistance groups. Therefore, changes in mRNA levels were investigated in Nras p19 Arf -/- (susceptible) and Nras p53 -/- (moderately susceptible) using a large-scale single shot RT-qPCR-array of 84 antiviral response genes. The amount of mRNA present in cell lines pre- and post-infection with GLV-0b347 at an MOI of 0.075 was measured via RT-qPCR and analyzed with the comparative $\Delta\Delta$CT-method. Table 5 lists the measured ΔCT values of control and test-samples, as well as $\Delta\Delta$CT values and the fold-change from both cell lines for all examined genes. Some results are tagged with additional commentaries A, B or C. These additions were generated automatically by the Qiagen analyzing program and are explained in the table's annotation. A table with further information related to all genes listed can be found in the appendix (table 14). Figures 29a and 29b give an overview over the induction or suppression of the different genes in the respective mHCC cell lines. As depicted, post infection there was a strong induction of multiple genes in Nras p19 Arf -/- and only a weak induction of fewer genes in Nras p53 -/-. Figure 30 compares expression of genes between the two cell lines at baseline (subfigure 30a), as well as after infection (subfigure 30b). Several genes were expressed differently at baseline, when comparing both cell lines. The imbalance in gene expression was slightly smaller after infection.

Figure 31 compares the expression of 12 selected genes measured via RT-qPCR. These include five genes coding for pattern recognition receptors (PRR) and adaptor molecules: TLR9, MyD88, MDA5, RIG-I and AIM2 as well as seven genes encoding downstream signaling molecules and response genes: MAVS, STAT1, IRF3, IRF7, IFN-β, IL1 and IL6. The displayed fold changes show the gene induction/suppression post infection with GLV-0b347. A distinct induction of several genes was detected in Nras p19 Arf -/-. IRF7 and IFN-βwere induced more than 10-fold, while MYD88 and IL6 showed inductions greater than 3-fold. The AIM2 gene was found to be suppressed. In contrast there was almost no distinct induction in Nras p53 -/-, except IL6 which increased almost 18-fold.

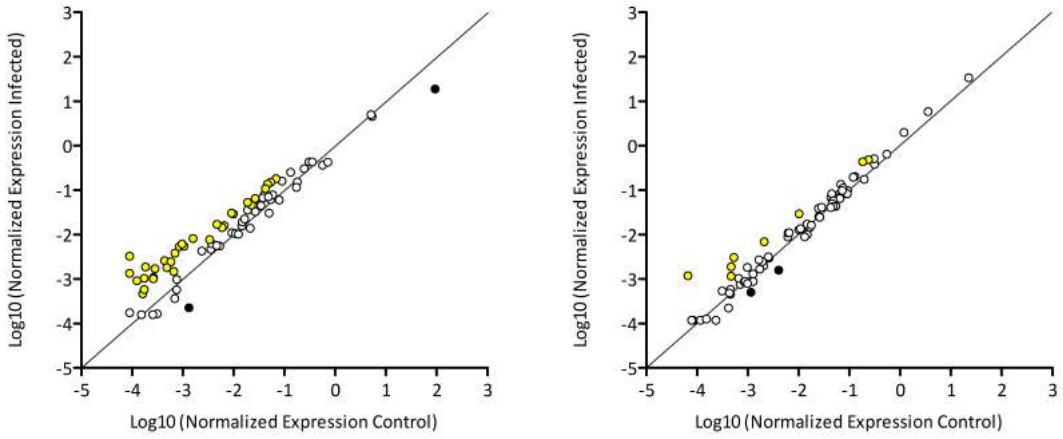

(a) Nras p19 Arf -/- **(b)** Nras p53 -/-

Figure 29: Gene induction in Nras p19 Arf -/- and Nras p53 -/- post infection with GLV-0b347. The figures show the normalized gene expression (in Log10) of the experimental group (y-axis) versus the control group (x-axis). Yellow dots represent genes where the experimental group is relatively up-regulated (fold regulation [FR] greater than 2), white dots represent genes which are unchanged (FR between 2 and -2) and black dots represent genes which are down-regulated (FR lower than -2).

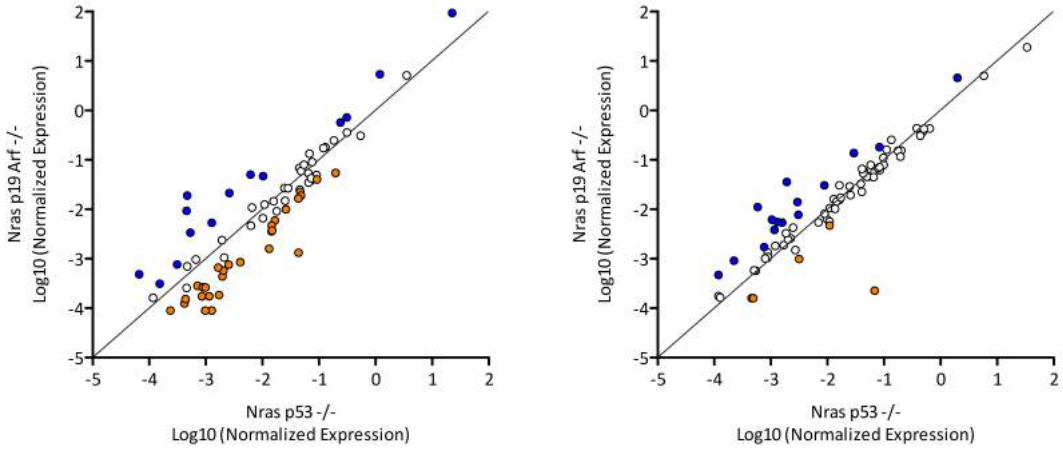

(a) Baseline **(b)** 24 hpi

Figure 30: Gene expression of Nras p19 Arf -/- and Nras p53 -/- at baseline and 24 hpi. The two subfigures show the normalized gene expression (in Log10) of Nras p19 Arf -/- (y-axis) versus Nras p53 -/- (x-axis). Subfigure (a) shows the expression levels of both cell lines prior to infection, and subfigure (b) 24 h after infection. Blue dots indicate genes which are expressed at least twice as much in Nras p19 Arf -/- than in Nras p53 -/-, while orange dots indicate vice versa.

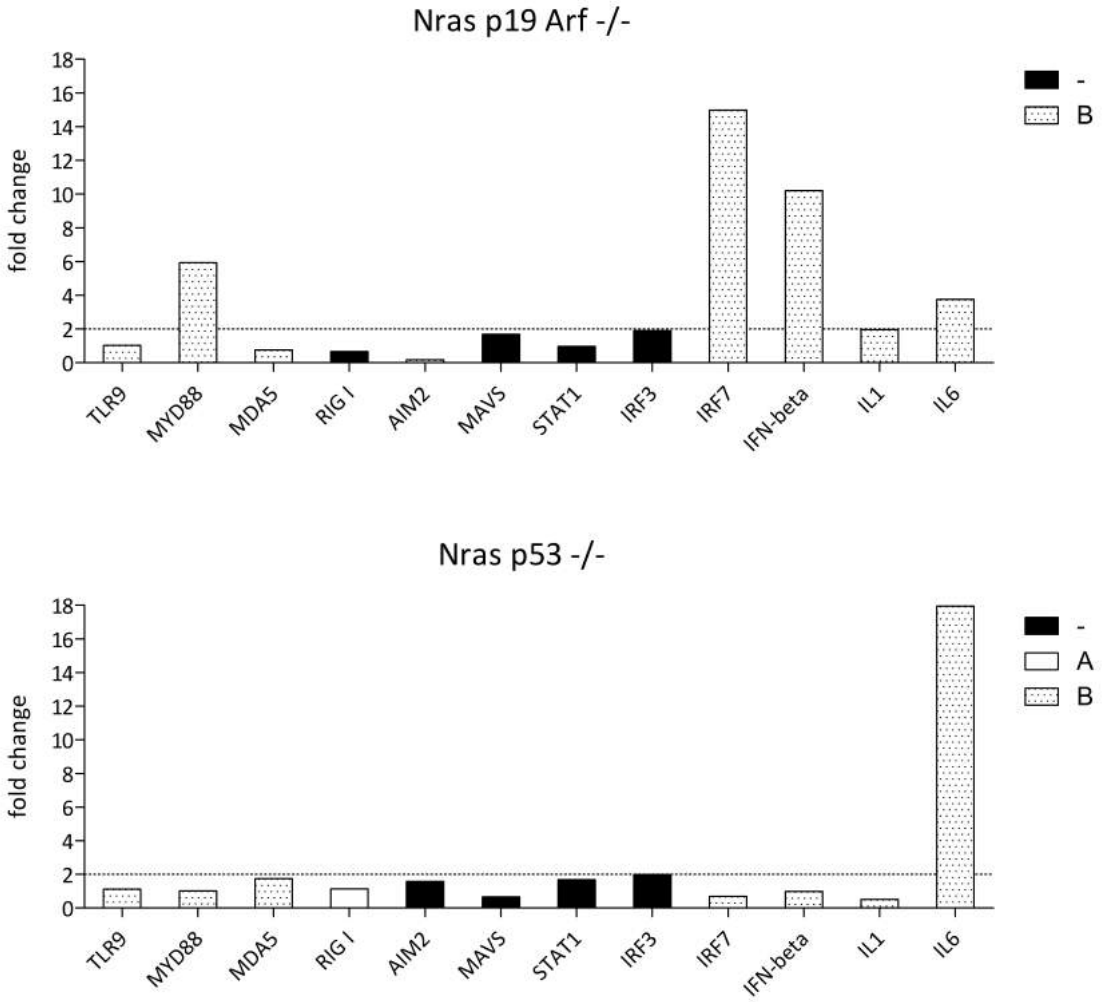

Figure 31: Induction of 12 antiviral genes in Nras p19 Arf -/- and Nras p53 -/- 24 hpi with GLV-0b347 at an MOI of 0.075. Results are displayed as fold change (fc). A fold change higher than 2, as indicated by the dotted lines, is considered a relevant induction in gene expression. Columns are coded according to the comments of Qiagen-analysis (as described in table 5). – (black): No comment, A (white): One of the groups (either control or test group) threshold cycle was > 30, B (dotted): threshold cycles of both groups were > 30. The data shown is from one experiment.

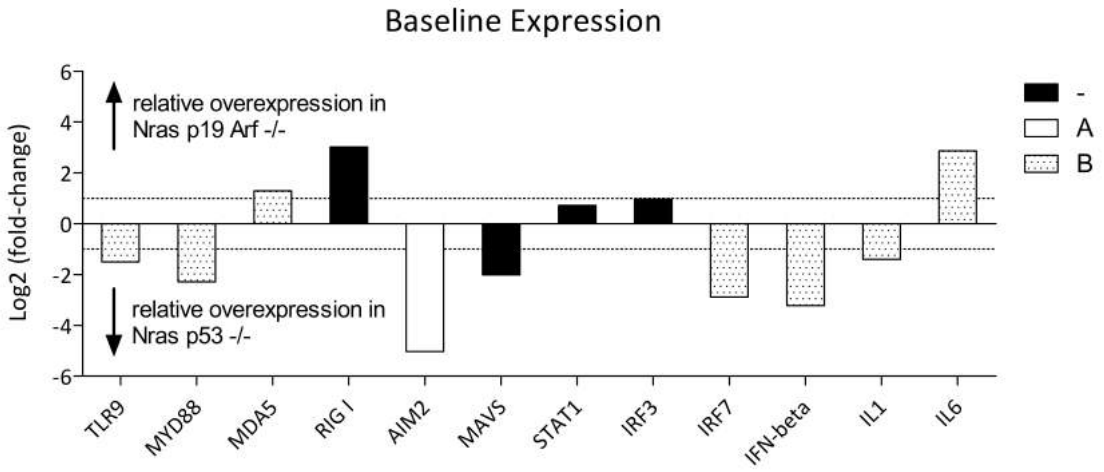

Figure 32: Relative comparison of gene expression between Nras p19 Arf -/- and Nras p53 -/- at baseline (control group). A fold-change was calculated using both control groups: Fold-change = 2^(ΔΔCT = ΔCT[control Nras p19 Arf -/-] - ΔCT[control Nras p53 -/-]). The logarithm of this fold-change to base 2 is plotted on the y-axis. A positive value represents a relative overexpression in Nras p19 Arf -/-, while a negative value represents an overexpression in Nras p53 -/-. Dotted lines indicate a Log(fold-change) of 1/-1 which represents a double in gene expression relative to the other cell line. Legend - (black): No comment. A (white): One of the groups (either control or test group) threshold cycle was $>$ 30. B (dotted): threshold cycles of both groups were $>$ 30. The data shown is from one experiment.

As depicted in figure 30a, at baseline there were 14 genes relatively higher expressed in Nras p19 Arf -/- (blue dots) and 28 genes higher expressed in Nras p53 -/- (orange dots). Figure 32 shows the compared relative baseline expression of the 12 representative genes highly relevant to cellular antiviral defense. Cell line Nras p19 Arf -/- showed overexpression of RNA-sensing molecules MDA5 and RIG-I, as well as of the cytokine IL6. Differences in gene expression of STAT1 and IRF3 were less than twofold. Nras p53 -/- exhibited a higher expression of TLR9 and TLR-adapter molecule Myd88, as well as intermediate signaling molecules MAVS and IRF7. Furthermore, Nras p53 -/- expressed higher amounts of IFN-β and IL1. Most prominently, Nras p53 -/- had a 32-fold higher expression of the DNA-sensing molecule AIM2 than Nras p19 Arf -/-.

Table 5: Expression of Antiviral Response Genes in Nras p19 Arf -/- and Nras p53 -/-.

	Nras p19 Arf -/-					Nras p53 -/-				
Genes	ΔCTc	ΔCTt	ΔΔCT	FC	*	ΔCTc	ΔCTt	ΔΔCT	FC	*
Aim2	9.565	12.109	2.544	0.172	B	4.533	3.875	-0.657	1.577	
Atg12	0.815	1.454	0.639	0.642		2.063	1.062	-1.001	2.002	
Atg5	4.222	4.022	-0.2	1.148		3.947	3.579	-0.368	1.291	
Azi2	3.865	2.477	-1.387	2.616		4.474	3.593	-0.881	1.842	
Card9	11.791	9.193	-2.598	6.053	B	10.462	10.358	-0.104	1.075	B
Casp1	10.492	11.432	0.94	0.521	B					C
Casp8	2.477	2.71	0.232	0.851		2.953	2.316	-0.637	1.555	
Ccl3	11.159	8.6	-2.559	5.894	B	8.992	8.816	-0.176	1.13	B
Ccl4	10.195	7.549	-2.646	6.259	A	7.951	9.299	1.348	0.393	A
Ccl5	7.56	7.499	-0.06	1.043		9.629	9.589	-0.04	1.028	B
Cd40					C					C
Cd80	12.594	11.066	-1.528	2.884	B	13.074	13.045	-0.029	1.021	B
Cd86					C	13.65	13.045	-0.605	1.521	B
Chuk	2.022	1.709	-0.313	1.242		2.447	1.193	-1.254	2.386	
Cnpy3	6.11	6.011	-0.098	1.07		5.997	5.94	-0.056	1.04	
Ctsb	4.209	2.721	-1.487	2.804		2.352	2.513	0.161	0.895	
Ctsl	-2.412	-2.178	0.233	0.851		-0.254	-0.993	-0.739	1.669	
Ctss					C	13.553	13.045	-0.509	1.423	B
Cxcl10	8.22	7.017	-1.203	2.303		10.88	8.352	-2.529	5.77	B
Cxcl11					C	13.64	13.045	-0.596	1.511	B
Cxcl9					C					C
Cyld	5.477	4.448	-1.028	2.04		4.429	4.207	-0.223	1.167	
Tkfc	8.139	7.742	-0.397	1.317	A	6.111	6.516	0.405	0.755	
Ddx3x	1.703	1.224	-0.479	1.394		0.878	0.638	-0.24	1.181	
Ddx58	5.565	6.165	0.6	0.66		8.586	8.401	-0.185	1.137	A
Dhx58	10.484	8.03	-2.453	5.477	B	11.059	9.754	-1.306	2.472	B
Fadd	6.078	5.695	-0.384	1.305		5.32	5.294	-0.026	1.018	
Fos	9.888	7.524	-2.365	5.15	A	8.893	7.176	-1.717	3.287	A
Hsp90	-2.348	-2.319	0.029	0.98		-1.824	-2.544	-0.72	1.647	
Ifih1	10.363	10.772	0.409	0.753	B	11.657	10.86	-0.798	1.738	B
Ifna2	10.758	8.681	-2.077	4.218	B	8.934	8.965	0.03	0.979	B
Ifnar1	7.254	5.973	-1.282	2.431		6.621	6.274	-0.347	1.272	
Ifnb1	12.411	9.059	-3.352	10.208	B	9.19	9.223	0.033	0.977	B
Ikbkb	7.407	6.124	-1.283	2.434		5.915	6.102	0.188	0.878	
Il12a					C					C
Il12b	12.974	10.098	-2.876	7.342	B	11.224	12.131	0.907	0.533	B
Il15	10.369	9.989	-0.381	1.302	B	8.626	8.305	-0.321	1.249	A
Il18	4.32	5.036	0.716	0.609		7.342	6.828	-0.514	1.428	
Il1b	13.452	12.487	-0.965	1.952	B	12.052	13.045	0.992	0.503	B
Il6	11.014	9.106	-1.908	3.754	B	13.879	9.713	-4.166	17.946	B

Table 5: Expression of Antiviral Response Genes - Continued

	Nras p19 Arf -/-					Nras p53 -/-				
Genes	ΔCTc	ΔCTt	ΔΔCT	FC	*	ΔCTc	ΔCTt	ΔΔCT	FC	*
Irak1	4.639	3.678	-0.961	1.947		3.443	3.35	-0.093	1.066	
Irf3	2.917	1.989	-0.927	1.902		3.883	2.888	-0.995	1.994	
Irf5	10.014	7.35	-2.664	6.338	A	10.563	9.908	-0.655	1.575	B
Irf7	13.452	9.548	-3.904	14.974	B	9.623	10.147	0.523	0.696	B
Isg15	6.753	6.503	-0.249	1.189		11.095	10.739	-0.356	1.28	B
Jun	4.414	2.879	-1.535	2.898		6.612	5.095	-1.517	2.861	
Map2k1	4.727	3.901	-0.826	1.773		3.808	3.679	-0.129	1.094	
Map2k3	4.853	4.484	-0.369	1.292		3.938	3.942	0.004	0.997	
Map3k1	7.737	5.874	-1.863	3.637		6.098	5.855	-0.243	1.184	
Map3k7	4.089	3.672	-0.416	1.335		4.38	4.109	-0.271	1.207	
Mapk1	1.49	1.209	-0.28	1.215		1.679	1.396	-0.283	1.217	
Mapk14	5.341	4.462	-0.879	1.84		4.453	4.331	-0.122	1.088	
Mapk3	3.656	4.069	0.413	0.751		4.208	4.52	0.312	0.805	
Mapk8	3.479	2.641	-0.838	1.788		3.731	3.169	-0.562	1.476	
Mavs	8.08	7.328	-0.751	1.683		6.073	6.651	0.578	0.67	
Mefv	7.751	7.469	-0.282	1.216		7.325	6.52	-0.805	1.747	
Mx1					C					C
Myd88	12.488	9.918	-2.57	5.938	B	10.201	10.173	-0.028	1.02	B
Nfkb1	4.356	3.822	-0.534	1.448		3.464	3.591	0.127	0.916	
Nfkbia	4.554	3.203	-1.351	2.55		3.789	3.357	-0.432	1.35	
Nlrp3	11.657	12.577	0.92	0.529	B	12.675	12.951	0.275	0.826	B
Nod2	11.887	9.851	-2.036	4.102	B	10.15	10.142	-0.008	1.006	B
Oas2										
Pin1	5.73	4.236	-1.494	2.816		4.38	4.543	0.164	0.893	
Pstpip1	8.718	7.879	-0.839	1.789	B	9.017	8.662	-0.355	1.279	B
Pycard	12.493	10.749	-1.744	3.35	B	9.771	10.955	1.184	0.44	B
Rela	9.297	6.947	-2.35	5.097	A	6.247	6.812	0.565	0.676	
Ripk1	5.921	5.475	-0.446	1.362		4.542	4.629	0.088	0.941	
Spp1	-6.543	-4.23	2.313	0.201		-4.49	-5.073	-0.583	1.498	
Stat1	6.531	6.572	0.041	0.972		7.257	6.51	-0.747	1.678	
Sugt1	0.483	1.239	0.756	0.592		1.699	0.979	-0.72	1.647	
Tank	5.219	4.935	-0.284	1.217		5.349	4.685	-0.664	1.585	
Tbk1	5.236	3.946	-1.29	2.445		5.14	4.615	-0.525	1.439	
Tbkbp1	5.73	4.813	-0.916	1.887		11.059	9.038	-2.021	4.059	B
Ticam1	10.574	9.391	-1.183	2.27	B	9.244	8.533	-0.711	1.637	B
Tlr3	6.328	6.617	0.289	0.818		6.518	6.202	-0.316	1.245	
Tlr7	13.452	8.263	-5.189	36.476	B	10.002	9.087	-0.915	1.885	B
Tlr8	11.93	12.627	0.697	0.617	B	11.102	11.107	0.004	0.997	B
Tlr9	12.672	12.627	-0.044	1.031	B	11.166	11.008	-0.158	1.116	B
Tnf					C					C

Table 5: Expression of Antiviral Response Genes - Continued

	Nras p19 Arf -/-					Nras p53 -/-				
Genes	ΔCTc	ΔCTt	ΔΔCT	FC	*	ΔCTc	ΔCTt	ΔΔCT	FC	*
Tradd	2.535	3.117	0.582	0.668		3.065	2.355	-0.71	1.636	
Traf3	6.651	5.11	-1.541	2.91		5.268	5.34	0.073	0.951	
Traf6	6.79	5.044	-1.746	3.354		5.809	5.944	0.135	0.911	
Trim25	11.907	9.95	-1.957	3.883	B	9.993	10.304	0.311	0.806	B

FC: fold-change. ΔCT: CT(gene of interest) - average CT(housekeeping genes). ΔΔCT: ΔCT(control [c]) - ΔCT(test [t]). Alternative names of genes as shown in figures 31 and 32: Ddx58 (RIG-I), Dhx58 (LGP2), Ifih1 (MDA5).

The comments (*) are described as in the "RT^2 Profiler PCR Array Gene Expression Analysis Report" provided by Qiagen:

A: *"This gene's average threshold cycle is relatively high (> 30) in either the control or the test sample and is reasonably low in the other sample (< 30). These data mean that the gene's expression is relatively low in one sample and reasonably detected in the other sample suggesting that the actual fold-change value is at least as large as the calculated and reported fold-change result. [...] it is important to have a sufficient number of biological replicates to validate the result for this gene."*

B: *"This gene's average threshold cycle is relatively high (> 30), meaning that its relative expression level is low, in both control and test samples, [...] This fold-change result may also have greater variations; therefore, it is important to have a sufficient number of biological replicates to validate the result for this gene."*

C: *"This gene's [...] expression was undetected, making this fold-change result erroneous and uninterpretable."*

Table 6: House Keeping Genes and PCR-Controls.

	Nras p19 Arf -/-			Nras p53 -/-		
Genes	CTc	CTv	*	CTc	CTv	*
Actb	20.85	21.55		18.89	20.01	
B2m	20.17	21.34		21.67	22.2	
Gapdh	20.48	21.38		19.07	20.03	
Gusb	25.26	26.12		26	26.55	
Hsp90ab1	20.99	21.47		19.99	20.99	
MGDC	35	35	C	33.63	34.03	B
RTC	19.48	20.02		19.54	19.95	
RTC	19.49	19.9		19.51	35	A
RTC	19.4	19.76		19.53	19.78	
PPC	18.43	18.43		18.48	18.43	
PPC	18.41	18.39		18.4	18.36	
PPC	18.6	18.65		18.64	18.54	
Average Controls						
Avg. RTC	19.46	19.89		19.53	24.91 *(19.87)*	
Avg. PPC	18.48	18.49		18.51	18.44	
PCC	0.98	1.4		1.02	6.47 *(1.42)*	

RTC: Reverse transcription control. PPC: Positive transcription control. MGDC: Mouse genomic DNA contamination. Out of three RTCs in the Nras p53 -/- test sample one value is aberrant (CT = 35, i.e. not detected, vs. 19.95 and 19.78), making this measurement a possible outlier. The therefore corrected values are printed in italic. The interpretation of PCR-controls is described in chapter 2.9.3.

4 Discussion

The main objective of this thesis was the investigation of the effects of a recombinant vaccinia virus (GLV-0b347) on murine hepatocellular carcinoma (mHCC) cell lines. HCC is known to have a heterogeneous mutational profile, therefor differences in oncogenic mutations may contribute to determining the susceptibility of individual tumors to viral infection. Six distinct mHCC cell lines with well-defined oncogenic mutations were investigated with respect to this question. Tumors lose many of their antiviral defense mechanisms through their malignant transformation, and thus become susceptible to viral infections. The extent to which innate immune defense remains functional may also contribute to primary OV resistance. The experimental approach of this thesis was inspired by the paper of Berchtold et al. in 2013 which revealed that resistance of sarcoma cell lines to measles vaccine (MeV-SCD) mediated oncolysis is determined by the innate immune defense [107].

4.1 Phase Contrast and Fluorescence Photos Confirm Successful Infection of mHCC Cell Lines with GLV-0b347

Photos revealed that GLV-0b347 infects mHCC cell lines in a dose and time dependent manner. Low minimal infective doses were necessary to demonstrate successful infection of the cell layer. An MOI of as low as 0.001 was sufficient to observe successful infection in all cell lines except for Nras p53 -/- in which an MOI of 0.01 was necessary. Higher initial infective doses resulted in earlier infection and greater cell damage. These observations match previous studies showing an efficient dose-dependent infection of human HCC cell lines by recombinant

VACV GLV-1h68 and GLV-2b372, via the expression of GFP and turboFP635, respectively [108, 109]. The damage in the cell layer further increased over time. In cell lines susceptible to VACV, e.g. Nras p19 Arf -/- and Nras Myc p19 Arf -/-, there was a decrease in the fluorescence signal with higher MOIs or at later time points. This indicates effective and early lysis of mHCC cells, leaving less time to synthesize fluorescent proteins. A decline in fluorescence signal through effective tumor cell reduction has been described by Tsoneva et al. during the infection of A549-tumor-bearing humanized NSG mice with GLV-2b372 [110].

4.2 Varying Cytotoxicity in mHCC Cell Lines Implies Link to Mutational Background

The results of cell mass quantification via the SRB assay revealed a highly variable outcome of mHCC viability after VACV infection. Based on the remaining cell mass after 96 h at MOI 1, cell lines were grouped according to viability. While the susceptible cell lines Nras p19 Arf -/- and Nras Myc p19 Arf -/- showed clear dose and time dependent reductions of cell mass ($<$ 50% remaining cell mass), cell lines Nras Myc p53 -/- and Nras p53 -/- responded moderately (50-75%) and cell lines Akt Myc p19 Arf -/- and Akt Myc p53 -/- revealed extensive resistance ($>$ 75%) to even the highest viral dose of 1 viral particle per cell (MOI 1).

Both resistant cell lines carry protein kinase B (PKB/Akt) activating mutations. Akt is commonly known as an oncogene that is strongly involved in cell survival [111]. Activated Akt exerts antiapoptotic properties through phosphorylation of Bad and suppression of p53 via mdm2. Akt can also activate NFκ B and thus promote cell survival. If Akt is conferring resistance to oncolysis it could imply that a part of GLV-0b347s oncolytic ability is dependent on the induction of apoptosis. In sarcoma cell lines it was shown that VACV GLV-1h68 downregulates the expression of the anti-apoptotic MCL-1 protein and thereby induces apoptosis [112]. Further investigation into GLV-0b347-induced apoptosis is needed, as the relevance of OV-induced apoptosis in effective tumor reduction has been demonstrated in numerous settings [113, 114]. Within the moderately susceptible group both cell lines were p53 negative, while within the susceptible group both cell lines were p19 Arf negative. A p53 mutation has already been described as a bad prognostic

factor in HCC [9]. In this study, the p53 negative mHCC cell lines showed poorer response to GLV-0b347-mediated oncolysis in the SRB-assay. One problem with this direct comparison is that the p53-negative cells are not matched with otherwise identical p53-positive cells, but instead these have a p19 Arf knockout. Both susceptible cell lines shared an intact p53 expression and a p19 Arf knockout. P19 Arf (p14 Arf in humans) is a nuclear protein and tumor suppressor that is transcriptionally induced through Myc and Ras overexpression. It can induce cell cycle arrest and apoptosis via p53, as well as p53-independent [115]. This further suggests the involvement of apoptotic pathways in OV-resilience.

An important factor for VACV replication efficiency and virulence is its ability to activate host mitogen activated protein kinases (MAPK). Therefore, vaccinia virus expresses the vaccinia growth factor (VGF), a glycosylated polypeptide with homology to the epidermal growth factor (EGF) and the transforming growth factor (TGF) [116]. VGF binds the EGF-receptor thereby activating downstream MAPK pathways which ultimately facilitate VACV propagation [117]. Conversely, VGF-deficient VACV is attenuated in non-dividing cells [118]. For these reasons, hypothetically, constitutionally activated Nras, or other components of the MAPK pathway could cause susceptibility to VACV infection and subsequent oncolysis in cancer cells. The lack of activating Nras mutations in both resistant cell lines Akt Myc p19 Arf -/- and Akt Myc p53 -/- is indicative of this relation. There remain many ways the respective mutations could confer susceptibility or resistance to VACV mediated oncolysis. Further specific experiments will have to be conducted to substantiate these hypotheses.

4.3 Real Time Cell Analysis

The xCELLigence system was used to compare dynamic viability in four different cell lines after infection with GLV-0b347, Nras p19 Arf -/-, Nras p53 -/-, Nras Myc p19 Arf -/- and Nras Myc p53 -/-. The xCELLigence RTCA assay has been established as a reliable cytotoxicity assay in various settings, including oncolytic virotherapy. Dyer et al. employed the xCELLigence RTCA system to compare potency and time course of oncolysis among different oncolytic adenoviruses [119]. Fajardo et al. used the xCELLigence system to compare T-cell enhanced adenoviral oncolysis between two cell lines [120]. These publications support the

feasibility of xCELLigence as a viability assay in the context of oncolytic virotherapy.

4.3.1 xCELLigence RTCA Assays Show Rapid Proliferation

The overall proliferation rate of all six cell lines was high, although the FBS concentration in culture medium was restricted to only 5%. Proliferation of cell lines Nras p19 Arf -/-, Nras p53 -/-, Nras Myc p19 Arf -/- and Nras Myc p53 -/- was further examined using the xCELLigence RTCA system. For all four cell lines it was observed that, (i) the fewer cells were initially seeded, the later the highest CI value appeared in time and (ii) the highest CI value of a cell line stayed near the same, independent of the initial cell count. Both observations are explainable by assuming that the highest CI value represents the point in time at which the cells have depleted the medium. In non-malignant cells the highest CI would represent the time at which cells reach confluence and form a monolayer at the bottom of the well. Since malignant cells are not contact inhibited, they continue to proliferate and form multilayers until no more nutrients are left. This results in substantially longer time to reach maximum CI with lower initial cell counts. Accordingly, as seen in all cell lines, the proliferation phase is not followed by a plateau as expected by sustained cell confluence. After a steady increase in CI to a peak, a substantial decline of CI was observed due to cell death after depletion of the medium. Only a run with 1000 cells per well provided a long and uniform exponential growth phase necessary for long-run measurements of 120 h. Therefore, in the subsequent experiments, 1000 cells per well were seeded and infected 24 h later. The drawback of this low cell count was that the very slow initial increase in CI made it sometimes impossible to detect any effect of oncolysis at an early stage of the experiment.

Interestingly, the more resilient cell lines reached higher maximum CI. The moderately susceptible cell lines Nras p53 -/- and Nras Myc p53 -/- reached CI values around 5, while the second most susceptible cell line Nras Myc p19 Arf -/- reached 3 and the most susceptible cell line Nras p19 Arf -/- reached no more than 2. This could be (i) a coincidental discovery, (ii) the effect of an unknown cell line feature that causes higher OV resistance and higher measured CI (as a confounding factor), or (iii) related to cellular attachment strength. Cells that exert

higher attachment strength cause a higher CI. After VACV infection they would also show more remaining cell mass in the SRB-assay, where still viable cells with low attachment strength can be removed through the process of washing with PBS. Further investigating this observation could be valuable. If the second assumption is correct, this would lead to a prognostic factor of OV resistance that could be easily tested through the xCELLigence assay.

4.3.2 Exceptions and Limitations of CI Validity

Data obtained by xCELLigence RTCA assays corroborate the findings of prior SRB assay-based cell viability testing showing similar effectiveness of GLV-0b347 in tumor cell reduction. For Nras p19 Arf -/- cells, however, instead of the expected reduction, an increase in CI was detected. CI, which represents measured impedance at the bottom of the well, is influenced by cell number, cell size/morphology and cell attachment strength. It is most likely that not an increase in cell viability (i.e. cell number or attachment strength), but a change in morphology caused by tumor cell infection is responsible for this CI increase. Langenbach stated that an increase in CI after infection is consistent with morphological changes like cell fusion and enlargement [121]. In such instances the validity of CI measurements must be questioned.

4.4 GLV-0b347 Replication in the Light of mHCC Cell Lines Resistance Group

Higher oncolytic effectiveness is necessarily linked to higher infection rate and spread of the virus in tumor tissues. As was demonstrated by phase contrast and fluorescence photos, GLV-0b347 can infect all six mHCC cell lines. The susceptible and moderately susceptible cell lines were further investigated to quantify the extent of viral replication and to compare viral replication with oncolytic effectiveness. This is of special interest since studies from Chen et al. with vaccinia based OVs have shown that in vitro replication efficacy can prognosticate in vitro and in vivo virulence and anti-tumor efficacy [122].

Plaque assays revealed that viral replication is linked to the susceptibility of the cell lines and differs between susceptibility groups. In sensitive cell lines Nras p19 Arf -/- and Nras Myc p19 Arf -/- the mean viral titer reached over 2 x 10^6 PFU/mL in the first 24 h, while titers in the moderately susceptible group remained far beneath 1 x 10^6 PFU/mL in the first 24 h. Differences became more evident when comparing the mean maximum titers. Sensitive cell lines reached titers above 1 x 10^8 PFU/mL, while in the moderately susceptible group the mean was below 5 x 10^7 PFU/mL. While replication efficiency was useful in distinguishing between susceptibility groups, it was not an analog for oncolytic effectiveness. Cell line Nras Myc p19 Arf -/- was more resistant to GLV-0b347 than Nras p19 Arf -/-. None the less, GLV-0b347 replicated more efficiently in Nras Myc p19 Arf -/-, achieving higher titers in the first 24 h and higher maximum titers within 96 h. The poorer replication performance of GLV-0b347 in Nras p19 Arf -/- could be due to more effective killing of this cell line, leaving cells less time to produce viral progeny. This effect is analogous to the reduced production of fluorescent protein with higher MOIs, discussed in chapter 4.1.

One drawback with the performed assay is that in basically all cell lines viral replication reached its plateau after 48 h. This means that the initial very low infective dose of 0.075 particles per cell could have been chosen even lower. An experiment with a lower starting dose could have revealed more subtle differences between cell lines. Furthermore, we only tested four of the six cell lines, omitting those in the resistant group.

4.5 Differences in Baseline and GLV-0b347-Induced Gene Expression

To investigate the molecular basis of resistance and susceptibility the induction of antiviral genes was examined in Nras p19 Arf -/- and in Nras p53 -/- cells after infection with GLV-0b347. Whereas in the susceptible cell line Nras p19 Arf -/- 32 genes were induced, in the more resilient cell line Nras p53 -/- there were only 8. This seems counterintuitive since a resilient cell might be expected to react with a stronger induction of antiviral genes than a susceptible one. The state of resistance, however, does not solely depend on the relative induction of antiviral

genes in response to an infection, but also on the baseline expression levels prior to infection. Concerning baseline levels, 28 antiviral genes were expressed more strongly in the resistant cell line Nras p53 -/-, whereas 14 antiviral genes displayed higher basal expression levels in susceptible Nras p19 Arf -/- cells.

In order to compare more specifically, 12 antiviral genes were chosen for closer review. In Nras p19 Arf -/-, the cytokine IL1 was slightly increased but below the 2-fold threshold, IL6 was increased 4-fold and TNF was not detected at all. A considerable induction of IFN-β (10-fold) was detected being indicative of an intact viral recognition system. But, there was lacking evidence of subsequent induction of ISGs. Effectors like Mx1 were detected neither in the control nor after infection. A weak induction of ISGs concurrently with IFN-β production may suggest a dysfunction in the JAK-STAT-pathway, which usually mediates IFN effects and activates transcription of ISGs. In Nras p53 -/- only one out of the 12 selected genes, IL6, was induced in a relevant manner. IL6 is a proinflammatory cytokine known for its role in the development of HCC and as an activator of the JACK/STAT3-pathway [123]. It is also secreted in response to the detection/ sensing of pathogens. This could mean that in this cell line either most genes are not induced through viral infection, or the utilized viral dose was too low to trigger an adequate IFN response. Like in Nras p19 Arf -/-, an induction of ISGs was not detectable in Nras p53 -/-.

When comparing the expression profiles of both cell lines prior to infection, only three genes were higher expressed in the susceptible cell line Nras p19 Arf -/-: MDA5, RIG-I and IL6. While Myskiw et al. stated that MDA5 and RIG-I (cytoplasmatic dsRNA sensors) can both detect RNA species produced during vaccinia virus infection and subsequently induce IFN production, Delaloye et al. reported that mainly MDA5 is capable to detect VACV and to induce type I IFN [124, 125]. Either way, the high baseline expression of these sensors is compatible with the induction of IFN-β after infection.

In contrast, Nras p53 -/- displayed higher expression levels of TLR9, MYD88, AIM2, MAVS, IRF7, IFN-β and IL1. TLR9 can detect foreign CpG-DNA and trigger subsequent type I IFN production. Mice deficient of TLR9 have been shown to be particularly susceptible to ectromelia virus (mousepox) [126]. MYD88 is an adaptor molecule for TLRs and supports the function of TLR9. Upon binding of TLR-specific PAMPs MYD88 mediates downstream signaling from the TLR.

This might give Nras p53 -/- an advantage in recognizing and responding to vaccinia virus, although some evidence suggests that TLR-independent pathways are more relevant for VACV induced type I IFN response [127, 128].

AIM2 is a cytoplasmatic DNA detector and was 32-fold higher expressed in Nras p53 -/- cells. This is one of the most prominent distinctions in the detected gene expression patterns and may explain the varying preparedness of mHCC cells to vaccinia infection. Hornung et al. identified AIM2 as a cytosolic dsDNA sensor that forms an inflammasome with ASC leading to activation of NFκB and caspase-1. Activation of caspase-1 and release of IL1-β in vaccinia infected B6-MCL macrophage cells was found to be dependent on AIM2 expression. Unexpectedly, an AIM2-shRNA knockout in macrophages resulted in decreased vaccinia related cell death [81].

Higher expression levels of MAVS, an intermediate signaling molecule, and IRF7 a transcription factor which mediates the production of type I interferon, are further indicators of increased preparedness to viral infection. However, no induction of IFN-β was detected in Nras p53 -/- post infection. Lastly, the higher baseline expression of IFN-β in Nras p53 -/- relative to Nras p19 Arf -/- cells might be the decisive advantage resulting in OV resistance. As summarized by Ebrahimi et al., IFN induced antiviral responses in tumor cells cause OV resistance. Studies investigating the effects of drugs disrupting IFN-signaling in combination with OVs have shown to increase viral replication and oncolysis [129]. Ruf et al. showed in vitro that a combination treatment of measles vaccine virus with resminostat (a histone deacetylase inhibitor that can suppress ISG-transcription) increases oncolytic effectiveness in human hepatoma cell lines [130]. Conversely, Berchtold et al. showed that pretreatment of tumor cells with IFN-β increases their resistance to viral infection and OV-mediated oncolysis [107].

Notable, the RT-qPCR panel experiment has several weaknesses that must be pointed out. First, a single shot large scale RT-qPCR was performed, meaning there was only one experiment that was not reproduced. Second, the high number of 84 observed genes reduces the significance of our findings, since there is an accumulated higher chance of statistic coincidence, also known as the look-elsewhere effect. Third, the comparability of the data between the cell lines in the infected sample group is somewhat questionable. Both cell lines were infected with an MOI of 0.075 with 24 hours of incubation before sample harvest. Both

cell lines differ concerning viral replication and cell viability, as discussed previously. Therefore, it is to assume that at the time of sample harvest more cells in Nras p19 Arf -/- were affected by the virus than in Nras p53 -/-, possibly skewing compared results. This could be one explanation of the observed imbalance in gene induction between the two cell lines. The results show a greater number of antiviral genes induced in the susceptible cell line Nras p19 Arf -/- by GLV-0b347 than in the more resilient Nras p53 -/-. This effect does not have to be considered while comparing baseline gene expressions. Lastly, only two cell lines were compared via qPCR as representatives of their viability group. Closer investigation of fewer key genes of antiviral response in all six cell lines is needed to yield more valid results.

5 Summary

After recent progress in cancer treatments through the emergence of targeted- and immuno-therapies, hepatocellular cancer (HCC) remains one of the most ill-treatable cancers to date. Late onset symptoms result in diagnosis of HCC in late, progressive, and often disseminated stages. Therefore, even in developed countries with adequate medical resources, HCC has a high mortality rate and new treatment options are urgently needed. The selection of patients for individual and tumour-specific therapies will most likely play an important role in future treatment strategies, which may soon include oncolytic viruses.

Oncolytic virotherapy is a promising new treatment option for patients with advanced and disseminated disease. Since the approval of Imlygic® (T-Vec) oncolytic virotherapy has entered clinical practice. Many vaccinia virus-based oncolytic viruses (OVs) are currently undergoing clinical trials. Other virotherapeutic agents based on a variety of viruses are also gaining ground.

The aim of this thesis was to investigate the oncolytic effectiveness of the recombinant vaccinia virus GLV-0b347 on murine cell lines of hepatocellular carcinoma (mHCC). For this purpose, six mHCC cell lines were selected that carry specific oncogenic mutations similar to those found in human HCCs. The mutations included activating mutations in proto-oncogenes Akt, Myc and Nras, as well as knockouts of the tumor suppressor genes p53 and p19 Arf. The mHCC cell lines were infected with the recombinant vaccinia virus GLV-0b347. Phase contrast and fluorescence photos of the infected cell layers revealed successful infection and patterns of viral spread in all cell lines. To determine the efficacy of GLV-0b347-mediated oncolysis, the cell mass based SRB viability assay was performed. The results showed a heterogeneous response of the different cell lines, which were then classified into three different sensitivity groups. Subsequently, the oncolytic efficacy in the four most responsive cell lines was investigated using the real-time

cell monitoring system xCELLigence RTCA. The continuous measurement confirmed the results of the cell mass based viability assay. The quantification of viral replication in the four mHCC cell lines showed differences in viral replication efficiency between cell lines of the susceptible and moderately susceptible group. The differences were most evident when comparing the maximum titers within 96 hours post infection (hpi). Finaly, the expression of a panel of antiviral response genes was analyzed by RT-qPCR to compare a susceptible to a moderately susceptible mHCC cell line. Differences in basel gene expression and gene induction in response to infection with GLV-0b347 were observed. While the susceptible cell line showed higher induction of crucial genes like IFN-β and IRF7, the moderately susceptible showed higher baseline expression of IFN-β, IRF7 and AIM2. The overall findings show that within one cancerous entity oncolytic efficacy of a virus can vary considerably. These differences are caused, among other factors, by the underlying oncogenic mutations of the tumor. Mutations of the innate immune response, especially of the interferon system, probably also play a decisive role. The complex background of oncolytic resistances requires further clarification. Future research should focus on identifying of prognostically reliable markers and developing strategies to direct the most effective oncolytic virus to each individual patient.

6 Zusammenfassung

Trotz vieler Fortschritte in der Krebstherapie in den letzten Jahren ist das Hepatozelluläre Karzinom (HCC) nach wie vor eine der am schlechtesten behandelbaren Krebsarten. Aufgrund spät auftretender Symptome gelingt die Diagnose meist erst in fortgeschrittenen und metastasierten Stadien. Auch in entwickelten Ländern mit moderner medizinischer Versorgung weist das HCC eine hohe Sterblichkeitsrate auf. Daher sind neue Behandlungsoptionen dringend erforderlich. Die Selektion von Patienten für individuelle und tumorspezifische Therapien wird höchstwahrscheinlich eine wichtige Rolle bei künftigen Behandlungsstrategien spielen, zu denen vielleicht bald auch oncolytische Viren zählen.

Die onkolytische Virotherapie ist eine vielversprechende neue Behandlungsform für Patienten mit fortgeschrittener und disseminierter Krankheit. Seit der Zulassung von Imlygic® (T-Vec) hat die onkolytische Virotherapie Einzug in die klinische Praxis gehalten. Derzeit befinden sich viele auf dem Vacciniavirus basierende onkolytische Viren (OVs) in der klinischen Erprobung. Weitere Virotherapeutika auf Basis vielfältiger Viren befinden sich ebenfalls auf dem Vormarsch.

Das Ziel dieser Arbeit war die Untersuchung der onkolytischen Effektivität des rekombinanten Vacciniavirus GLV-0b347 auf murinen Zelllinien des hepatozellulären Karzinoms (mHCC). Hierfür wurden sechs mHCC-Zelllinien ausgewählt, die spezifische onkogene Mutationen tragen, die denen bei menschlichen HCCs ähneln. Zu diesen Mutationen gehörten aktivierende Mutationen in den Genen für Akt, Myc und Nras sowie die Abschaltungen/Knockouts von p53 und p19 Arf. Die mHCC-Zelllinien wurden mit dem rekombinanten Vacciniavirus GLV-0b347 infiziert. Phasenkontrast- und Fluoreszenzbilder des infizierten Zellrasens zeigten Anzeichen einer erfolgreichen Infektion und Muster der Virusverbreitung in allen Zelllinien. Um die Wirksamkeit der GLV-0b347-vermittelten Onkolyse zu bestimmen, wurde der zellmassenbasierte SRB-Viabilitätsassay durchgeführt. Die

Ergebnisse zeigten ein heterogenes Ansprechen der unterschiedlichen Zelllinien, worauf diese in drei verschiedene Sensibilitätsgruppen eingeteilt wurden. In der Folge wurde die onkolytische Wirksamkeit in den vier am besten ansprechenden Zelllinien mit dem Echtzeit-Zell-Monitoring System xCELLigence RTCA untersucht. Die kontinuierliche Messung bestätigte die Ergebnisse des zellmassenbasierten Viabilitätsassays. Die Quantifizierung der viralen Replikation in den vier mHCC-Zelllinien zeigte Unterschiede in der Effizienz der viralen Replikation zwischen Zelllinien der suszeptiblen und mäßig suszeptiblen Gruppe. Am deutlichsten waren die Unterschiede beim Vergleich der maximalen Titer innerhalb von 96 Stunden nach Infektion (hours post infection - hpi). Schließlich wurde mittels RT-qPCR eine Reihe antiviraler Gene untersucht, um eine suszeptible mit einer mäßig suszeptiblen mHCC-Zelllinie zu vergleichen. Hierbei wurden Unterschiede in der basalen Genexpression und in der Geninduktion als Reaktion auf eine Infektion mit GLV-0b347 festgestellt. Während die suszeptible Zelllinie eine höhere postinfektiöse Induktion von Genen wie IFN-β und IRF7 aufwies, zeigte die mäßig suszeptible Zelllinie eine höhere Basalexpression von IFN-β, IRF7 und AIM2. Die Ergebnisse zeigen, dass selbst innerhalb einer Krebsentität die onkolytische Wirksamkeit eines Virus sehr unterschiedlich sein kann. Diese Unterschiede bedingen sich u.a. durch die zugrundeliegenden onkogenen Mutationen des Tumors. Wahrscheinlich spielen Mutationen der zellulären Immunantwort, insbesondere des Interferonsystems, ebenfalls eine entscheidende Rolle. Die komplexen Hintergründe onkolytischer Resistenzen bedürfen weiterer Aufklärung. Ein Hauptziel zukünftiger Forschung sollte darin bestehen, prognostisch zuverlässige Marker zu identifizieren und eine Strategie zu entwickeln, um individuellen Patienten das wirksamste onkolytische Virus zukommen zu lassen.

Appendix

A.1 Clinical Trials with Vaccinia Viruses

All trials involving GLV-1h68 and Pexa-Vec listed on *ClinicalTrials.gov* by July 14th, 2020. The following abbreviations are used; A: Active and not recruiting, C: Completed, IV: intra venous, IPe: intra peritoneal, IPl: intra pleural, N: No longer available, R: Recruiting, T: Terminated.

Table 7: Clinical trials on GLV-1h68 (synonym: GL-ONC1)

Indication	Phase	Status	Notes	NCT
Ovarian cancer	I/II	R	IPe, plus chemotherapy plus/minus bevacizumab	2759588
Peritoneal carcinomatosis	I/II	C	IPe	1443260
Solid tumors	I	T	IV	2714374
Malignant pleural effusion	I	A	IPl	1766739
Advanced cancers with no standard of care		N	Expanded access	3420430
Solid tumors	I	C	IV	0794131
Head and neck cancer	I	C	IV plus radiation therapy and cisplatin	1584284

Table 8: Clinical trials on Pexa-Vec

Indication	Phase	Status	Notes	NCT
Hepatocellular carcinoma	III	A	IT, plus sorafenib	2562755
Colorectal carcinoma	II	T	IV, neoadjuvant	1329809
Hepatocellular carcinoma	II	C	IV	1636284
Hepatocellular carcinoma	II	C	IV, plus sorafenib	1171651
Hepatocellular carcinoma	II	C	HCC failed sorafenib	1387555
Hepatocellular carcinoma	II	C	IT	0554372
Hepatocellular carcinoma	I/II	A	IT, plus nivolumab	3071094
Colorectal cancer	I/II	R	IV, plus durvalumab or tremelimumab	3206073

Table 8: Clinical trials on Pexa-Vec - Continued

Indication	Phase	Status	Notes	NCT
Malignant melanoma	I/II	C	IT	0429312
Colorectal carcinoma	I/II	C	IV, plus minus irinotecan	1394939
Breast cancer, soft tissue sarcoma	I/II	R	IV, plus cyclophosphamide	2630368
Solid tumors	I	R	IT, plus ipilimumab	2977156
Renal cell carcinoma	I	R	IV/IT, plus REGN2810	3294083
Solid tumors in pediatric patients	I	C	IV, dose escalation	1169584
Colorectal carcinoma	I	C	IV, dose escalation	1380600
Solid tumors	I	C	IV, dose escalation	0625456
carcinoma	I	C	IT	0629759

A.2 Lists of Materials

Table 9: Machines and equipment

Item	Manufacturer
AB 7300 Real-Time PCR System	Applied Biosystems, Foster City, CA, USA
CK 40 inverted phase contrast microscope	Olympus, Tokio, Japan
Drying chamber	Binder, Tuttlingen Germany
Fresco (microfuge)	Heraeus, Hanau, Germany
Genios Plus (microplate reader)	Tecan, Männedorf, Switzerland
Glas bottles (500 mL)	Schott, Mainz, Germany
Hera Cell (incubator)	Heraeus, Hanau, Germany
Hera Safe (safety workbench)	Heraeus, Hanau, Germany
Incubator	Memmert, Schwabach, Germany
Incubator	Binder, Tuttlingen Germany
IX 50 inverted phase contrast microscope	Olympus, Tokio, Japan
Megafuge 2.0 R (centrifuge)	Heraeus, Hanau, Germany
Mr. Frost™ (freezing container)	Thermo Fisher Scientific, Waltham, MA, USA
NanoDrop™ 1000 (spectrophotometer)	NanoDrop Technologies, Wilmington, DE, USA
Neubauer Improved (haemocytometer)	Hecht Assisstent, Sondheim, Germany
Promax 1020 (shaker)	Heidolph Instruments, Schwabach, Germany
RCT basic (magnetic stirrer)	IKA, Staufen im Breisgau, Germany

Table 9: Machines and equipment - Continued

Item	Manufacturer
Sonifier	Emerson, Ferguson, MO, USA
Synergy HAT (microplate reader)	BioTek Instruments, Winooski, VT, USA
Thermomixer R (dry block)	Eppendorf, Hamburg, Germany
Thermostatic Circulator (attached to Sonifier)	LKB, Vienna, Austria
U-RFL-T (power supplie unit)	Olympus, Tokio, Japan
Varioklav (autoclave)	HP Medizintechnik, Oberschließheim, Germany
Water bath	Köttermann, Gossau, Switzerland
Western blot equipment	Bio-Rad Laboratories, Hercules, CA, USA
xCELLigence RTCA	Hoffmann-La Roche, Basel, Switzerland

Table 10: Software

Item	Manufacturer
AB 7300 System software (V 1.4)	Applied Biosystems, Foster City, CA, USA
AnalySIS (V 3.1)	Soft Imaging System, Münster, Germany
Gen5 (V 1.11)	BioTek Instruments, Winooski, VT, USA
GNU Image Manipulation Program (GIMP)	The GIMP Team (www.gimp.org)
GraphPad Prism 4	GraphPad Software, San Diego, CA, USA
Magellan (V 5.00)	Tecan, Männedorf, Switzerland
NanoDrop-1000 (V 3.2.1)	NanoDrop Technologies, Wilmington, DE, USA
xCELLigence RTCA software (V 1.2.1)	Hoffmann-La Roche, Basel, Switzerland
xFluor (V 4.51)	Tecan, Männedorf, Switzerland

Table 11: Consumable supplies

Item	Manufacturer
Amersham Hyperfilm ECL (photofilm)	GE Healthcare, Chicago, IL, USA
Cell scraper	Greiner Bio-One, Kremsmünster, Austria
Cell strainer (40 μm)	Greiner Bio-One, Kremsmünster, Austria
Conical-bottom tubes (15 and 50 mL)	Corning, Corning, NY, USA
Cryoconservation tube (2 mL)	Corning, Corning, NY, USA
Pasteur pipettes	Wilhelm Ulbrich, Bamberg, Germany
Pipette tips (with filter)	Starlab, Hamburg, Germany
Tissue culture flask (75 mL)	Techno Plastic Products (TPP), Trasadingen, Switzerland

Table 11: Consumable supplies - Continued

Item	Manufacturer
Tissue culture flask (175 mL)	Greiner Bio-One, Kremsmünster, Austria
Microfuge tubes (0.5, 1.5 and 2 mL)	Eppendorf, Hamburg, Germany
Multiwell-plates (6, 24, 48, 96 well)	Corning, Corning, NY, USA; TPP Techno Plastic Products (TPP), Trasadingen, Switzerland
Self standing tube (5 mL)	Sarstedt, Nümbrecht, Germany

Table 12: Media

Item	Manufacturer
Dulbecco's modified Eagle's medium (DMEM)	Sigma-Aldrich, St. Louis, MO, USA
Dulbecco's phosphate-buffered saline (DPBS)	Sigma-Aldrich, St. Louis, MO, USA
Fetal bovine serum (FBS)	Sigma-Aldrich, St. Louis, MO, USA
Non-essential amino acids (NEAA)	Sigma-Aldrich, St. Louis, MO, USA
Penicillin-/Streptomycin (PEN/STREP)	Sigma-Aldrich, St. Louis, MO, USA
Trypsin-EDTA (0.05 %)	Thermo Fisher Scientific, Waltham, MA, USA

Table 13: Reagents and chemicals

Item	Manufacturer
Acetic acid	Merck, Darmstadt, Germany
Amonium persulfate (APS)	Carl Roth, Karlsruhe, Germany
β-mercaptoethanol	Carl Roth, Karlsruhe, Germany
Bovine serum albumin (BSA)	Carl Roth, Karlsruhe, Germany
Bromophenol blue	Sigma-Aldrich, St. Louis, MO, USA
Coomassie brilliant blue G-250 (dye mix)	Bio-Rad Laboratories, Hercules, CA, USA
Crystal violet	Sigma-Aldrich, St. Louis, MO, USA
Descosept AF	Dr. Schumacher, Malsfeld-Beiseförth, Germany
Dimethyl sulfaoxoide (DMSO)	Appli Chem, Darmstadt, Germany
EC™ Western Blotting Detection Kit	GE Healthcare, Chicago, IL, USA
Ethanol	
Ficoll™	Sigma-Aldrich, St. Louis, MO, USA
Formaldehyde	Carl Roth, Karlsruhe, Germany
Glycin	Carl Roth, Karlsruhe, Germany
Hydrogen chloride (HCl)	Merck, Darmstadt, Germany
IGEPAL®	Sigma-Aldrich, St. Louis, MO, USA

Table 13: Reagents and chemicals - Continued

Item	Manufacturer
Isopropanol (IPA)	Honeywell, Morris Plains, NJ, USA
Methanol (MeOH)	Honeywell, Morris Plains, NJ, USA
Non-fat dry milk	Carl Roth, Karlsruhe, Germany
NucleoSpin® RNA	Macherey-Nagel, Düren, Germany
PageRuler™	Thermo Fisher Scientific, Waltham, MA, USA
Polysorbate 20 (Tween 20)	Sigma-Aldrich, St. Louis, MO, USA
Ponceau-S	Carl Roth, Karlsruhe, Germany
Roti®-Block	Carl Roth, Karlsruhe, Germany
Sodium chloride (NaCl)	Merck, Darmstadt, Germany
Sodium dodecyl sulfate (SDS)	Carl Roth, Karlsruhe, Germany
Sulfosalicylic acid	Merck, Darmstadt, Germany
Tetramethylethylenediamine (TEMED)	Sigma-Aldrich, St. Louis, MO, USA
Trichloroacetic acid (TCA)	Carl Roth, Karlsruhe, Germany
Tris(hydroxymethyl)-aminomethan (TRIS)	Carl Roth, Karlsruhe, Germany
Triton X-100	Sigma-Aldrich, St. Louis, MO, USA
Trypan blue	Thermo Fisher Scientific, Waltham, MA, USA
Xylene cyanol	Carl Roth, Karlsruhe, Germany

A.3 Additional Information and List of Detected Genes

Table 14: List of detected genes from the RT^2 Profiler PCR array.

Position	GeneBank	Symbol	Description
A01	NM_001013779	Aim2	Absent in melanoma 2
A02	NM_026217	Atg12	Autophagy-related 12 (yeast)
A03	NM_053069	Atg5	Autophagy-related 5 (yeast)
A04	NM_013727	Azi2	5-azacytidine induced gene 2
A05	NM_001037747	Card9	Caspase recruitment domain family, member 9
A06	NM_009807	Casp1	Caspase 1
A07	NM_009812	Casp8	Caspase 8
A08	NM_011337	Ccl3	Chemokine (C-C motif) ligand 3
A09	NM_013652	Ccl4	Chemokine (C-C motif) ligand 4
A10	NM_013653	Ccl5	Chemokine (C-C motif) ligand 5

Table 14: List of detected genes from the RT^2 Profiler PCR array - Continued

Position	GeneBank	Symbol	Description
A11	NM_011611	Cd40	CD40 antigen
A12	NM_009855	Cd80	CD80 antigen
B01	NM_019388	Cd86	CD86 antigen
B02	NM_007700	Chuk	Conserved helix-loop-helix ubiquitous kinase (IKBKA)
B03	NM_028065	Cnpy3	Canopy 3 homolog (zebrafish)
B04	NM_007798	Ctsb	Cathepsin B
B05	NM_009984	Ctsl	Cathepsin L
B06	NM_021281	Ctss	Cathepsin S
B07	NM_021274	Cxcl10	Chemokine (C-X-C motif) ligand 10
B08	NM_019494	Cxcl11	Chemokine (C-X-C motif) ligand 11
B09	NM_008599	Cxcl9	Chemokine (C-X-C motif) ligand 9
B10	NM_173369	Cyld	Cylindromatosis (turban tumor syndrome)
B11	NM_145496	Dak	Dihydroxyacetone kinase 2 homolog (yeast)
B12	NM_010028	Ddx3x	DEAD/H (Asp-Glu-Ala-Asp/His) box polypeptide 3, X-linked
C01	NM_172689	Ddx58	DEAD (Asp-Glu-Ala-Asp) box polypeptide 58 (RIG-1)
C02	NM_030150	Dhx58	DEXH (Asp-Glu-X-His) box polypeptide 58
C03	NM_010175	Fadd	Fas (TNFRSF6)-associated via death domain
C04	NM_010234	Fos	FBJ osteosarcoma oncogene
C05	NM_010480	Hsp90aa1	Heat shock protein 90, alpha (cytosolic), class A member 1
C06	NM_027835	Ifih1	Interferon induced with helicase C domain 1 (MDA5)
C07	NM_010503	Ifna2	Interferon alpha 2
C08	NM_010508	Ifnar1	Interferon (alpha and beta) receptor 1
C09	NM_010510	Ifnb1	Interferon beta 1, fibroblast
C10	NM_010546	Ikbkb	Inhibitor of kappaB kinase beta
C11	NM_008351	Il12a	Interleukin 12A
C12	NM_008352	Il12b	Interleukin 12B
D01	NM_008357	Il15	Interleukin 15
D02	NM_008360	Il18	Interleukin 18
D03	NM_008361	Il1b	Interleukin 1 beta
D04	NM_031168	Il6	Interleukin 6
D05	NM_008363	Irak1	Interleukin-1 receptor-associated kinase 1
D06	NM_016849	Irf3	Interferon regulatory factor 3

Table 14: List of detected genes from the RT^2 Profiler PCR array - Continued

Position	GeneBank	Symbol	Description
D07	NM_012057	Irf5	Interferon regulatory factor 5
D08	NM_016850	Irf7	Interferon regulatory factor 7
D09	NM_015783	Isg15	ISG15 ubiquitin-like modifier
D10	NM_010591	Jun	Jun oncogene
D11	NM_008927	Map2k1	Mitogen-activated protein kinase kinase 1
D12	NM_008928	Map2k3	Mitogen-activated protein kinase kinase 3
E01	NM_011945	Map3k1	Mitogen-activated protein kinase kinase kinase 1
E02	NM_172688	Map3k7	Mitogen-activated protein kinase kinase kinase 7
E03	NM_011949	Mapk1	Mitogen-activated protein kinase 1
E04	NM_011951	Mapk14	Mitogen-activated protein kinase 14
E05	NM_011952	Mapk3	Mitogen-activated protein kinase 3
E06	NM_016700	Mapk8	Mitogen-activated protein kinase 8
E07	NM_144888	Mavs	Mitochondrial antiviral signaling protein
E08	NM_019453	Mefv	Mediterranean fever
E09	NM_010846	Mx1	Myxovirus (influenza virus) resistance 1
E10	NM_010851	Myd88	Myeloid differentiation primary response gene 88
E11	NM_008689	Nfkb1	Nuclear factor of kappa light polypeptide gene enhancer in B-cells 1, p105
E12	NM_010907	Nfkbia	Nuclear factor of kappa light polypeptide gene enhancer in B-cells inhibitor, alpha
F01	NM_145827	Nlrp3	NLR family, pyrin domain containing 3
F02	NM_145857	Nod2	Nucleotide-binding oligomerization domain containing 2
F03	NM_145227	Oas2	2'-5' oligoadenylate synthetase 2
F04	NM_023371	Pin1	Protein (peptidyl-prolyl cis/trans isomerase) NIMA-interacting 1
F05	NM_011193	Pstpip1	Proline-serine-threonine phosphatase-interacting protein 1
F06	NM_023258	Pycard	PYD and CARD domain containing
F07	NM_009045	Rela	V-rel reticuloendotheliosis viral oncogene homolog A (avian), p65 NF-kappa B
F08	NM_009068	Ripk1	Receptor (TNFRSF)-interacting serine-threonine kinase 1
F09	NM_009263	Spp1	Secreted phosphoprotein 1
F10	NM_009283	Stat1	Signal transducer and activator of transcription 1

Table 14: List of detected genes from the RT^2 Profiler PCR array - Continued

Position	GeneBank	Symbol	Description
F11	NM_026474	Sugt1	SGT1, suppressor of G2 allele of SKP1 (S. cerevisiae)
F12	NM_011529	Tank	TRAF family member-associated Nf-kappa B activator
G01	NM_019786	Tbk1	TANK-binding kinase 1
G02	NM_198100	Tbkbp1	TBK1 binding protein 1
G03	NM_174989	Ticam1	Toll-like receptor adaptor molecule 1
G04	NM_126166	Tlr3	Toll-like receptor 3
G05	NM_133211	Tlr7	Toll-like receptor 7
G06	NM_133212	Tlr8	Toll-like receptor 8
G07	NM_031178	Tlr9	Toll-like receptor 9
G08	NM_013693	Tnf	Tumor necrosis factor
G09	NM_001033161	Tradd	TNFRSF1A-associated via death domain
G10	NM_011632	Traf3	Tnf receptor-associated factor 3
G11	NM_009424	Traf6	Tnf receptor-associated factor 6
G12	NM_009546	Trim25	Tripartite motif-containing 25
H01	NM_007393	Actb	Actin, beta
H02	NM_009735	B2m	Beta-2 microglobulin
H03	NM_008084	Gapdh	Glyceraldehyde-3-phosphate dehydrogenase
H04	NM_010368	Gusb	Glucuronidase, beta
H05	NM_008302	Hsp90ab1	Heat shock protein 90, alpha (cytosolic), class B member 1
H06	SA_00106	MGDC	Mouse Genomic DNA Contamination
H07	SA_00104	RTC	Reverse Transcription Control
H08	SA_00104	RTC	Reverse Transcription Control
H09	SA_00104	RTC	Reverse Transcription Control
H10	SA_00103	PPC	Positive PCR Control
H11	SA_00103	PPC	Positive PCR Control
H12	SA_00103	PPC	Positive PCR Control

Bibliography

[1] J. Ferlay, M. Colombet, I. Soerjomataram, C. Mathers, D. M. Parkin, M. Pineros, A. Znaor, and F. Bray. Estimating the global cancer incidence and mortality in 2018: Globocan sources and methods. *Int J Cancer*, 144(8):1941–1953, 2019.

[2] F. X. Bosch, J. Ribes, M. Diaz, and R. Cleries. Primary liver cancer: worldwide incidence and trends. *Gastroenterology*, 127(5 Suppl 1):S5–S16, 2004.

[3] M. Sherman. Hepatocellular carcinoma: epidemiology, surveillance, and diagnosis. *Semin Liver Dis*, 30(1):3–16, 2010.

[4] M. Sherman. Hepatocellular carcinoma: epidemiology, risk factors, and screening. *Semin Liver Dis*, 25(2):143–54, 2005.

[5] A. Forner, J. M. Llovet, and J. Bruix. Hepatocellular carcinoma. *Lancet*, 379(9822):1245–55, 2012.

[6] C. L. Lin and J. H. Kao. Review article: the prevention of hepatitis b-related hepatocellular carcinoma. *Aliment Pharmacol Ther*, 48(1):5–14, 2018.

[7] Y. T. Wang, T. Y. Chen, J. Zhu, Y. C. Jiao, and C. F. Qu. [primary prevention by hepatitis b vaccine on liver cancer in high incidence area of china]. *Zhonghua Yu Fang Yi Xue Za Zhi*, 52(4):402–408, 2018.

[8] M. H. Chang, S. L. You, C. J. Chen, C. J. Liu, M. W. Lai, T. C. Wu, S. F. Wu, C. M. Lee, S. S. Yang, H. C. Chu, T. E. Wang, B. W. Chen, W. L. Chuang, M. S. Soon, C. Y. Lin, S. T. Chiou, H. S. Kuo, D. S. Chen, and Group Taiwan

Hepatoma Study. Long-term effects of hepatitis b immunization of infants in preventing liver cancer. *Gastroenterology*, 151(3):472–480 e1, 2016.

[9] H. Hayashi, K. Sugio, T. Matsumata, E. Adachi, K. Takenaka, and K. Sugimachi. The clinical significance of p53 gene mutation in hepatocellular carcinomas from japan. *Hepatology*, 22(6):1702–7, 1995.

[10] P. A. Farazi and R. A. DePinho. Hepatocellular carcinoma pathogenesis: from genes to environment. *Nat Rev Cancer*, 6(9):674–87, 2006.

[11] A. Villanueva, P. Newell, D. Y. Chiang, S. L. Friedman, and J. M. Llovet. Genomics and signaling pathways in hepatocellular carcinoma. *Semin Liver Dis*, 27(1):55–76, 2007.

[12] B. T. MacDonald, K. Tamai, and X. He. Wnt/beta-catenin signaling: components, mechanisms, and diseases. *Dev Cell*, 17(1):9–26, 2009.

[13] J. K. Sicklick, Y. X. Li, A. Jayaraman, R. Kannangai, Y. Qi, P. Vivekanandan, J. W. Ludlow, K. Owzar, W. Chen, M. S. Torbenson, and A. M. Diehl. Dysregulation of the hedgehog pathway in human hepatocarcinogenesis. *Carcinogenesis*, 27(4):748–57, 2006.

[14] S. Kawate, T. Fukusato, S. Ohwada, A. Watanuki, and Y. Morishita. Amplification of c-myc in hepatocellular carcinoma: correlation with clinicopathologic features, proliferative activity and p53 overexpression. *Oncology*, 57(2):157–63, 1999.

[15] D. F. Calvisi and S. S. Thorgeirsson. Molecular mechanisms of hepatocarcinogenesis in transgenic mouse models of liver cancer. *Toxicol Pathol*, 33(1):181–4, 2005.

[16] Y. Ito, T. Takeda, M. Sakon, M. Tsujimoto, S. Higashiyama, K. Noda, E. Miyoshi, M. Monden, and N. Matsuura. Expression and clinical significance of erb-b receptor family in hepatocellular carcinoma. *Br J Cancer*, 84(10):1377–83, 2001.

[17] M. Fernandez, D. Semela, J. Bruix, I. Colle, M. Pinzani, and J. Bosch.

Angiogenesis in liver disease. *J Hepatol*, 50(3):604–20, 2009.

[18] Y. Fujiwara, D. S. Hoon, T. Yamada, K. Umeshita, M. Gotoh, M. Sakon, I. Nishisho, and M. Monden. Pten / mmac1 mutation and frequent loss of heterozygosity identified in chromosome 10q in a subset of hepatocellular carcinomas. *Jpn J Cancer Res*, 91(3):287–92, 2000.

[19] J. M. Llovet, C. Bru, and J. Bruix. Prognosis of hepatocellular carcinoma: the bclc staging classification. *Semin Liver Dis*, 19(3):329–38, 1999.

[20] G. M. Keating and A. Santoro. Sorafenib: a review of its use in advanced hepatocellular carcinoma. *Drugs*, 69(2):223–40, 2009.

[21] Masatoshi Kudo, Richard S Finn, Shukui Qin, Kwang-Hyub Han, Kenji Ikeda, Fabio Piscaglia, Ari Baron, Joong-Won Park, Guohong Han, and Jacek Jassem. Lenvatinib versus sorafenib in first-line treatment of patients with unresectable hepatocellular carcinoma: a randomised phase 3 non-inferiority trial. *The Lancet*, 391(10126):1163–1173, 2018.

[22] Richard S Finn, Shukui Qin, Masafumi Ikeda, Peter R Galle, Michel Ducreux, Tae-You Kim, Masatoshi Kudo, Valeriy Breder, Philippe Merle, and Ahmed O Kaseb. Atezolizumab plus bevacizumab in unresectable hepatocellular carcinoma. *New England Journal of Medicine*, 382(20):1894–1905, 2020.

[23] A Vogel, A Cervantes, I Chau, B Daniele, JM Llovet, T Meyer, J-C Nault, U Neumann, J Ricke, and B Sangro. Hepatocellular carcinoma: Esmo clinical practice guidelines for diagnosis, treatment and follow-up. *Annals of Oncology*, 30(5):871–873, 2019.

[24] J. M. Llovet, S. Ricci, V. Mazzaferro, P. Hilgard, E. Gane, J. F. Blanc, A. C. de Oliveira, A. Santoro, J. L. Raoul, A. Forner, M. Schwartz, C. Porta, S. Zeuzem, L. Bolondi, T. F. Greten, P. R. Galle, J. F. Seitz, I. Borbath, D. Haussinger, T. Giannaris, M. Shan, M. Moscovici, D. Voliotis, J. Bruix, and Sharp Investigators Study Group. Sorafenib in advanced hepatocellular carcinoma. *N Engl J Med*, 359(4):378–90, 2008.

[25] S. J. Russell, K. W. Peng, and J. C. Bell. Oncolytic virotherapy. *Nat Biotechnol*, 30(7):658–70, 2012.

[26] L. Russell and K. W. Peng. The emerging role of oncolytic virus therapy against cancer. *Chin Clin Oncol*, 7(2):16, 2018.

[27] K. Garber. China approves world's first oncolytic virus therapy for cancer treatment. *J Natl Cancer Inst*, 98(5):298–300, 2006.

[28] R. Cattaneo, T. Miest, E. V. Shashkova, and M. A. Barry. Reprogrammed viruses as cancer therapeutics: targeted, armed and shielded. *Nat Rev Microbiol*, 6(7):529–40, 2008.

[29] S. J. Russell, M. J. Federspiel, K. W. Peng, C. Tong, D. Dingli, W. G. Morice, V. Lowe, M. K. O'Connor, R. A. Kyle, N. Leung, F. K. Buadi, S. V. Rajkumar, M. A. Gertz, M. Q. Lacy, and A. Dispenzieri. Remission of disseminated cancer after systemic oncolytic virotherapy. *Mayo Clin Proc*, 89(7):926–33, 2014.

[30] S. Gross. Measles and leukaemia. *Lancet*, 1(7695):397–8, 1971.

[31] A. Z. Bluming and J. L. Ziegler. Regression of burkitt's lymphoma in association with measles infection. *Lancet*, 2(7715):105–6, 1971.

[32] E. Kelly and S. J. Russell. History of oncolytic viruses: genesis to genetic engineering. *Mol Ther*, 15(4):651–9, 2007.

[33] H. L. Kaufman, F. J. Kohlhapp, and A. Zloza. Oncolytic viruses: a new class of immunotherapy drugs. *Nat Rev Drug Discov*, 14(9):642–62, 2015.

[34] R. H. Andtbacka, H. L. Kaufman, F. Collichio, T. Amatruda, N. Senzer, J. Chesney, K. A. Delman, L. E. Spitler, I. Puzanov, S. S. Agarwala, M. Milhem, L. Cranmer, B. Curti, K. Lewis, M. Ross, T. Guthrie, G. P. Linette, G. A. Daniels, K. Harrington, M. R. Middleton, Jr. Miller, W. H., J. S. Zager, Y. Ye, B. Yao, A. Li, S. Doleman, A. VanderWalde, J. Gansert, and R. S. Coffin. Talimogene laherparepvec improves durable response rate in patients with advanced melanoma. *J Clin Oncol*, 33(25):2780–8, 2015.

[35] D. Hanahan and R. A. Weinberg. Hallmarks of cancer: the next generation. *Cell*, 144(5):646–74, 2011.

[36] L. A. Pikor, J. C. Bell, and J. S. Diallo. Oncolytic viruses: Exploiting cancer's deal with the devil. *Trends Cancer*, 1(4):266–277, 2015.

[37] B. L. Liu, M. Robinson, Z. Q. Han, R. H. Branston, C. English, P. Reay, Y. McGrath, S. K. Thomas, M. Thornton, P. Bullock, C. A. Love, and R. S. Coffin. Icp34.5 deleted herpes simplex virus with enhanced oncolytic, immune stimulating, and anti-tumour properties. *Gene Ther*, 10(4):292–303, 2003.

[38] C. J. Buchholz, T. Friedel, and H. Buning. Surface-engineered viral vectors for selective and cell type-specific gene delivery. *Trends Biotechnol*, 33(12):777–790, 2015.

[39] E. Gurlevik, P. Schache, A. Goez, A. Kloos, N. Woller, N. Armbrecht, M. P. Manns, S. Kubicka, and F. Kuhnel. Meganuclease-mediated virus self-cleavage facilitates tumor-specific virus replication. *Mol Ther*, 21(9):1738–48, 2013.

[40] T. L. DeWeese, H. van der Poel, S. Li, B. Mikhak, R. Drew, M. Goemann, U. Hamper, R. DeJong, N. Detorie, R. Rodriguez, T. Haulk, A. M. DeMarzo, S. Piantadosi, D. C. Yu, Y. Chen, D. R. Henderson, M. A. Carducci, W. G. Nelson, and J. W. Simons. A phase i trial of cv706, a replication-competent, psa selective oncolytic adenovirus, for the treatment of locally recurrent prostate cancer following radiation therapy. *Cancer Res*, 61(20):7464–72, 2001.

[41] Z. S. Guo, Z. Liu, and D. L. Bartlett. Oncolytic immunotherapy: Dying the right way is a key to eliciting potent antitumor immunity. *Front Oncol*, 4:74, 2014.

[42] D. Zamarin, R. B. Holmgaard, S. K. Subudhi, J. S. Park, M. Mansour, P. Palese, T. Merghoub, J. D. Wolchok, and J. P. Allison. Localized oncolytic virotherapy overcomes systemic tumor resistance to immune checkpoint blockade immunotherapy. *Sci Transl Med*, 6(226):226ra32, 2014.

[43] M. Z. Tesfay, A. C. Kirk, E. M. Hadac, G. E. Griesmann, M. J. Federspiel, G. N. Barber, S. M. Henry, K. W. Peng, and S. J. Russell. Pegylation of vesicular stomatitis virus extends virus persistence in blood circulation of passively immunized mice. *J Virol*, 87(7):3752–9, 2013.

[44] J. Morrison, S. S. Briggs, N. Green, K. Fisher, V. Subr, K. Ulbrich, S. Kehoe, and L. W. Seymour. Virotherapy of ovarian cancer with polymer-cloaked adenovirus retargeted to the epidermal growth factor receptor. *Mol Ther*, 16(2):244–51, 2008.

[45] C. Springfeld, V. von Messling, M. Frenzke, G. Ungerechts, C. J. Buchholz, and R. Cattaneo. Oncolytic efficacy and enhanced safety of measles virus activated by tumor-secreted matrix metalloproteinases. *Cancer Res*, 66(15):7694–700, 2006.

[46] F. J. Kohlhapp and H. L. Kaufman. Molecular pathways: Mechanism of action for talimogene laherparepvec, a new oncolytic virus immunotherapy. *Clin Cancer Res*, 22(5):1048–54, 2016.

[47] Q. Zhang, Y. A. Yu, E. Wang, N. Chen, R. L. Danner, P. J. Munson, F. M. Marincola, and A. A. Szalay. Eradication of solid human breast tumors in nude mice with an intravenously injected light-emitting oncolytic vaccinia virus. *Cancer Res*, 67(20):10038–46, 2007.

[48] S. Lal, U. M. Lauer, D. Niethammer, J. F. Beck, and P. G. Schlegel. Suicide genes: past, present and future perspectives. *Immunol Today*, 21(1):48–54, 2000.

[49] J. Lampe, S. Bossow, T. Weiland, I. Smirnow, R. Lehmann, W. Neubert, M. Bitzer, and U. M. Lauer. An armed oncolytic measles vaccine virus eliminates human hepatoma cells independently of apoptosis. *Gene Ther*, 20(11):1033–41, 2013.

[50] C. Yurttas, S. Berchtold, N. P. Malek, M. Bitzer, and U. M. Lauer. Pulsed versus continuous application of the prodrug 5-fluorocytosine to enhance the oncolytic effectiveness of a measles vaccine virus armed with a suicide gene. *Hum Gene Ther Clin Dev*, 25(2):85–96, 2014.

[51] N. Woller, E. Gurlevik, B. Fleischmann-Mundt, A. Schumacher, S. Knocke, A. M. Kloos, M. Saborowski, R. Geffers, M. P. Manns, T. C. Wirth, S. Kubicka, and F. Kuhnel. Viral infection of tumors overcomes resistance to pd-1-immunotherapy by broadening neoantigenome-directed t-cell responses. *Mol Ther*, 23(10):1630–40, 2015.

[52] Y. Shen and J. Nemunaitis. Fighting cancer with vaccinia virus: teaching new tricks to an old dog. *Mol Ther*, 11(2):180–95, 2005.

[53] B. Moss. Poxvirus dna replication. *Cold Spring Harb Perspect Biol*, 5(9), 2013.

[54] M. Puhlmann, C. K. Brown, M. Gnant, J. Huang, S. K. Libutti, H. R. Alexander, and D. L. Bartlett. Vaccinia as a vector for tumor-directed gene therapy: biodistribution of a thymidine kinase-deleted mutant. *Cancer Gene Ther*, 7(1):66–73, 2000.

[55] G. C. Spagnoli, P. Zajac, W. R. Marti, D. Oertli, E. Padovan, C. Noppen, T. Kocher, M. Adamina, and M. Heberer. Cytotoxic t-cell induction in metastatic melanoma patients undergoing recombinant vaccinia virus-based immuno-gene therapy. *Recent Results Cancer Res*, 160:195–201, 2002.

[56] J. Cono, C. G. Casey, D. M. Bell, Control Centers for Disease, and Prevention. Smallpox vaccination and adverse reactions. guidance for clinicians. *MMWR Recomm Rep*, 52(RR-4):1–28, 2003.

[57] B Moss. *Fields virology*, volume 2, chapter Poxviridae, p 2129–2159. Lippincott Williams & Wilki, 6th edition, 2013.

[58] Jr. Roenigk, H. H., S. Deodhar, R. St Jacques, and K. Burdick. Immunotherapy of malignant melanoma with vaccinia virus. *Arch Dermatol*, 109(5):668–73, 1974.

[59] R. M. Hansen and J. A. Libnoch. Remission of chronic lymphocytic leukemia after smallpox vaccination. *Arch Intern Med*, 138(7):1137–8, 1978.

[60] M. J. Mastrangelo and E. C. Lattime. Virotherapy clinical trials for regional disease: in situ immune modulation using recombinant poxvirus vectors. *Cancer Gene Ther*, 9(12):1013–21, 2002.

[61] Q. Zhang, C. Liang, Y. A. Yu, N. Chen, T. Dandekar, and A. A. Szalay. The highly attenuated oncolytic recombinant vaccinia virus glv-1h68: comparative genomic features and the contribution of f14.5l inactivation. *Mol Genet Genomics*, 282(4):417–35, 2009.

[62] U. M. Lauer, M. Schell, J. Beil, S. Berchtold, U. Koppenhofer, J. Glatzle, A. Konigsrainer, R. Mohle, D. Nann, F. Fend, C. Pfannenberg, M. Bitzer, and N. P. Malek. Phase i study of oncolytic vaccinia virus gl-onc1 in patients with peritoneal carcinomatosis. *Clin Cancer Res*, 24(18):4388–4398, 2018.

[63] J. H. Kim, J. Y. Oh, B. H. Park, D. E. Lee, J. S. Kim, H. E. Park, M. S. Roh, J. E. Je, J. H. Yoon, S. H. Thorne, D. Kirn, and T. H. Hwang. Systemic armed oncolytic and immunologic therapy for cancer with jx-594, a targeted poxvirus expressing gm-csf. *Mol Ther*, 14(3):361–70, 2006.

[64] K. A. Parato, C. J. Breitbach, F. Le Boeuf, J. Wang, C. Storbeck, C. Ilkow, J. S. Diallo, T. Falls, J. Burns, V. Garcia, F. Kanji, L. Evgin, K. Hu, F. Paradis, S. Knowles, T. H. Hwang, B. C. Vanderhyden, R. Auer, D. H. Kirn, and J. C. Bell. The oncolytic poxvirus jx-594 selectively replicates in and destroys cancer cells driven by genetic pathways commonly activated in cancers. *Mol Ther*, 20(4):749–58, 2012.

[65] C. J. Breitbach, J. M. Paterson, C. G. Lemay, T. J. Falls, A. McGuire, K. A. Parato, D. F. Stojdl, M. Daneshmand, K. Speth, D. Kirn, J. A. McCart, H. Atkins, and J. C. Bell. Targeted inflammation during oncolytic virus therapy severely compromises tumor blood flow. *Mol Ther*, 15(9):1686–93, 2007.

[66] C. J. Breitbach, R. Arulanandam, N. De Silva, S. H. Thorne, R. Patt, M. Daneshmand, A. Moon, C. Ilkow, J. Burke, T. H. Hwang, J. Heo, M. Cho, H. Chen, F. A. Angarita, C. Addison, J. A. McCart, J. C. Bell, and D. H. Kirn. Oncolytic vaccinia virus disrupts tumor-associated vasculature in humans. *Cancer Res*, 73(4):1265–75, 2013.

[67] T. P. Cripe, M. C. Ngo, J. I. Geller, C. U. Louis, M. A. Currier, J. M. Racadio, A. J. Towbin, C. M. Rooney, A. Pelusio, A. Moon, T. H. Hwang, J. M. Burke, J. C. Bell, D. H. Kirn, and C. J. Breitbach. Phase 1 study of intratumoral pexa-vec (jx-594), an oncolytic and immunotherapeutic vaccinia virus, in pediatric cancer patients. *Mol Ther*, 23(3):602–8, 2015.

[68] C. J. Breitbach, J. C. Bell, T. H. Hwang, D. H. Kirn, and J. Burke. The emerging therapeutic potential of the oncolytic immunotherapeutic pexa-vec (jx-594). *Oncolytic Virother*, 4:25–31, 2015.

[69] J. Heo, C. J. Breitbach, A. Moon, C. W. Kim, R. Patt, M. K. Kim, Y. K. Lee, S. Y. Oh, H. Y. Woo, K. Parato, J. Rintoul, T. Falls, T. Hickman, B. G. Rhee, J. C. Bell, D. H. Kirn, and T. H. Hwang. Sequential therapy with jx-594, a targeted oncolytic poxvirus, followed by sorafenib in hepatocellular carcinoma: preclinical and clinical demonstration of combination efficacy. *Mol Ther*, 19(6):1170–9, 2011.

[70] J. Trowsdale and P. Parham. Mini-review: defense strategies and immunity-related genes. *Eur J Immunol*, 34(1):7–17, 2004.

[71] O. Takeuchi and S. Akira. Pattern recognition receptors and inflammation. *Cell*, 140(6):805–20, 2010.

[72] M. Yoneyama, M. Kikuchi, T. Natsukawa, N. Shinobu, T. Imaizumi, M. Miyagishi, K. Taira, S. Akira, and T. Fujita. The rna helicase rig-i has an essential function in double-stranded rna-induced innate antiviral responses. *Nat Immunol*, 5(7):730–7, 2004.

[73] D. C. Kang, R. V. Gopalkrishnan, L. Lin, A. Randolph, K. Valerie, S. Pestka, and P. B. Fisher. Expression analysis and genomic characterization of human melanoma differentiation associated gene-5, mda-5: a novel type i interferon-responsive apoptosis-inducing gene. *Oncogene*, 23(9):1789–800, 2004.

[74] A. Pichlmair, O. Schulz, C. P. Tan, J. Rehwinkel, H. Kato, O. Takeuchi, S. Akira, M. Way, G. Schiavo, and C. Reis e Sousa. Activation of mda5 re-

quires higher-order rna structures generated during virus infection. *J Virol*, 83(20):10761–9, 2009.

[75] M. Yoneyama, M. Kikuchi, K. Matsumoto, T. Imaizumi, M. Miyagishi, K. Taira, E. Foy, Y. M. Loo, Jr. Gale, M., S. Akira, S. Yonehara, A. Kato, and T. Fujita. Shared and unique functions of the dexd/h-box helicases rig-i, mda5, and lgp2 in antiviral innate immunity. *J Immunol*, 175(5):2851–8, 2005.

[76] L. Unterholzner. The interferon response to intracellular dna: why so many receptors? *Immunobiology*, 218(11):1312–21, 2013.

[77] A. Takaoka, Z. Wang, M. K. Choi, H. Yanai, H. Negishi, T. Ban, Y. Lu, M. Miyagishi, T. Kodama, K. Honda, Y. Ohba, and T. Taniguchi. Dai (dlm-1/zbp1) is a cytosolic dna sensor and an activator of innate immune response. *Nature*, 448(7152):501–5, 2007.

[78] Z. Zhang, B. Yuan, M. Bao, N. Lu, T. Kim, and Y. J. Liu. The helicase ddx41 senses intracellular dna mediated by the adaptor sting in dendritic cells. *Nat Immunol*, 12(10):959–65, 2011.

[79] L. Unterholzner, S. E. Keating, M. Baran, K. A. Horan, S. B. Jensen, S. Sharma, C. M. Sirois, T. Jin, E. Latz, T. S. Xiao, K. A. Fitzgerald, S. R. Paludan, and A. G. Bowie. Ifi16 is an innate immune sensor for intracellular dna. *Nat Immunol*, 11(11):997–1004, 2010.

[80] L. Sun, J. Wu, F. Du, X. Chen, and Z. J. Chen. Cyclic gmp-amp synthase is a cytosolic dna sensor that activates the type i interferon pathway. *Science*, 339(6121):786–91, 2013.

[81] V. Hornung, A. Ablasser, M. Charrel-Dennis, F. Bauernfeind, G. Horvath, D. R. Caffrey, E. Latz, and K. A. Fitzgerald. Aim2 recognizes cytosolic dsdna and forms a caspase-1-activating inflammasome with asc. *Nature*, 458(7237):514–8, 2009.

[82] O. Takeuchi and S. Akira. Mda5/rig-i and virus recognition. *Curr Opin Immunol*, 20(1):17–22, 2008.

[83] P. J. Maglione, N. Simchoni, and C. Cunningham-Rundles. Toll-like receptor signaling in primary immune deficiencies. *Ann N Y Acad Sci*, 1356:1–21, 2015.

[84] E. M. Moresco, D. LaVine, and B. Beutler. Toll-like receptors. *Curr Biol*, 21(13):R488–93, 2011.

[85] J. W. Schoggins and C. M. Rice. Interferon-stimulated genes and their antiviral effector functions. *Curr Opin Virol*, 1(6):519–25, 2011.

[86] P. Domanski, M. Witte, M. Kellum, M. Rubinstein, R. Hackett, P. Pitha, and O. R. Colamonici. Cloning and expression of a long form of the beta subunit of the interferon alpha beta receptor that is required for signaling. *J Biol Chem*, 270(37):21606–11, 1995.

[87] M. Sakatsume, K. Igarashi, K. D. Winestock, G. Garotta, A. C. Larner, and D. S. Finbloom. The jak kinases differentially associate with the alpha and beta (accessory factor) chains of the interferon gamma receptor to form a functional receptor unit capable of activating stat transcription factors. *J Biol Chem*, 270(29):17528–34, 1995.

[88] N. W. Bartlett, K. Buttigieg, S. V. Kotenko, and G. L. Smith. Murine interferon lambdas (type iii interferons) exhibit potent antiviral activity in vivo in a poxvirus infection model. *J Gen Virol*, 86(Pt 6):1589–1596, 2005.

[89] G. R. Stark, I. M. Kerr, B. R. Williams, R. H. Silverman, and R. D. Schreiber. How cells respond to interferons. *Annu Rev Biochem*, 67:227–64, 1998.

[90] C. E. Samuel. Antiviral actions of interferons. *Clin Microbiol Rev*, 14(4):778–809, table of contents, 2001.

[91] W. M. Schneider, M. D. Chevillotte, and C. M. Rice. Interferon-stimulated genes: a complex web of host defenses. *Annu Rev Immunol*, 32:513–45, 2014.

[92] A. Roobol, J. Roobol, A. Bastide, J. R. Knight, A. E. Willis, and C. M. Smales. p58ipk is an inhibitor of the eif2alpha kinase gcn2 and its localiza-

tion and expression underpin protein synthesis and er processing capacity. *Biochem J*, 465(2):213–25, 2015.

[93] J. Gil, M. A. Garcia, P. Gomez-Puertas, S. Guerra, J. Rullas, H. Nakano, J. Alcami, and M. Esteban. Traf family proteins link pkr with nf-kappa b activation. *Mol Cell Biol*, 24(10):4502–12, 2004.

[94] J. Gil and M. Esteban. The interferon-induced protein kinase (pkr), triggers apoptosis through fadd-mediated activation of caspase 8 in a manner independent of fas and tnf-alpha receptors. *Oncogene*, 19(32):3665–74, 2000.

[95] B. Dong, L. Xu, A. Zhou, B. A. Hassel, X. Lee, P. F. Torrence, and R. H. Silverman. Intrinsic molecular activities of the interferon-induced 2-5a-dependent rnase. *J Biol Chem*, 269(19):14153–8, 1994.

[96] O. Haller and G. Kochs. Interferon-induced mx proteins: dynamin-like gtpases with antiviral activity. *Traffic*, 3(10):710–7, 2002.

[97] K. Turan, M. Mibayashi, K. Sugiyama, S. Saito, A. Numajiri, and K. Nagata. Nuclear mxa proteins form a complex with influenza virus np and inhibit the transcription of the engineered influenza virus genome. *Nucleic Acids Res*, 32(2):643–52, 2004.

[98] D. Dauch, R. Rudalska, G. Cossa, J. C. Nault, T. W. Kang, T. Wuestefeld, A. Hohmeyer, S. Imbeaud, T. Yevsa, L. Hoenicke, T. Pantsar, P. Bozko, N. P. Malek, T. Longerich, S. Laufer, A. Poso, J. Zucman-Rossi, M. Eilers, and L. Zender. A myc-aurora kinase a protein complex represents an actionable drug target in p53-altered liver cancer. *Nat Med*, 22(7):744–53, 2016.

[99] Oscar Bastidas. Cell counting with neubauer chamber, basic hemocytometer usage. *Technical Note-Neubauer Chamber Cell Counting*, 2013.

[100] Marlene Absher. Hemocytometer counting. In *Tissue culture*, pages 395–397. Elsevier, 1973.

[101] D. Shcherbo, E. M. Merzlyak, T. V. Chepurnykh, A. F. Fradkov, G. V. Er-

makova, E. A. Solovieva, K. A. Lukyanov, E. A. Bogdanova, A. G. Zaraisky, S. Lukyanov, and D. M. Chudakov. Bright far-red fluorescent protein for whole-body imaging. *Nat Methods*, 4(9):741–6, 2007.

[102] P. Skehan, R. Storeng, D. Scudiero, A. Monks, J. McMahon, D. Vistica, J. T. Warren, H. Bokesch, S. Kenney, and M. R. Boyd. New colorimetric cytotoxicity assay for anticancer-drug screening. *J Natl Cancer Inst*, 82(13):1107–12, 1990.

[103] V. Vichai and K. Kirtikara. Sulforhodamine b colorimetric assay for cytotoxicity screening. *Nat Protoc*, 1(3):1112–6, 2006.

[104] K. Solly, X. Wang, X. Xu, B. Strulovici, and W. Zheng. Application of real-time cell electronic sensing (rt-ces) technology to cell-based assays. *Assay Drug Dev Technol*, 2(4):363–72, 2004.

[105] M. M. Bradford. A rapid and sensitive method for the quantitation of microgram quantities of protein utilizing the principle of protein-dye binding. *Anal Biochem*, 72:248–54, 1976.

[106] U. K. Laemmli. Cleavage of structural proteins during the assembly of the head of bacteriophage t4. *Nature*, 227(5259):680–5, 1970.

[107] S. Berchtold, J. Lampe, T. Weiland, I. Smirnow, S. Schleicher, R. Handgretinger, H. G. Kopp, J. Reiser, F. Stubenrauch, N. Mayer, N. P. Malek, M. Bitzer, and U. M. Lauer. Innate immune defense defines susceptibility of sarcoma cells to measles vaccine virus-based oncolysis. *J Virol*, 87(6):3484–501, 2013.

[108] I. Gentschev, M. Muller, M. Adelfinger, S. Weibel, F. Grummt, M. Zimmermann, M. Bitzer, M. Heisig, Q. Zhang, Y. A. Yu, N. G. Chen, J. Stritzker, U. M. Lauer, and A. A. Szalay. Efficient colonization and therapy of human hepatocellular carcinoma (hcc) using the oncolytic vaccinia virus strain glv-1h68. *PLoS One*, 6(7):e22069, 2011.

[109] J. W. Ady, C. Johnsen, K. Mojica, J. Heffner, D. Love, A. Pugalenthi, L. J. Belin, N. G. Chen, Y. A. Yu, A. A. Szalay, and Y. Fong. Oncolytic gene

therapy with recombinant vaccinia strain glv-2b372 efficiently kills hepatocellular carcinoma. *Surgery*, 158(2):331–8, 2015.

[110] D. Tsoneva, B. Minev, A. Frentzen, Q. Zhang, A. K. Wege, and A. A. Szalay. Humanized mice with subcutaneous human solid tumors for immune response analysis of vaccinia virus-mediated oncolysis. *Mol Ther Oncolytics*, 5:41–61, 2017.

[111] G. Song, G. Ouyang, and S. Bao. The activation of akt/pkb signaling pathway and cell survival. *J Cell Mol Med*, 9(1):59–71, 2005.

[112] M. J. Wilkinson, H. G. Smith, G. McEntee, J. Kyula-Currie, T. D. Pencavel, D. C. Mansfield, A. A. Khan, V. Roulstone, A. J. Hayes, and K. J. Harrington. Oncolytic vaccinia virus combined with radiotherapy induces apoptotic cell death in sarcoma cells by down-regulating the inhibitors of apoptosis. *Oncotarget*, 7(49):81208–81222, 2016.

[113] S. Balachandran, M. Porosnicu, and G. N. Barber. Oncolytic activity of vesicular stomatitis virus is effective against tumors exhibiting aberrant p53, ras, or myc function and involves the induction of apoptosis. *J Virol*, 75(7):3474–9, 2001.

[114] S. Greiner, J. Y. Humrich, P. Thuman, B. Sauter, G. Schuler, and L. Jenne. The highly attenuated vaccinia virus strain modified virus ankara induces apoptosis in melanoma cells and allows bystander dendritic cells to generate a potent anti-tumoral immunity. *Clin Exp Immunol*, 146(2):344–53, 2006.

[115] W. M. Abida and W. Gu. p53-dependent and p53-independent activation of autophagy by arf. *Cancer Res*, 68(2):352–7, 2008.

[116] J. P. Brown, D. R. Twardzik, H. Marquardt, and G. J. Todaro. Vaccinia virus encodes a polypeptide homologous to epidermal growth factor and transforming growth factor. *Nature*, 313(6002):491–2, 1985.

[117] R. M. Buller, S. Chakrabarti, J. A. Cooper, D. R. Twardzik, and B. Moss.

Deletion of the vaccinia virus growth factor gene reduces virus virulence. *J Virol*, 62(3):866–74, 1988.

[118] J. A. McCart, J. M. Ward, J. Lee, Y. Hu, H. R. Alexander, S. K. Libutti, B. Moss, and D. L. Bartlett. Systemic cancer therapy with a tumor-selective vaccinia virus mutant lacking thymidine kinase and vaccinia growth factor genes. *Cancer Res*, 61(24):8751–7, 2001.

[119] A. Dyer, Y. Di, H. Calderon, S. Illingworth, G. Kueberuwa, A. Tedcastle, P. Jakeman, S. L. Chia, A. Brown, M. A. Silva, D. Barlow, J. Beadle, T. Hermiston, D. J. Ferguson, B. Champion, K. D. Fisher, and L. W. Seymour. Oncolytic group b adenovirus enadenotucirev mediates non-apoptotic cell death with membrane disruption and release of inflammatory mediators. *Mol Ther Oncolytics*, 4:18–30, 2017.

[120] C. A. Fajardo, S. Guedan, L. A. Rojas, R. Moreno, M. Arias-Badia, J. de Sostoa, C. H. June, and R. Alemany. Oncolytic adenoviral delivery of an egfr-targeting t-cell engager improves antitumor efficacy. *Cancer Res*, 77(8):2052–2063, 2017.

[121] Kurt Langenbach. Atcc technology assessment of roche xcelligence system: an electronic impedance-based cell sensing unit. *BioTechniques*, 49(6):905–906, 2010.

[122] N. G. Chen, Y. A. Yu, Q. Zhang, and A. A. Szalay. Replication efficiency of oncolytic vaccinia virus in cell cultures prognosticates the virulence and antitumor efficacy in mice. *J Transl Med*, 9:164, 2011.

[123] J. Lokau, V. Schoeder, J. Haybaeck, and C. Garbers. Jak-stat signaling induced by interleukin-6 family cytokines in hepatocellular carcinoma. *Cancers (Basel)*, 11(11), 2019.

[124] C. Myskiw, J. Arsenio, E. P. Booy, C. Hammett, Y. Deschambault, S. B. Gibson, and J. Cao. Rna species generated in vaccinia virus infected cells activate cell type-specific mda5 or rig-i dependent interferon gene transcription and pkr dependent apoptosis. *Virology*, 413(2):183–93, 2011.

[125] J. Delaloye, T. Roger, Q. G. Steiner-Tardivel, D. Le Roy, M. Knaup Reymond, S. Akira, V. Petrilli, C. E. Gomez, B. Perdiguero, J. Tschopp, G. Pantaleo, M. Esteban, and T. Calandra. Innate immune sensing of modified vaccinia virus ankara (mva) is mediated by tlr2-tlr6, mda-5 and the nalp3 inflammasome. *PLoS Pathog*, 5(6):e1000480, 2009.

[126] C. Samuelsson, J. Hausmann, H. Lauterbach, M. Schmidt, S. Akira, H. Wagner, P. Chaplin, M. Suter, M. O'Keeffe, and H. Hochrein. Survival of lethal poxvirus infection in mice depends on tlr9, and therapeutic vaccination provides protection. *J Clin Invest*, 118(5):1776–84, 2008.

[127] Z. Waibler, M. Anzaghe, H. Ludwig, S. Akira, S. Weiss, G. Sutter, and U. Kalinke. Modified vaccinia virus ankara induces toll-like receptor-independent type i interferon responses. *J Virol*, 81(22):12102–10, 2007.

[128] J. Zhu, J. Martinez, X. Huang, and Y. Yang. Innate immunity against vaccinia virus is mediated by tlr2 and requires tlr-independent production of ifn-beta. *Blood*, 109(2):619–25, 2007.

[129] S. Ebrahimi, E. Ghorbani, M. Khazaei, A. Avan, M. Ryzhikov, K. Azadmanesh, and S. M. Hassanian. Interferon-mediated tumor resistance to oncolytic virotherapy. *J Cell Biochem*, 118(8):1994–1999, 2017.

[130] B. Ruf, S. Berchtold, S. Venturelli, M. Burkard, I. Smirnow, T. Prenzel, S. W. Henning, and U. M. Lauer. Combination of the oral histone deacetylase inhibitor resminostat with oncolytic measles vaccine virus as a new option for epi-virotherapeutic treatment of hepatocellular carcinoma. *Mol Ther Oncolytics*, 2:15019, 2015.

Erklärung zum Eigenanteil

Die Konzeption der Studie erfolgte durch Herrn Prof. Dr. U. M. Lauer in Zusammenarbeit mit Frau Dr. S. Berchtold.

Sämtliche Versuche wurden nach Einarbeitung von mir eigenständig durchgeführt. Die regelmäßige Pflege und Kontrolle der verwendeten Zellkulturen wurde paritätisch von Sebastian Gräter (Doktorand) und mir übernommen. Die Datenerhebung und statistische Auswertung erfolgten nach entsprechender Einweisung selbstständig durch mich.

Bei der eingereichten Dissertation handelt es sich um meine eigenständig erbrachte Leistung. Die Dissertationsschrift wurde nach Anleitung durch Herrn Prof. Dr. U. M. Lauer und Frau Dr. S. Berchtold selbstständig verfasst. Es wurden nur die angegebenen Quellen und Hilfsmittel benutzt und sich keiner unzulässigen Hilfe Dritter bedient. Wörtlich oder sinngemäß aus anderen Werken übernommene Inhalte habe ich als solche kenntlich gemacht.

Die Arbeit oder Teile davon habe ich bislang nicht an einer Hochschule des In- oder Auslands als Bestandteil einer Prüfungs- oder Qualifikationsleistung vorgelegt.

Die Richtigkeit der vorstehenden Erklärungen bestätige ich.

Danksagung

Mein herzlichster Dank geht an alle, die mit Ihrer tatkräftigen und moralischen Unterstützung zum Gelingen dieser Doktorarbeit beigetragen haben.

Allen voran möchte ich mich bei meinem Doktorvater, Herrn Prof. Dr. Ulrich M. Lauer, für die Überlassung des Themas, die freundliche Aufnahme in seine Arbeitsgruppe, die Bereitstellung aller benötigten Resourcen, sowie für seine persönliche Zeit und Engagement für diese Arbeit bedanken.

Ein besonderer Dank geht an Frau Dr. Susanne Berchtold, für die engagierte persönliche Betreuung und das regelmäßige gründliche Korrigieren meiner Texte. Ebenso möchte ich Frau Irina Smirnow ganz herzlich dafür danken, dass sie mich in die notwendigen Laborarbeiten eingearbeitet hat und mir während meiner Arbeit allzeit hilfreich zur Seite stand.

Bedanken möchte ich mich auch bei Herrn Dr. Markus Burkard, Herrn Christian Leischner, Frau Andrea Schenk und Herrn Dr. Dr. Sascha Venturelli für ihre Hilfsbereitschaft, anregende Gespräche und ein stets offenes Ohr für Fragen.

Des weiteren bedanke ich mich bei meinen Kommilitonen und Laborkollegen, Sebastian Gräter, Joschka Gottesleben, Maximilian Härtel und Stavros Sotiriadis für die gemeinsame Zeit im Labor und außerhalb, sowie für ihren Support.

Letztendlich geht mein größter Dank an meine Familie, meine Freunde und meine Partnerin, meinen unerschöpflichen Quellen an Freude und Inspiration. Vielen Dank, dass ihr diesen Weg gemeinsam mit mir gegangen seit und mir stehts zur Seite steht. Ganz besonders danke ich meinen Eltern, für ihre unbedingte und grenzenlose Unterstützung.